Fluorophore Studies & Instrumentation Development for Tumour Margin Estimation

Hazel L. Stewart

A thesis submitted to the University of Strathclyde for the degree of

Doctor of Philosophy with Integrated Study

Optical Medical Imaging with Healthcare Innovation & Entrepreneurship

Photophysics Research Group
Department of Physics
University of Strathclyde
Glasgow

2019

This thesis is the result of the author's original research. It has been composed by the author and has not been previously submitted for examination which has led to the award of a degree.

The copyright of this thesis belongs to the author under the terms of the United Kingdom Copyright Acts as qualified by University of Strathclyde Regulation 3.50. Due acknowledgement must always be made of the use of any material contained in, or derived from, this thesis.

Signed:

Date:

Abstract

Surgery remains a key treatment option for tumour removal, where surgeons primarily rely on eye and touch to assess the boundary between healthy and cancerous tissue with no cellular information as guidance. There is therefore a need for a device or instrument that can be used by the surgeon in real-time during the surgical procedure that will ensure as many of the cancerous cells have been removed as possible. Fluorescence-based techniques have great potential for such an application, wherein this thesis explores various aspects related to the use of fluorescence techniques for estimating tumour margins.

The intrinsic fluorophore NAD(P)H has been studied due to the significant interest it has gained for its use in tumour margin estimation, where the influence of environmental factors on the properties of NAD(P)H in various solvents were initially investigated. An increase in the fluorescence lifetime of NADH was observed in water and ethylene glycol upon oxygen removal, where the average lifetimes increased from 0.40 ns to 0.45 ns and 0.76 ns to 0.94 ns respectively. In addition to this, fluorescence anisotropy measurements revealed two rotational correlation times of 0.43 ± 0.24 ns and 5.49 ± 0.04 ns for NADH in ethylene glycol. These times correspond to particle sizes of ~ 0.6 nm and 1.4 nm which have been attributed to the folded and unfolded conformations of NADH free in solution respectively, where such methods have not previously been reported for resolving the folded and unfolded conformations of NADH.

NAD(P)H was also studied in the cellular environment, where a decrease in every lifetime component of NAD(P)H in cancerous prostate cells incubated in high glucose media compared to those in low glucose media has been observed, where decreases of 0.52 ns, 2.1 ns and 0.10 ns were found for τ_1, τ_2, (bound NAD(P)H) and τ_3 (unbound NAD(P)H) respectively. In contrast to this, no change in lifetime was observed in healthy prostate cells incubated in both high and low glucose media. It is believed that the observed decrease in lifetime components in the cancer cells is due to the preferential use of the glycolysis pathway in these cells, which has been previously linked to a decrease in fluorescence lifetime of certain cancerous cell lines.

Additionally, a low-cost liquid light guide-based fluorescence lifetime system incorporating a translational stage has been designed for phantom margin assessments, where the margins were created using silica sol-gels. Measurements of phantom margins with Rhodamine 6G and NADH in the doped sol-gel region demonstrated that the sol-gel only region could be clearly identified 1 mm after the margin position based on the fluorescence decays obtained. Measurements were also performed using FDA-approved Indocyanine Green in the doped sol-gel region of the phantom margin, however only scatter from the sol-gel could be detected 7 mm before the margin. A comparison between light guide and single-photon avalanche diode (SPAD) array fluorescence lifetime imaging microscopy (FLIM) measurements demonstrated improved spatial resolution provided by the FLIM system for assessing the margin position with short-lived fluorophores such as ICG, where the sol-gel only region of the ICG-doped sample could be clearly identified 1 mm after the margin using this system.

Acknowledgements

Many thanks to my supervisor Professor David Birch for providing me with this opportunity to undertake a PhD and for accepting me as a summer research student all those years ago. His guidance and advice whether it be about science or life has always been valued and will stay with me for many years. I would also like to thank my second supervisor Ted Hupp for his additional guidance and support, and John Revie for his help with my many requests for instrument parts.

I would like to thank the members of the Photophysics Group who have graced the office over the years and have never failed to make me laugh day in and day out. A special mention goes to Chloe who has been there for me since our summer research days to take 2-hour breaks from labs to sort out life problems, and also to Gillian who started the Optima journey with me and was always ready to provide a glass of wine when required and keep me right with course deadlines.

I would also like to thank those who put the Optima PhD programme together as I wouldn't have had this opportunity without them in the first place, and I wish the best of luck to the rest of the 2015 cohort as well in all their future endeavours. A special thanks also goes to the Glasgow Girls – I couldn't have asked for a better group to have worked through the impossible business courses with. You made the train journeys to Edinburgh much more bearable and made me feel great about my board game abilities.

I would like to finally thank my friends and family for always checking in on me and tentatively asking how the project was going. I would like to thank my parents especially – you have always believed in me and without your continuing support I would not have been able to finish the PhD. And a special thanks to my mum for providing copious amounts of homemade soup and tins of tuna – possibly the most important contributions to the completion of the PhD.

Publications & Proceedings

H. L. Stewart, P. Yip, M. Rosenberg, T. J. Sorensen, B. W. Laursen, A. E. Knight & D. J. S. Birch, "Nanoparticle metrology of silica colloids and super resolution studies using the ADOTA fluorophore", *Meas. Sci. Technol.*, 2016, 27, 045007 (https://doi.org/10.1088/0957-0233/27/4/045007).

H. L. Stewart, T. R. Hupp & D. J. S. Birch, "Glucose Imaging for Improved Cancer Surgery", Poster Presentation, TransMed 2017, Edinburgh.

H. L. Stewart, T. R. Hupp & D. J. S. Birch, "NADPH: A Potential Probe for Improved Cancer Surgery", Student & Poster Presentation, FluoroFest 2017, Glasgow.

H. L. Stewart, T. R. Hupp & D. J. S. Birch, "NADPH: A Potential Probe for Improved Cancer Surgery", Poster Presentation, SUPA Annual Gathering 2017, Edinburgh.

H. L. Stewart, T. R. Hupp & D. J. S. Birch, "A liquid light guide-based fluorescence lifetime system towards improved precision in cancer surgery", Poster Presentation, MAF 2017, Bruges.

H. L. Stewart, T. R. Hupp & D. J. S. Birch, "A liquid light guide-based fluorescence lifetime system and potential biomarker for improved precision in cancer surgery", Oral Presentation, Biomedical Imaging Summer School 2017, London.

H. L. Stewart, T. R. Hupp & D. J. S. Birch, "NADPH as a potential intrinsic probe for tumour margin estimation", *Proc. SPIE 10478,* Molecular-Guided Surgery: Molecules, Devices & Applications IV, 2018, 1047817 (https://doi.org/10.1117/12/2287414). Student & Poster Presentation, SPIE Photonics West BiOS, San Francisco.

H. L. Stewart, T. R. Hupp & D. J. S. Birch, "Intrinsic & extrinsic probe studies for tumour margin estimation", Oral Presentation, FluoroFest 2019, Fort Worth.

Abbreviations

5-ALA – 5-aminolevulinic acid

ADC – Analogue-to-digital convertor

ADOTA – Azadioxatriangulenium

ATP – Adenosine triphosphate

CMOS – Complementary metal-oxide semiconductor

DMEM – Dulbecco's Modified Eagle Medium

DMSO – Dimethyl sulfoxide

FAD – Flavin adenine dinucleotide

FLIM – Fluorescence lifetime imaging microscopy

FRET – Förster Resonance Energy Transfer

G6P – Glucose-6-phosphate

ICG – Indocyanine Green

IRF – Instrument response function

MCA – Multi-channel analyser

NAD^+ – Nicotinamide adenine dinucleotide (oxidised form)

NADH – Nicotinamide adenine dinucleotide (reduced form)

$NADP^+$ - Nicotinamide adenine dinucleotide phosphate (oxidised form)

NADPH – Nicotinamide adenine dinucleotide phosphate (reduced form)

NIR – Near-infrared

NLLS – Nonlinear least squares

PBS – Phosphate buffered saline

PDT – Photodynamic therapy

PMT – Photomultiplier detector

PPP – Pentose phosphate pathway

R5P – Ribose-5-phosphate

R6G – Rhodamine 6G

RPMI – Roswell Park Memorial Institute

SLN – Sentinel lymph node

SPAD – Single photon avalanche diode

TAC – Time to amplitude convertor

TCSPC – Time correlated single photon counting

TEOS – Tetraethyl orthosilicate

TMOS – Tetramethyl orthosilicate

TRES – Time-resolved emission spectra

Table of Contents

1. Introduction

1.1 Cancer Treatment

Cancer is one of the leading causes of death worldwide, where over 18 million cases were diagnosed globally in 2018[1]. This is set to rise to over 29 million diagnoses by 2040[1], and so the continuous development and improvement of cancer treatment remains of high importance. There are several treatment options available to cancer patients which are typically chosen depending on the type and stage of cancer. Some of the most common treatment options include chemotherapy, radiotherapy and surgical removal, where more specific techniques include photodynamic therapy (PDT) for the treatment of cancers in the neck and head areas, laser treatment for very early stage cancers that are close to the body surface, as well as high intensity focused ultrasound which can be used for treating single tumours or parts of large tumours[2]. Cancer treatments are under continuous development, where examples of newer treatment methods that are being more commonly used include immunotherapy where certain drugs can be used to re-establish the ability of the immune system in eliminating cancer cells while not causing additional damage to healthy cells[3], as well as gene therapy which can be used to modify, delete or replace abnormal genes specific to the target cancer cells[4].

While various cancer treatments are currently being developed, surgery remains one of the most common treatment options for tumour removal, where in the UK ~ 49% of all patients cured undergo surgical intervention[5]. This project focuses on the surgical aspect of cancer treatment, where the steady rise in cancer cases each year and the common use of surgery in tumour removal means it is essential to continue the improvement of cancer surgery through research.

1.1.1 Available Surgical Techniques

Many surgical techniques are currently employed over the various stages of cancer diagnosis and treatment. For example, different endoscopic procedures can be used for the detection of various types of cancer, such as bronchoscopy for the diagnosis

of lung cancer[6], colonoscopy for detecting colorectal cancer[7], cystoscopy for cancer of the bladder[8] and laparoscopy for diagnosing liver, pancreatic and ovarian cancer[9]. For treating cancers, surgery can typically involve large incisions through skin, muscle and sometimes bone to reach and remove the cancer, however there are some less invasive techniques also available to minimise recovery time and damage to healthy tissue. Examples include laparoscopy again, which can be used in the treatment of certain cancers such as those in the abdomen or prostate[10], laser surgery where a beam of high intensity light is used to remove the cancerous tissue without damaging surrounding tissue[11], cryosurgery which utilises liquid nitrogen to freeze and kill abnormal cells[12] and also Mohs micrographic surgery, which can be used to shave off certain skin cancers[13].

During cancer surgery it is important that as much of the cancerous tissue is removed as possible while also preventing unnecessary damage to surrounding healthy tissue[14]. To accomplish this, surgeons primarily rely on visual inspection, palpation and experience in order to determine cancerous tissue during surgery. The margin between the cancerous cells and the cut tissue edge is known as the surgical margin. A negative surgical margin indicates there are no cancerous cells near the edge of the cut tissue and a positive margin indicates that there are cancerous cells present at or very close to the cut tissue edge, where it is therefore possible that cancerous tissue remains in the body[15]. While visual inspection and palpation can be effective for bulk tumour, it lacks sensitivity in detecting cancer at the cellular level[16] potentially leading to a positive margin and the patient requiring further surgery.

The current gold standard for margin assessment is slide-based histology, which can be a time-consuming and laborious process that is completed post-operatively[17]. There are other techniques currently available for estimating tumour margins intraoperatively, some of which include frozen section histology, intraoperative MRI, CT[18], ultrasound[19] and optical coherence tomography[20]. However, these have their own drawbacks and are not in widespread use, where some drawbacks include requiring highly complex and specialised surgical suites for the use of intraoperative MRI and CT in particular which are also currently limited in their use to neurosurgery[18], as well as other techniques being limited in spatial resolution and

contrast compared to post-operative histology[17]. New technology for intraoperative margin assessment needs to be able to match the diagnostic accuracy of post-operative histology but offer further benefits such as reduced turnover times, practicality and reduced cost before they can be considered for routine clinical practice[21]. Various methods for improving the intraoperative assessment of tumour margins are currently being developed, where some recent examples include the development of MarginProbe® that can measure the electrical properties of breast tissue using radiofrequency waves[21,22], as well as ClearEdge™ that utilises bioimpedance spectroscopy to measure the variation in the dielectric properties of different tissues[23,24]. However, one area that has gained significant interest for intraoperative margin assessment is the use of fluorescence-based techniques, which is the focus of this work.

1.1.2 Fluorescence-based Surgical Applications

Fluorescence has been used in surgery since 1948 where it was used for the identification of brain tumours during neurosurgery using fluorescein[25]. It has since found various clinical applications which include in tissue perfusion and the detection of vital structures such as the bile duct[14]. Its potential is still being explored in other areas, for instance in visualising biological structures such as the parathyroid and the ureter to avoid injury during surgery[26,27].

Fluorescence-based techniques have many advantages for their use in surgical procedures and tumour margin estimation in particular, which include high contrast and sensitivity, intuitive operation, relatively low cost, ease of image acquisition as well as high selectivity for certain cancer cells[18,28]. The use of fluorescence in cancer surgery has been widely reviewed in recent years and is one of the most commonly researched applications of fluorescence-based surgical techniques, where reviews have included topics such as a summary of requirements and limitations in molecular image-guided surgery[29], a look at the current status and potential future trends in fluorescence-guided surgery in general[30,31] as well as more focused reviews on probes[32] and instrumentation[33] in particular. Two of the main oncological

applications include sentinel lymph node (SLN) mapping and tumour imaging. The SLN is the first drainage site of cancer cells from the primary tumour, where a fluorescent dye can be used to visualise the location of the SLN using only a low dose of the contrast agent[18]. These contrast agents are able to bind to cells in the lymph nodes, where a combination of radioactive tracers and fluorophores can also be used to improve SLN mapping[34].

The other main oncological application for fluorescence is to use fluorescent agents in tumour imaging for visualising cancerous tissue, where they have the ability to detect small tumour lesions that could be easily missed during surgery. Such practises are the focus of interest in this work, where recent techniques with significant relevance to this work include the use of fluorescence lifetime imaging microscopy (FLIM) for visualising autofluorescence from components such as the reduced form of the coenzyme nicotinamide adenine dinucleotide and its phosphorylated derivate (NAD(P)H) and flavin adenine dinucleotide (FAD) in tissues and cell studies[35,36], where recent studies have been conducted without inducing significant chemical changes to samples of fixed tissue[37]. The development of new extrinsic probes is also of interest, where one example is the use of an antibody conjugated to a near infrared (NIR) dye for determining squamous cell carcinomas of the head and neck[38]. Developments in complementary instrumentation are also taking place, where examples include the development of technology such as single photon avalanche diode arrays for real-time FLIM to identify tumour margins[39], as well as the development of complete instruments such as the PerkinElmer IVIS® Spectrum[40,41], the Quest Spectrum® fluorescence imaging system[42], and the FLUOBEAM® camera[43,44]. While many instruments and methods are currently being researched and developed, most are still in pre-clinical stages of development and those that are approved are not without their limitations. Such limitations include being restricted in their use with a specific fluorophore, the ability to operate in an ambient light setting not yet being fully realised[33], and systems only being able image macroscopically and not obtain contrast at the cellular level[29], where the consequence of these limitations is that surgeons still largely rely on vision and touch despite the availability of these technologies[33]. Continued research into these techniques is required to try and eliminate these drawbacks and further advance

the field of margin estimation, finding a cost-effective and practical solution for surgeons to use in accurately identifying margins intraoperatively. The work in this thesis looks to contribute to the utilisation of fluorescence-based techniques in margin assessment where both fluorescence lifetime spectroscopy and FLIM have been considered.

1.2 Intrinsic Fluorophores

Intrinsic fluorophores refer to fluorophores that occur naturally. Examples of such fluorophores can include aromatic amino acids, flavins and porphyrins found in the body, as well as the green pigment chlorophyll found in plants. One of the major advantages of using intrinsic fluorophores for biological applications is that the cells or structures do not have to be altered in any way to be studied – no external fluorophore is required to monitor them. This is useful as not only does it mean there are no external factors that will influence the biological processes, but there are also significantly less regulatory requirements that have to be met for their use in clinical applications in comparison to extrinsic probes[18]. Complications with intrinsic probes can arise however from the potentially shallow penetration depth into tissue due to excitation in UV/visible spectrum, as well as the number of other intrinsic fluorophores that may fluoresce under similar conditions to the probe of interest. There are in fact several biological structures in the body that can fluoresce, where some of the most common are listed in Table 1.1 along with their fluorescence properties[45,46].

Fluorophore	Abs. Max. (nm)	Em. Max. (nm)	Quantum Yield	Avg. Lifetime (ns)
NAD(P)H	340	450	-	0.4
Collagen	325	400, 405	-	5.3
Tryptophan	280	350	0.13	3.1
Tyrosine	275	300	0.14	3.6
Phenylalanine	260	280	0.02	6.8
Flavins	450	535	-	2.3 – 4.7
Elastin	290, 325	340, 400	-	2.3

Table 1.1: List of intrinsic fluorophores present in the body and their corresponding absorption maximum, emission maximum, quantum yield and average lifetime. References for the quantum yield could only be obtained for three of the intrinsic fluorophores listed.

Table 1.1 highlights the potential complexity of using an intrinsic fluorophore as a probe due to the overlap of the excitation and emission properties. This work focuses on the use of NAD(P)H – a set of coenzymes used by the body which will be discussed in more detail in Section 1.2.1. Table 1.1 shows that there is overlap in the absorption maxima of NAD(P)H with that of collagen and elastin in particular; however the combination of factors such as the greater variation in emission maxima between the three species as well as the differences in the fluorescence lifetimes should help in distinguishing the signal of NAD(P)H through the use of time-resolved fluorescence techniques.

The term NAD(P)H collectively refers to two different coenzymes: the reduced form of nicotinamide adenine dinucleotide (NADH) and its phosphorylated derivative (NADPH). These coenzymes have very similar structures but play very different roles in the body. The role of each will be discussed here where its structure and fluorescence properties are discussed in more detail in Chapter 4.

1.2.1 NADH

Glucose is a simple sugar that can be broken down to provide cells with energy through a process called cellular respiration, where it is broken down into carbon dioxide and water. Energy is produced through this process in the form of adenosine triphosphate (ATP) molecules, where these molecules store the energy required by the body and are known as the currency of energy in biological systems. The process of cellular respiration occurs over four main pathways: glycolysis, pyruvate oxidation, the citric acid cycle and oxidative phosphorylation. NADH is produced during the first three stages of cellular respiration and is crucial in the production of ATP. The coenzyme exists in two states: its oxidised form (NAD^+) and the reduced form (NADH), where it readily cycles between these two states. NAD^+ is the primary electron carrier in cellular respiration, where it accepts two electrons and one H^+ to become the higher energy form NADH. Electrons are removed from the glucose molecules in a controlled way to ensure the consequent controlled release of energy. The reduction of NAD^+ to NADH is shown in Figure 1.1. NADH carries the electrons to the electron transport chain in the inner mitochondrial membrane of the cell where oxidative phosphorylation occurs. The electrons are deposited at the beginning of the chain, where they then move through the chain and energy is released at different steps. The energy is then captured and used to produce ATP[47]. The majority of ATP molecules from one molecule of glucose are produced through this oxidative phosphorylation pathway.

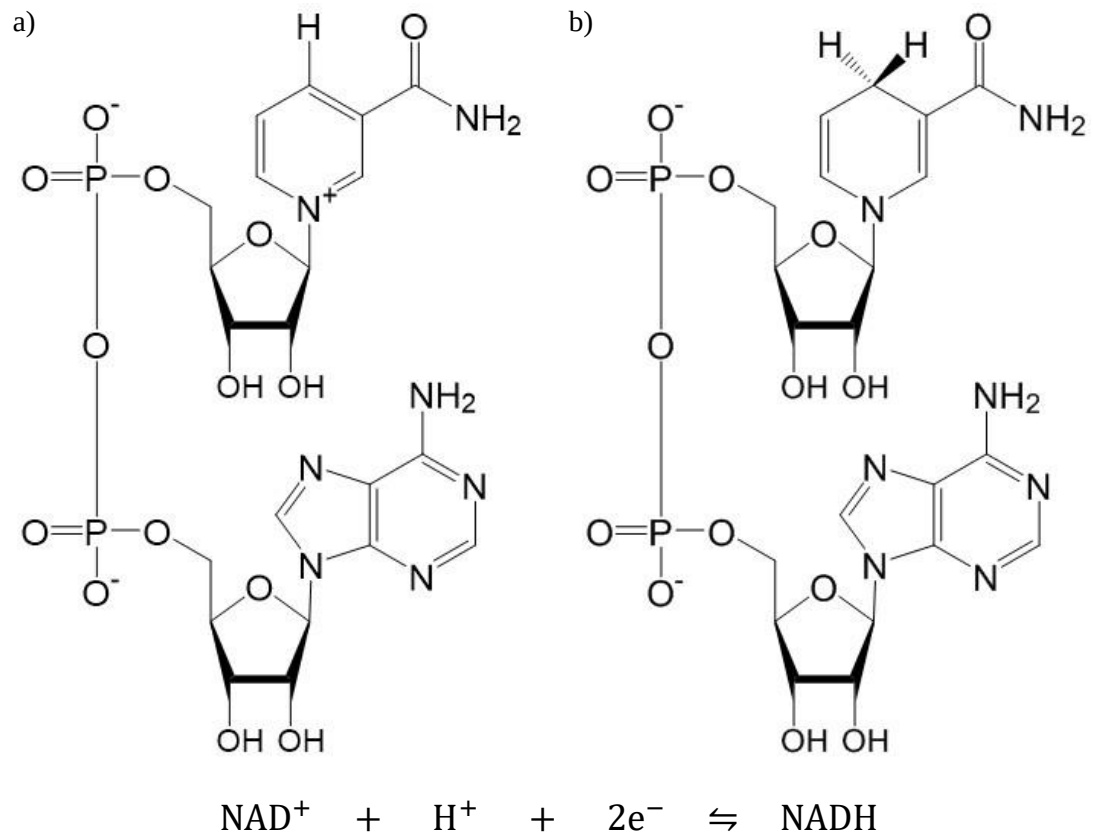

Figure 1.1: a) Oxidised and b) reduced forms of the coenzyme NAD denoted by NAD^+ and NADH respectively, and the corresponding REDOX reaction equation between each form.

1.2.2 NADPH

During the glycolysis process of cellular respiration, a phosphate group is added to the glucose molecule to produce glucose-6-phosphate (G6P). While this molecule can go on to be used in cellular respiration, there is an alternative branch to a process called the Pentose Phosphate Pathway (PPP) that G6P can instead be used in for the production of two molecules in particular: the coenzyme NADPH and ribose-5-phosphate (R5P).

The PPP is split into two phases: the oxidative and non-oxidative phases. The non-oxidative phase is primarily used to produce R5P that can go on to be used for the synthesis of nucleotides and nucleic acids, which are some of the essential building blocks of DNA and RNA. The oxidative phase of the PPP is instead used to produce NADPH, which acts as an electron shuttle like NADH but interacts with a different

set of enzymes. NADPH has almost an almost identical structure to NADH with the exception of an additional phosphate group located on the ribose ring that is attached to the adenine moiety. It is essential in macromolecular biosynthetic processes as well as maintaining safe levels of reactive oxygen species in the body, where the reduced form is the dominant form of this coenzyme and is readily available to donate electrons to these processes. In comparison to this, the oxidised form of NAD – NAD^+ – is dominant, where the difference in these ratios of the two coenzymes and the additional phosphate group of NADPH allow them to interact with different sets of enzymes.

1.3 Cancer Cell Metabolism

There are many differences in the metabolic processes involved in both cellular respiration and the PPP in cancerous cells compared to healthy cells. While healthy cells primarily rely on the oxidative phosphorylation pathway for the generation of ATP, where pyruvate is produced through glycolysis under normal oxygen levels with most of it entering the mitochondria to take part in the citric acid cycle, this is not the case for cancer cells. Metabolic changes are made within the cells in response to genetic mutations and the tumour microenvironment in order to meet their three basic needs: a rapid generation of ATP to maintain energy status, an increased biosynthesis of macromolecules such as carbohydrates and proteins, and maintenance of the cell's REDOX status[48]. A simplified change in the cell respiration process in cancer cells is shown in Figure 1.2.

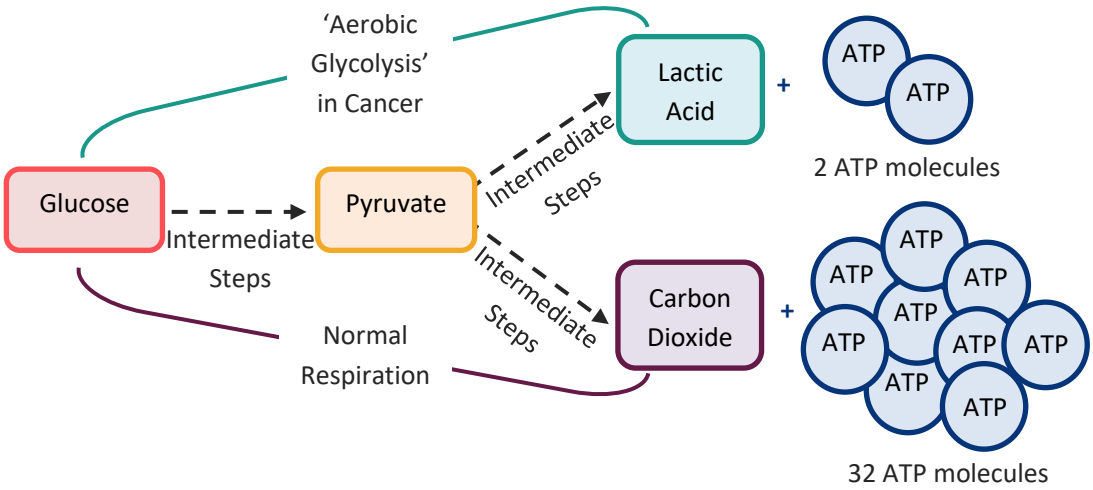

Figure 1.2: Simplified depiction of the difference in the cell respiration processes in healthy cells (bottom pathway) and cancerous cells (top pathway). Healthy cells rely on oxidative phosphorylation to produce ATP which releases carbon dioxide as a waste product whereas cancer cells rely on the glycolysis pathway which instead secretes lactic acid.

Oxygen is required in healthy cells to undergo the process of aerobic respiration, where the pyruvate produced from glycolysis is broken down to produce carbon dioxide and water alongside the majority of ATP needed by the cells. When there is insufficient oxygen the cells will switch to anaerobic respiration, where the pyruvate is not broken down completely and instead produces lactic acid, where this pathway is much less efficient in producing ATP. It has been found that cancer cells also produce a significant amount of lactic acid regardless of how much oxygen is available to the cells. This phenomenon is known as the 'Warburg effect' and was first proposed by Otto Henreich Warburg in 1924, who believed the oxidative phosphorylation pathway was disrupted in cancer cells leading to a switch to glycolysis for generating sufficient ATP[49,50]. It was later revealed however that this was not necessarily the case, as the oxidative phosphorylation pathway still functioned as normal in many cancer cell types[51]. Clinical data from the past decade has shown that an increased glucose uptake was observed in > 90% of human cancer types measured, indicating the preferential use of the so-called 'aerobic glycolysis' pathway[52]. The generation of sufficient ATP remains one potential reason for the increased rate of glycolysis in cancer cells, however it is still a subject of debate and a full explanation for this switch remains unclear[52,53]. One such proposition for the upregulation of the glycolysis pathway required by cancer cells is to increase the

production of NADPH in particular via the PPP. As previously mentioned NADPH is crucial in the biosynthesis of macromolecules, therefore to meet the higher demands for biosynthesis in cancer cells there is in turn a higher demand for NADPH. In addition to this, it also crucial for regulating the elevated levels of reactive oxygen species that are produced during the rapid cell proliferation of cancer cells[48,54]. While the reason for the switch to glycolysis in these cells remains unclear, the upregulation of this pathway has been previously linked to a decrease in the fluorescence lifetime of NAD(P)H in certain cancerous and pre-cancerous cell lines[55,56] – a mechanism which is investigated in Chapter 6 of this thesis.

1.4 Extrinsic Fluorophores

Extrinsic fluorophores are also utilised in various aspects of this work. Extrinsic fluorophores have their own advantages over intrinsic fluorophores for medical applications such as there being more control in choosing the location at which the fluorescent label is attached, as well as being typically designed to have enhanced fluorescence properties that make them more ideal for such applications[57]. This section characterises two of the main extrinsic fluorophores used in this work, which include the methyl derivative of azadioxatriangulenium (MeADOTA) for its use in characterising silica nanoparticle sizes, and Indocyanine Green (ICG) for its use in phantom tumour margin measurements.

1.4.1 MeADOTA

ADOTA is a cationic triangulenium dye, where the unique combination of properties such as a long fluorescence lifetime of ~ 20 ns and fluorescence emission towards the red part of the spectrum make this an ideal fluorophore for monitoring the rotation of larger molecules through fluorescence polarisation and fluorescence anisotropy[58]. The chemical structure and absorption and emission spectra of the methyl derivative MeADOTA used in this work are shown in Figure 1.3.

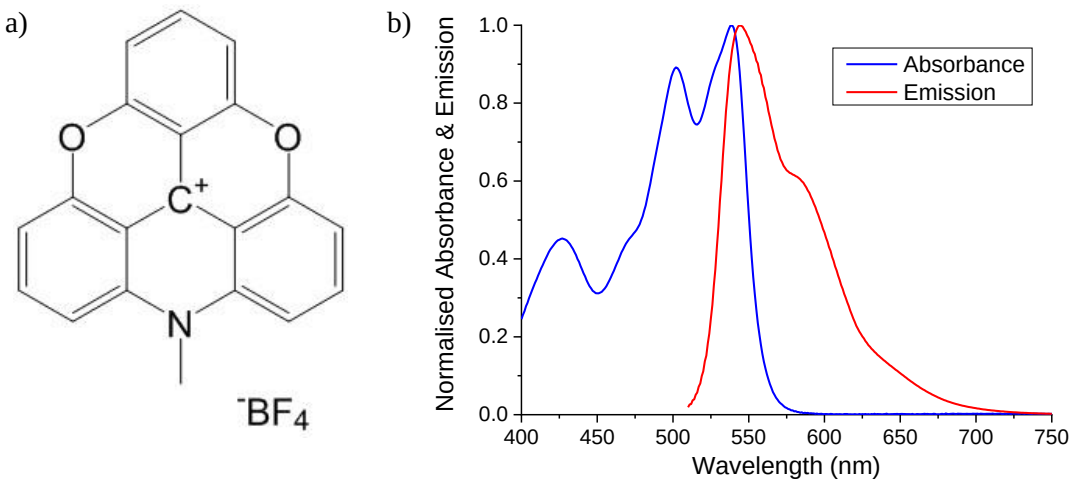

Figure 1.3: a) Chemical structure and b) the normalised absorption and emission spectra of MeADOTA. The emission spectrum was measured using a 570 nm excitation wavelength.

ADOTA and various derivates of this fluorophore have been studied and characterised in different environments[58,59], have been shown to enhance the fluorescence emission from metals[60], and the MeADOTA derivative has been used as part of this work for measuring silica nanoparticles using fluorescence anisotropy[61]. The properties of ADOTA such as its long lifetime also give it potential in biomedical applications, where it can be used for binding to large biomolecules such as proteins[62], and it has also been shown using time gating and fluorescence lifetime correlation spectroscopy that ADOTA labelled with Hyaluronan can be used to detect hyaluronidase, which can be over-expressed in many types of cancer[63].

1.4.2 Indocyanine Green

ICG is one of the few and most commonly used FDA approved fluorescent probes for clinical applications, where other approved probes include Methylene Blue, 5-aminolevulinic acid (5-ALA) and Fluorescein[32]. ICG was originally developed for near-infrared (NIR) photography by Kodak in 1955 and was approved for clinical use a few years later for cardiac output monitoring[64,65]. Since then, ICG has been used in a wide range of medical applications that have included the imaging of retinal blood vessels[65], assessing liver function[66] as well as assessing the severity of burn wounds[67]. In addition to this, there have been many studies on the use of ICG in

cancer-based applications, which have included clinical studies on using ICG for SLN mapping for various cancers[14], as a fluorescence contrast agent[68] where it has been shown to accumulate in certain cancers such as those in the liver[69], which has also lead to developing potential treatments of cancers such as hepatocellular carcinoma using ICG in NIR PDT[70], and it has also been studied for its use in post-chemotherapy detection of residual breast tumour tissue[71]. The chemical structure of ICG is shown in Figure 1.4.

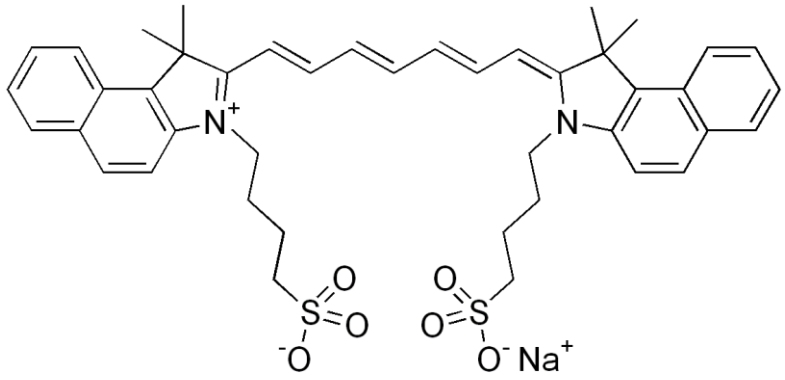

Figure 1.4: Chemical structure of Indocyanine Green (ICG)

ICG is a water-soluble tricarbocyanine molecule with a molecular weight of 774.96 g/mol[72]. ICG can be prone to aggregation like many carbocyanine dyes depending on its concentration and the solvent properties, where it is particularly prone to polymerisation at higher concentrations in aqueous solution[73]. The stability of ICG also depends on its storage temperature and light exposure, where prolonged exposure to light and higher temperatures can decrease its fluorescence intensity[74].

As well as already being FDA approved for clinical applications, the other main advantage of using ICG in fluorescence-based medical applications is that its absorption and emission are in the NIR region, with λ_{ex} *(max.)* ~ 780 nm and λ_{em} *(max.)* ~ 820 nm. NIR light is advantageous for such applications due to its capability of penetrating deeper into tissue compared to UV/visible light, as well as almost no autofluorescence being present at such wavelengths leading to enhanced contrast of different tissues[14]. Such advantages as well as the continuing interest in ICG for determining tumour tissue has led to its use in studies for this thesis.

1.5 Thesis Summary

The overall aim of this project was to utilise time-resolved fluorescence techniques in exploring several areas relevant to cancer surgery such as in instrumentation development, fluorescent probe studies and tissue phantom design. This work also demonstrates the advantages of such techniques for use in cancer surgery applications, where Chapter 2 discusses the main theory and experimental details behind the techniques used in this work.

Chapter 3 discusses the instrumentation design that was undertaken in this work. Liquid light guides were successfully incorporated into an existing fluorescence lifetime-based system, which was further developed into a system that utilised a translational stage in order to measure a sample at different positions.

Chapter 4 characterises the main intrinsic probe of interest NAD(P)H to gain a more detailed understanding of its sensitivity to its environment. Factors such as pH and oxygen levels that differ between healthy and cancerous cells were investigated in particular, where pH had a minimal effect on the fluorescence lifetime, but decreased oxygen levels caused an increase in the lifetime of NADH.

Chapter 5 details the study of various silica nanoparticles, where the fluorescent dye MeADOTA was successfully used to characterise a range of silica nanoparticle sizes. Silica sol-gels were then used as tissue phantoms to create phantom tumour margins. These were studied using the translational stage-based fluorescence lifetime system as well as with FLIM, demonstrating their capabilities of determining the phantom margin position to within 1 millimetre.

Chapter 6 continues the study of NAD(P)H where it is instead investigated in the cellular environment. Fluorescence lifetime comparisons are drawn between NAD(P)H in the healthy and cancerous prostate cell environments, where a higher ratio of unbound/bound NAD(P)H in the cancerous cells indicated a shift to the glycolysis pathway. A decrease in fluorescence lifetime was also observed with a higher glucose concentration in the cancerous cells where no change in lifetime was observed in the healthy cells for high and low glucose concentrations, highlighting another potential method of discriminating between the two cell types.

2. Theory

2.1 Fluorescence Photophysics

One of the first reports of the phenomenon of fluorescence came from Sir John William Herschel in 1845, who observed the emission of blue light from a quinine solution[75]. However it was not until 1852 the term ‘fluorescence’ was coined by Sir George Gabriel Stokes who studied the dispersion of light from a wide range of substances[76,77]. Fluorescence has since been developed for use in various research and practical applications such as medicine, chemical sensing, lighting and microscopy among numerous others, where its growing use in biological studies in particular has led to its utilisation in the work presented in this thesis.

2.1.1 Photoluminescence

The emission of light from a source can be divided into two categories: incandescence and luminescence. Incandescence describes the emission of light from heat energy, where luminescence describes the emission of light that is not attributed to the heating of the energy source. There are many forms of luminescence, one of which is photoluminescence where light is emitted from a source due to photoexcitation: electron excitation by the absorption of photons. Photoluminescence can be further broken down into the categories of fluorescence and phosphorescence, where the process of fluorescence is the focus of this work. Details of the different processes and timescales associated with photoluminescence can be described using a Jablonski diagram as shown in Figure 2.1.

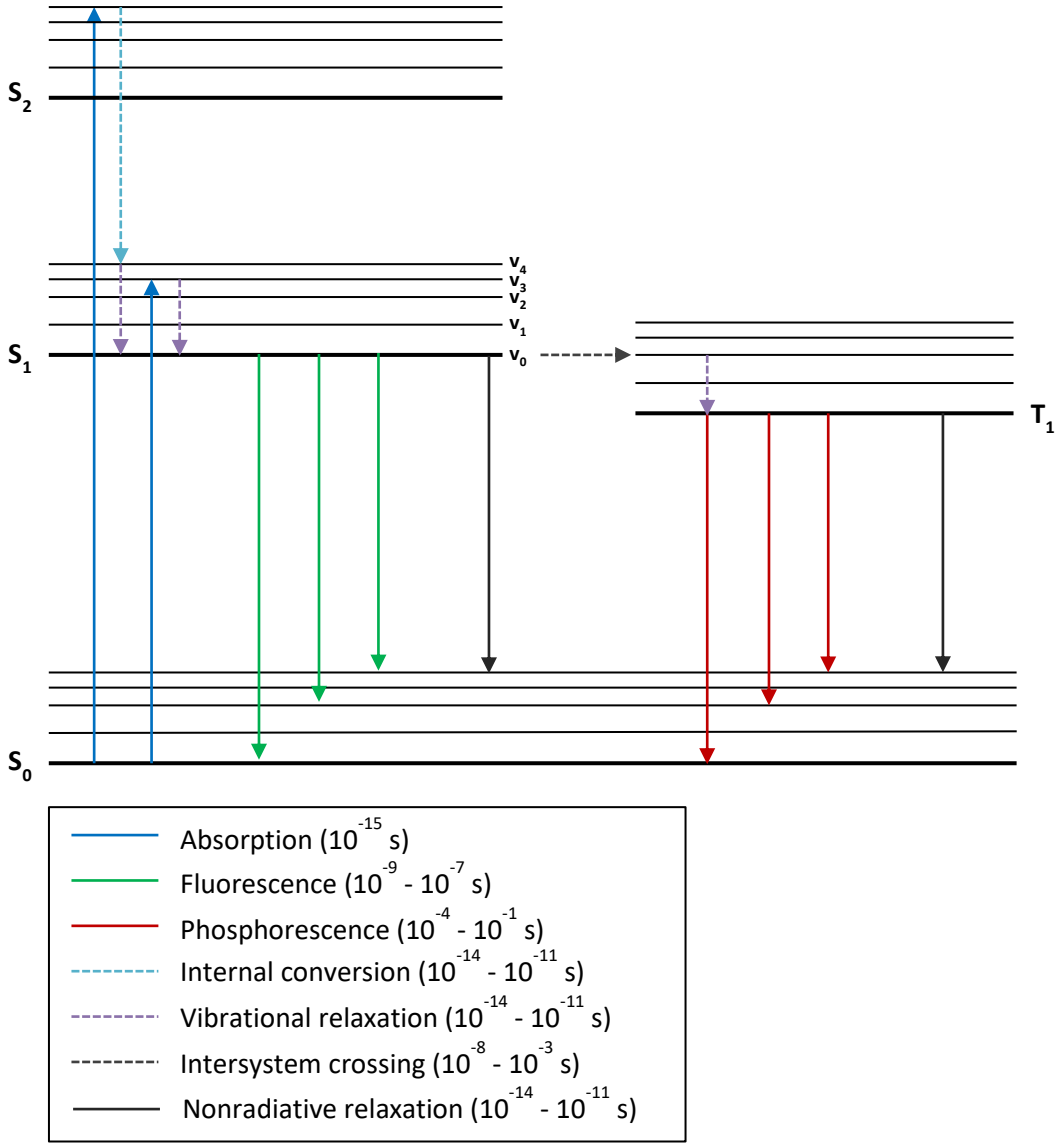

Figure 2.1: Jablonski diagram of the various processes associated with photoluminescence, along with the timescales associated with each process in the key.

When a fluorophore absorbs a photon of appropriate energy electronic excitation occurs, where an electron is excited from the ground state (S_0) to a singlet excited state (S_1, S_2, ...). Absorption is the fastest process to occur, where the energy level and vibrational level (v_1, v_2, ...) that the electron transitions to depends on the amount of energy that was transferred to it by the photon and the probability of the transition which is governed by selection rules. These include the Laporte selection rule, where an electronic transition must involve a change in the orbital angular momentum quantum number ℓ where $\Delta\ell = \pm 1$, as well as the spin selection rule where there is

no change in spin multiplicity and therefore $\Delta S = 0$[78] (where here S = total spin quantum number). Energy is quickly dissipated due to the instability of the molecule at this higher energy configuration, which can be through vibrational relaxation and/or internal conversion to different electronic states. Vibrational relaxation involves the loss of energy to other vibrational modes until the electron reaches the lowest vibrational level of the electronic state it is in, whereas through internal conversion the molecule loses energy by transitioning from an electronic state to a lower lying electronic state. Vibrational relaxation will occur immediately after internal conversion to the lowest vibrational level of the new electronic state.

Once in the lowest vibrational level the energy can either be emitted radiatively, lost through nonradiative processes such as quenching, or undergo intersystem crossing. Intersystem crossing is a non-radiative transition from the excited singlet state to the excited triplet T state, where instead of having an opposite spin state to the ground state electron, the excited electron instead has a parallel spin state. This transition is more likely to occur when there is an overlap in the vibrational levels of the two excited states as there are little or no energy changes allowed in the transition[79]. Intersystem crossing occurs again as the electron relaxes from the T_1 state to the S_0 state, where the emission of a photon from this transition is known as phosphorescence. This occurs on a much longer timescale in comparison to fluorescence due to the low probability of the T_1 to S_0 transition taking place.

Fluorescence is the emission of photons from the S_1 to S_0 transition and is the phenomenon of interest in this thesis. Since energy is lost through vibrational relaxation and internal conversion, the energy of the photon emitted is lower than the energy of the absorbed photon. The wavelength of the emitted photon is therefore longer, where this change in wavelength is known as the Stokes shift[76]. An example of this is shown in Figure 2.2, which also shows the mirroring of the absorbance and emission profiles. This occurs due to the similar spacing of the vibrational energy levels of the excited states to those of the ground state.

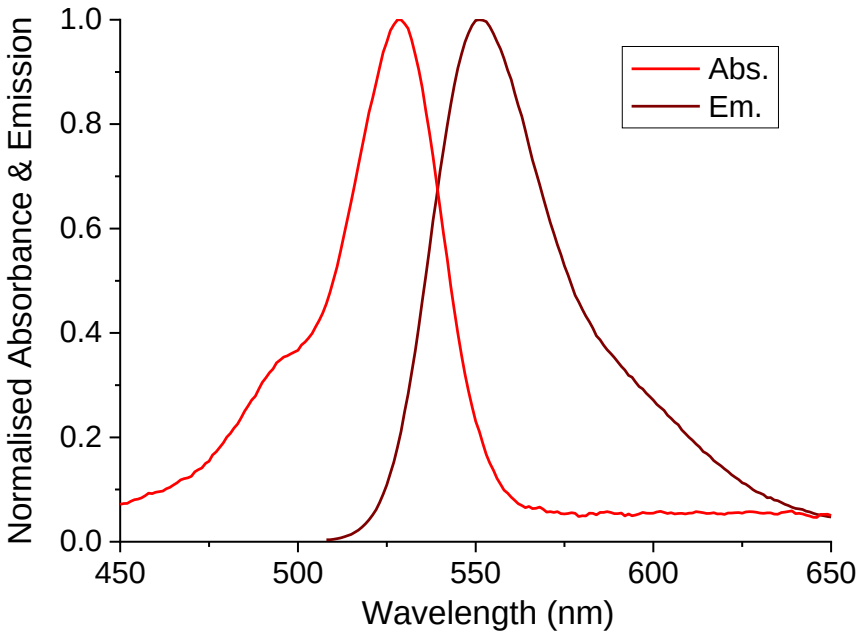

Figure 2.2: Normalised absorbance and fluorescence emission of Rhodamine 6G, showing the Stokes shift in peak wavelength position caused by the lower energy of the emitted photons.

2.1.2 Quantum Yield & Fluorescence Lifetime

An important characteristic of a fluorophore is its quantum yield. The quantum yield is the ratio of the number of photons emitted from a fluorophore to the number of absorbed photons, which can be expressed in terms of the intramolecular processes via:

$$\Phi = \frac{k_r}{k_r + k_{nr}} \tag{1}$$

where Φ is the quantum yield, k_r is the radiative decay rate and k_{nr} is the non-radiative decay rate, where the sum of $k_r + k_{nr}$ equates to the total decay rate. The efficiency of a fluorophore is often determined by its quantum yield, where a higher quantum yield means a higher number of the absorbed photons are emitted. It is very difficult however to directly measure the quantum yield of a fluorophore, where to do so an integrating sphere is typically required in order to collect all photons emitted from a sample in all directions.

The fluorescence lifetime is another important characteristic of a fluorophore, which can be defined as the average length of time a molecule spends in its excited state before emission of a photon and returning to the ground state. For a population of molecules *M* that are brought to the excited state at time 0 through absorption of photons, the molecules can return to the ground state via radiative or non-radiative transitions, where the rate at which these decay from the excited state is given by:

$$\frac{d[M^*]}{dt} = -(k_r + k_{nr})[M^*] \tag{2}$$

where M^* is the concentration of molecules in the excited state. Integrating this equation describes the evolution of the decay of these molecules over time following δ-function excitation at time 0:

$$i(t) = i(0)\exp\left(-\frac{t}{\tau_f}\right) \tag{3}$$

where $i(t)$ gives the fluorescence intensity, as this is proportional to the concentration of molecules in the excited state at any given time after excitation at time 0, $i(0)$ is the intensity immediately following excitation, and τ_f is the characteristic fluorescence lifetime of the fluorophore. Fluorescence lifetimes are generally on the nanosecond timescale and can be defined in terms of the intramolecular processes as:

$$\tau_f = \frac{1}{k_r + k_{nr}} \tag{4}$$

Since the emission of a photon is a random process, the fluorescence lifetime is an average time the molecules spend in the excited state, as very few molecules will emit a photon at exactly $t = \tau_f$.

2.1.3 Fluorescence Quenching

Fluorescence quenching refers to processes that can decrease the fluorescence intensity of a sample. Such quenching can occur through various mechanisms, some of which include the formation of complexes in the ground state (static quenching), excited state reactions, energy transfer and collisional quenching. Collisional quenching is one of the most commonly observed quenching processes, which involves the deactivation of a fluorophore in the excited state through contact with a quencher molecule. Collisional quenching can often be described by the Stern-Volmer equation:

$$\frac{F_0}{F} = 1 + K[Q] = 1 + k_q \tau_0 [Q] \tag{5}$$

where F_0 and F correspond to the fluorescence intensities in the absence and presence of a quencher respectively, K is the Stern-Volmer quenching constant which gives an indication of how sensitive the fluorophore is to a quencher, k_q is the biomolecular quenching constant, τ_0 is the unquenched lifetime and $[Q]$ is the quencher concentration. While many molecules can act as collisional quenchers, one of the most efficient and well-known quencher molecules is oxygen, giving rise to the use of various fluorophores as O_2 sensors[80].

Another common and now popularly utilised mechanism of quenching is Förster Resonance Energy Transfer (FRET). Instead of direct contact between the molecules, FRET involves an energy transfer between a donor molecule *D* in the excited state and an acceptor molecule *A* in the ground state through dipole-dipole interactions. A spectral overlap of the donor emission and acceptor absorption is required for FRET, where the rate of energy transfer depends on the extent of the spectral overlap as well as other factors such as the orientation of the transition dipoles and the distance between the donors and acceptors. The rate of energy transfer k_{DA} is given by:

$$k_{DA} = \frac{1}{\tau_D} \left(\frac{R_0}{r}\right)^6 \tag{6}$$

where τ_D is the fluorescence lifetime of the donor in the absence of the acceptor, R_0

is the Förster distance at which the energy transfer efficiency of the D-A separation is 50%, and r is the D-A separation. The FRET rate is proportional to $1/r^6$, making it extremely sensitive to the distance between the molecules. This sensitivity to the distance between the molecules allows for the use of FRET as a "spectroscopic ruler", where it has gained substantial interest in recent years for the study of intermolecular distances in biomolecules[81].

2.2 Fluorescence Techniques & Instrumentation

Both steady state and time-resolved fluorescence techniques have been utilised throughout this work to study the properties of fluorophores in various environments. Steady-state measurements commonly refer to the continuous illumination of a sample and recording the fluorescence emission over a wavelength range, and time-resolved measurements employ pulsed light sources for excitation and the fluorescence intensity decay is recorded. Steady-state measurements are important to undertake first to understand the fundamental fluorescence properties of a sample, however time-resolved measurements can reveal greater molecular information such as the shape and flexibility of a macromolecule, conformational changes, the rate of energy transfer between molecules, as well as distinguishing between different excited state processes and environments[75]. The main techniques and instrumentation used for the steady-state and time-resolved measurements presented in this thesis are discussed here.

2.2.1 Absorbance & Fluorescence Spectroscopy

A complimentary technique to fluorescence spectroscopy is UV-Vis spectroscopy, which has also been utilised in this work. UV-Vis spectroscopy involves the measurement of the amount of light absorbed by a sample over a given wavelength range. This measurement is commonly undertaken first when studying a new molecule of interest, as this can provide information on a suitable excitation wavelength for subsequently recording the fluorescence emission if the sample is

unknown. UV-Vis measurements were performed on a PerkinElmer Lambda 2 UV-Vis spectrometer, where the typical setup and optical path of such a spectrometer is shown in Figure 2.3.

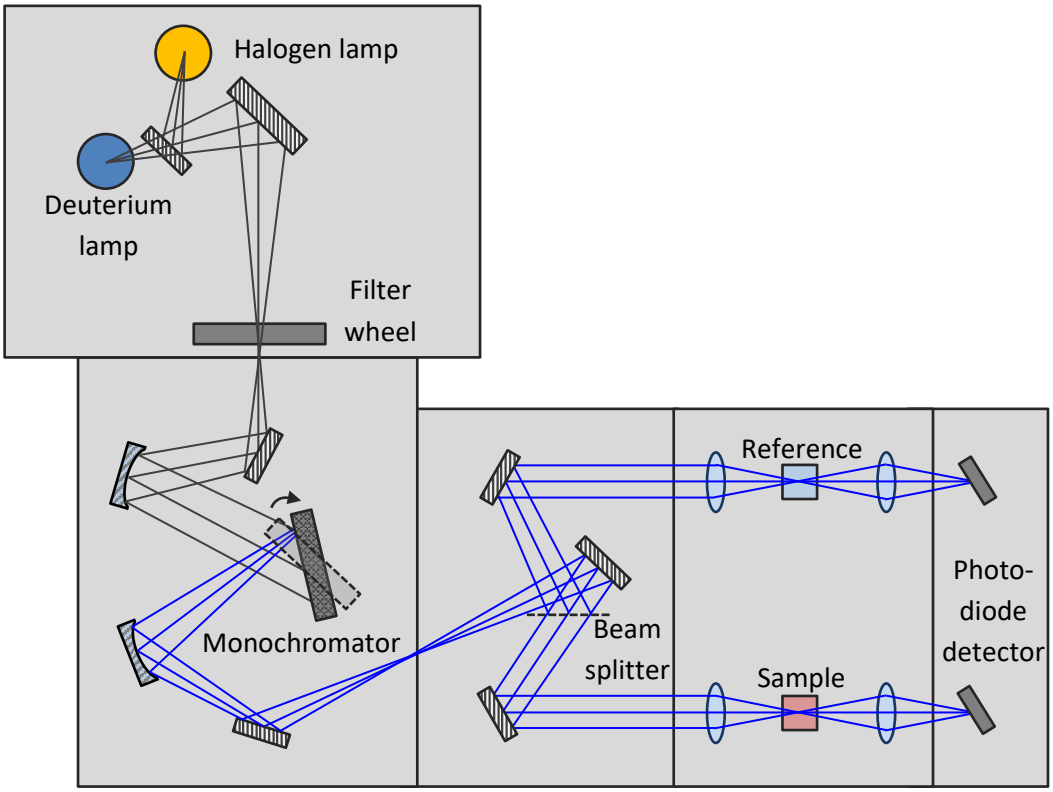

Figure 2.3: Schematic diagram for the PerkinElmer Lambda 2 UV-Vis spectrometer.

Two light sources are required in the UV-Vis spectrometer, which include a deuterium lamp for measuring in the UV range of 190 – 330 nm and a halogen lamp for measuring in the visible range of 330 – 1100 nm. Light from the source is focused through the entry slit to the monochromator, which is used to scan through the wavelength range of light chosen to be focused on the sample through the exit slit. The light is reflected onto the beamsplitter to allow half the light to be focused onto the cuvette containing the sample of interest, and the other half focused onto the cuvette containing the reference sample. The light that passes through each cuvette to reach separate photodiode detectors. The absorbance of a sample $A(\lambda)$ can be written as:

$$A(\lambda) = \log_{10}\left(\frac{I_0(\lambda)}{I(\lambda)}\right) = -\log_{10} T(\lambda) \quad (7)$$

where $I_0(\lambda)$ is the incoming light intensity, $I(\lambda)$ is the transmitted light intensity and $T(\lambda)$ is the transmission. The absorption spectrum helps determine wavelengths for excitation, where wavelengths that exhibit high absorption are usually desired for collecting fluorescence emission in later measurements. The Beer-Lambert law describes how light is absorbed by a sample and its proportionality to the concentration c and path length l, and is given by:

$$A = \varepsilon c l \quad (8)$$

where ε is the absorption coefficient (with units $L\ mol^{-1}\ cm^{-1}$). The linear relationship between absorbance and concentration in the Beer-Lambert law means it can be utilised to calculate unknown concentrations of known molecules.

The spectrofluorometer used to collect fluorescence emission spectra from samples was the HORIBA FluoroMax-2, where the typical setup is shown in Figure 2.4. For fluorescence measurements on the FluoroMax-2 a xenon lamp is used as the light source, where the light passes through a monochromator in order to select the desired wavelength of excitation for the sample. This excitation wavelength is kept constant to collect emission spectra. Prior to reaching the sample, ~ 8% of the excitation light is directed to the reference photodiode in order to measure any fluctuations in the light source intensity. Fluorescence emission from the sample is collected perpendicularly to the excitation arm to minimise excitation light being collected by the detector. The emission from the sample passes through a second monochromator which scans across the desired wavelength range before reaching the photomultiplier (PMT) detector. Wavelength correction factors are applied to the raw data collected for both the reference signal at the reference photodiode and the signal from the PMT detector to correct for intensity fluctuations of the excitation source, wavelength dependencies of the system optics as well as dark counts.

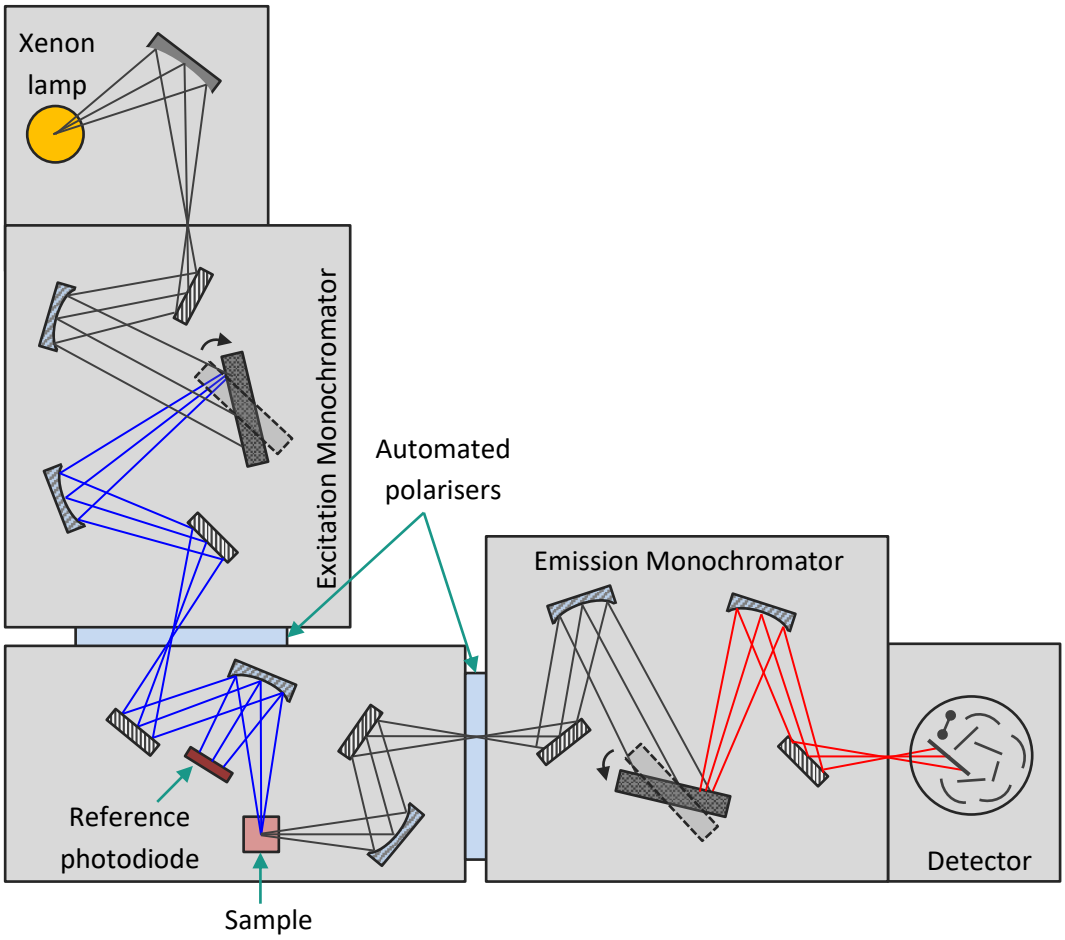

Figure 2.4: Schematic diagram for the HORIBA FluoroMax-2 fluorescence spectrometer.

2.2.2 Fluorescence Lifetime Spectroscopy

Time-resolved fluorescence spectroscopy involves the measurement of the time a molecule remains in its excited state, also known as fluorescence lifetime spectroscopy. Fluorescence lifetime measurements can provide additional information about a system compared to emission measurements alone, and offer advantages such as the ability to discriminate against scattered light and other endogenous fluorophores, as well as typically being independent of photobleaching and wavelength which can often affect fluorescence intensity measurements[82]. Fluorescence lifetime spectroscopy can be performed either in the time-domain (pulse fluorometry) or frequency-domain (phase modulation fluorometry)[83]. When measuring in the frequency-domain, the intensity of the excitation light is modulated at a high frequency. This results in a fluorescence emission that is also intensity

modulated at the same frequency, however it is phase-shifted and will have a decrease in modulation depth in comparison to that produced by the excitation light[75]. These properties are determined by the fluorescence lifetime of the sample; therefore the lifetime can be calculated by measuring the change in phase and modulation depth. While frequency-domain measurements have their own advantages such as rapid acquisition time[84], the work presented in this thesis instead utilises time-domain fluorescence lifetime measurements, which is discussed in greater detail below.

2.2.2.1 Time Correlated Single Photon Counting

The main technique used in this project for investigating fluorescence lifetimes is Time Correlated Single Photon Counting (TCSPC). TCSPC is a sensitive measurement technique allowing for the measurement of fluorescence decays on the nanosecond timescale. The TCSPC process and equipment setup required to measure the fluorescence lifetime are shown in Figure 2.5 and Figure 2.6 respectively.

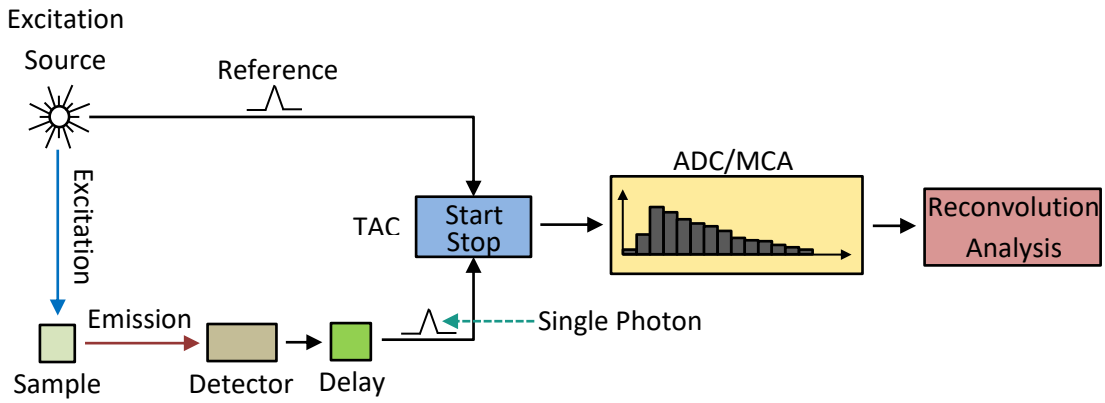

Figure 2.5: TCSPC process used for obtaining fluorescence decays. A light pulse from the excitation source starts the timing electronics which are then stopped by the detection of a fluorescence photon. This difference in times is converted to a corresponding voltage, to a digital signal and then stored as a photon count event in a histogram.

TCSPC involves monitoring the detection and arrival time of all photons after excitation of a sample, where an excitation source such as an LED or laser diode is used to produce a light pulse which starts the timing electronics. The timing electronics are then stopped by a signal produced by the PMT detector upon

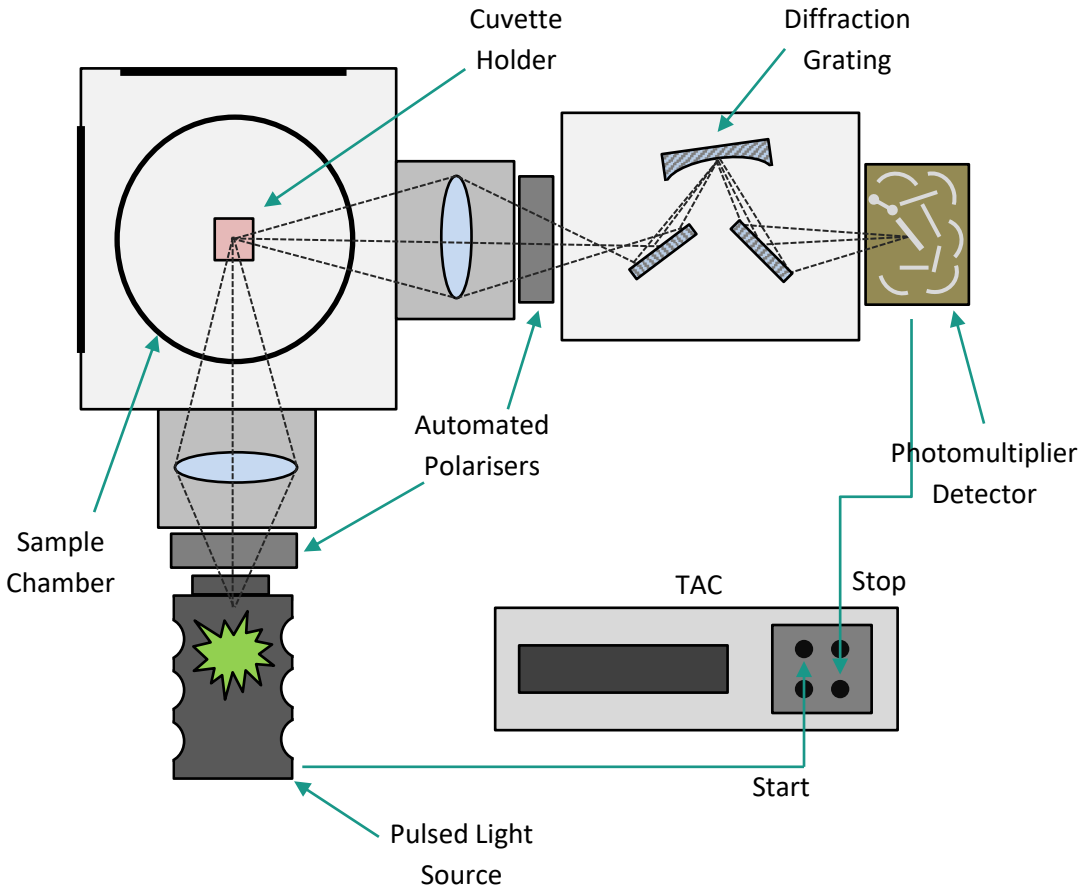

Figure 2.6: Equipment setup for the HORIBA DeltaFlex system for fluorescence lifetime measurements.

detection of a fluorescence photon emitted from the sample. The arrival time of the fluorescence photon at the detector is measured in reference to the start pulse by a time-to-amplitude convertor (TAC). The TAC produces an analogue voltage through the charging of a capacitor which is proportional to the elapsed time between the start and stop signals. The time between a stop signal being detected and the next start signal being received is known as the dead time, where photons arriving in the dead time will not be counted. If a photon is not detected within the given TAC range, the TAC is reset for the next start signal. When a photon is detected, the analogue signal is converted to a digital signal through an analogue-to-digital convertor (ADC), where a multi-channel analyser (MCA) measures these voltages and stores them as detection photon count events. Only one conversion of a detected photon to a corresponding voltage can occur per cycle, therefore if any later photons arrive in the same cycle, these will be disregarded by the electronics. If this is not minimised this can create a bias towards the first detected photons and therefore

shorten the fluorescence decay. This is known as the pile-up effect[85]. To ensure this bias does not exist, only 1 – 2 photons are detected per 100 excitation events which is achieved experimentally by creating a stop-to-start rate ratio (α value) of < 2%[86] using neutral density filters. To produce a fluorescence decay curve, this process is repeated thousands of times until a set amount of counts has been detected (typically 10,000 counts in the peak bin) so the MCA can construct a histogram of photon counts vs. time, where each histogram bin has a fixed time width.

The typical experimental setup for TCSPC shown in Figure 2.6 is based on a HORIBA DeltaFlex system, which incorporates a monochromator on the emission arm for selecting the emission wavelength of interest. Each arm also incorporates polarisers, where for fluorescence lifetime measurements the polariser on the excitation arm is typically set to 0° and the polariser of the emission arm is set to the magic angle (54.7° for square geometry) to remove polarisation effects[87]. The magic angle condition is important to implement when polarised excitation sources are used – if the excitation source is unpolarised or filters and not diffraction gratings are used for wavelength selection then magic angle conditions are not required[88]. The system is typically operated in forward mode, where the excitation source is connected to the 'Start' input to provide the start signal for the electronics. Forward mode triggers the timing electronics with every excitation pulse, and so for a photon detection rate of 1% only one excitation pulse in 100 will lead to a photon being detected. This means that the timing electronics go through the cycle and dead time the other 99 times with no detection of a photon. Reverse mode can be employed when the dead time of the timing electronics is considerably long, which instead only triggers the timing electronics upon detection of a photon meaning the system only undergoes the dead time for this photon event rather than for every excitation pulse. In this mode the detector is instead connected to the 'Start' input to produce the start signal. The timing electronics of the system used and shown in Figure 2.6 are suitably fast enough for the system to operate in forward mode.

The instrumental response function (IRF) is also recorded for analysis of fluorescence lifetime measurements, which represents the response of the instrument to a sample with no lifetime and in turn the shortest profile that is measurable by the

system[75]. In an ideal setting, the IRF would resemble a δ-function, however the width of the IRF is often broadened due to the characteristics of the excitation sources as well as the optical and electronic components of the instrument[75]. To obtain the IRF, Rayleigh scattering from a dilute LUDOX SM-AS silica solution is typically measured, where both the excitation and emission polarisers of the instrument are set to a vertical position.

2.2.2.2 Fluorescence Lifetime Data Analysis

Since the IRF in practice does not resemble a δ-function and is broadened as a result of the instrument components, the fluorescence decay obtained in measurements is in fact a convolution of the fluorescence impulse response, $i(t)$, and the IRF, $P(t)$ (blue curve in Figure 2.7). The excitation pulse can be considered as a series of δ-functions. Each δ-function produces a decay response starting at different delay times with an intensity proportional to the height of the corresponding δ-function. Together these responses produce a linear sum that is representative of the measured decay[75]. The convolution can be expressed by the following:

$$F(t) = \int_0^t P(t')\, i(t-t')dt' = P(t) \otimes i(t) \tag{9}$$

where $F(t)$ is the expected fluorescence decay, the variable t' is a moving time delay that corresponds to the point in time where each δ-function of the IRF generates a fluorescence response[89], and $\otimes$ denotes convolution. The term *re*convolution analysis, which is used to determine fluorescence lifetimes, comes from the iterative process applied to the term $i(t-t')$ from Equation 9. This term is iterated in order to find the value of τ_f from Equation 3 (in the simplest monoexponential case) that produces a function $F(t)$ which best describes the acquired data. Nonlinear least squares (NLLS) fitting is used to determine $F(t)$, which starts with an assumed model and parameters that will describe the data. The model used by the analysis software to find the fluorescence lifetimes is given by:

$$F(t) = A + B_1 \exp\left(-\frac{t}{\tau_{f1}}\right) + \cdots + B_n \exp\left(-\frac{t}{\tau_{fn}}\right) \quad (10)$$

where n is the number of exponential components required to fit the data and therefore the number of species present in the sample with different fluorescence lifetimes, A is a background offset, and B is the pre-exponential function corresponding to the amount of each emitting species there is. The B values are given as both a relative amplitude, which is weighted by the lifetime, and as a normalised value providing information on the relative concentration of species in the sample.

The goodness of fit of the model and parameters can be expressed as a chi squared (χ^2) value calculated from the following equation:

$$\chi^2 = \sum_N \left[\frac{Y(i) - F_d(i)}{\sigma(i)}\right]^2 \quad (11)$$

where $Y(i)$ is the measured data (red curve in Figure 2.7), $F_d(i)$ is the fitted function (green curve in Figure 2.7, where the term $Y(i) - F_d(i)$ corresponds to the deviation of the model from the decay at each channel), $\sigma(i)$ is the expected standard deviation, which can be expressed as $\sqrt{Y(i)}$ due to the use of Poisson statistics, and N is the number of data channels used in the analysis. A χ^2 value of 1 obtained from a fit would be considered the most ideal, however it is generally accepted that a value of $0.9 < \chi^2 < 1.2$ can be considered a good fit, where $\chi^2 > 1.2$ usually suggests that an incorrect model is being used to describe the data[90].

The weighted residuals, W_t, as shown in Equation 12 and Figure 2.7 that are obtained from a fit can also be used to assess the goodness of fit:

$$W_t = \frac{Y(i) - F_d(i)}{\sigma(i)} \quad (12)$$

A random distribution of the residuals indicates a good fit, where non-random residuals can indicate that an additional exponential component may be required to

describe the data or that systematic effects are interfering with the measurement. A typical decay curve, IRF and the corresponding residuals for a good fit obtained from reconvolution analysis are shown in Figure 2.7 as an example.

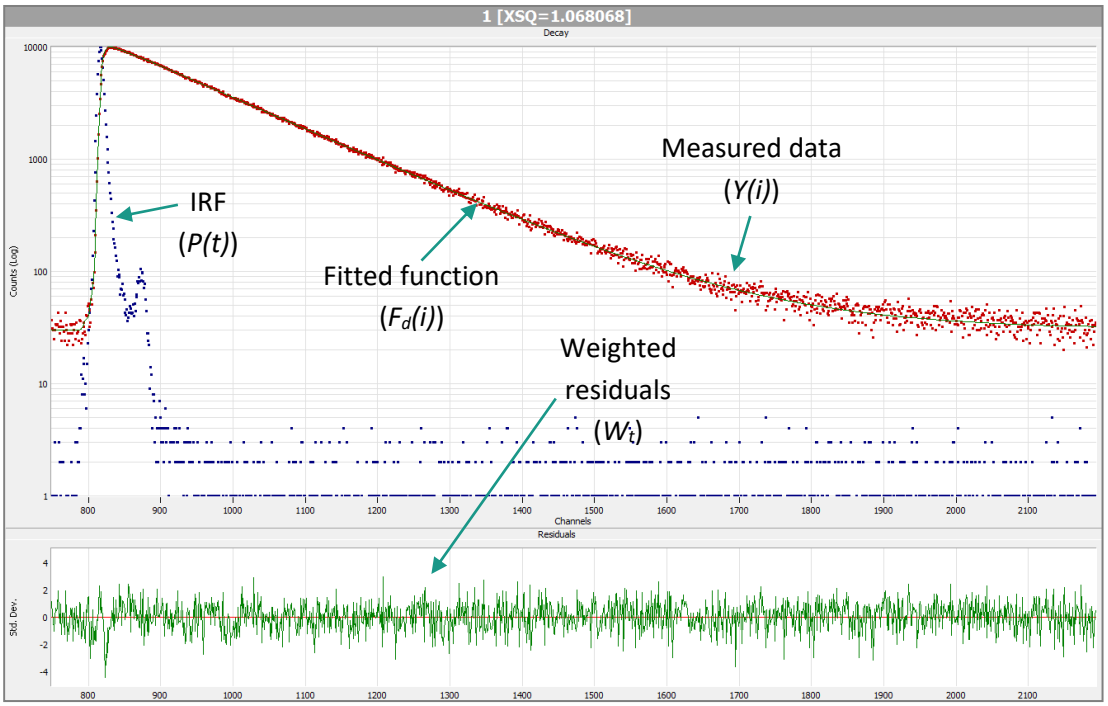

Figure 2.7: Typical fluorescence decay curve (red), the fitted function to the experimental data (green in top window), the IRF (blue) and the corresponding weighted residuals indicating a good fit obtained using reconvolution analysis.

2.2.3 Time-Resolved Emission Spectra

TCSPC can also be used for the measurement of time-resolved emission spectra (TRES). TRES consists of the measurement of the fluorescence decays over a range of emission wavelengths incremented in fixed steps, where decays are typically obtained for a predetermined time at each emission wavelength. The acquired data can provide further information on a system than what would be obtained from one decay measurement alone as it allows for the resolution of overlapping spectra. The emission spectra at different times during the decay can be obtained from the profile created by the peak positions of each decay at the time of interest, where differences – if they exist – in the spectra for shorter- and longer-lived species may be observed[90]. Reconvolution can also be applied to resolve the spectra corresponding

to the different decay times of the species present in a sample using global analysis. All the obtained decays are combined and analysed as one to find common lifetimes, where these lifetime components are then fixed and fitted to each decay curve individually to therefore determine the corresponding pre-exponential factors for each decay curve at each emission wavelength. These pre-exponential factors weighted by the lifetime can be plotted against the wavelength to produce the emission spectrum corresponding to each decay component.

2.2.4 Time-Resolved Fluorescence Anisotropy

Time-resolved fluorescence anisotropy is another powerful technique that measures the depolarisation of the fluorescence emission from a sample. Fluorescence anisotropy can be used in applications such as measuring the rotation of molecules, probing the local viscosity and monitoring conformational changes in molecules such as proteins[92], where in this work it has been utilised for the characterisation of nanoparticles on the ~ 1 – 20 nm scale and for tracking the growth of silica gels to also be used in this work as tissue phantoms by measuring the fluorescence anisotropy of dye molecules attached to nanoparticles undergoing Brownian rotation[61].

The same system as shown in Figure 2.6 can be used for anisotropy measurements. In this case the excitation polariser is set to a vertical position, resulting in a population of molecules whose absorption dipoles align with the vertically polarised light to be excited. These molecules will randomise again becoming unpolarised, where this depolarisation is measured by recording vertically and horizontally polarised decay curves denoted by I_{VV} and I_{VH} respectively. The typical geometry for fluorescence anisotropy measurements is shown in Figure 2.8.

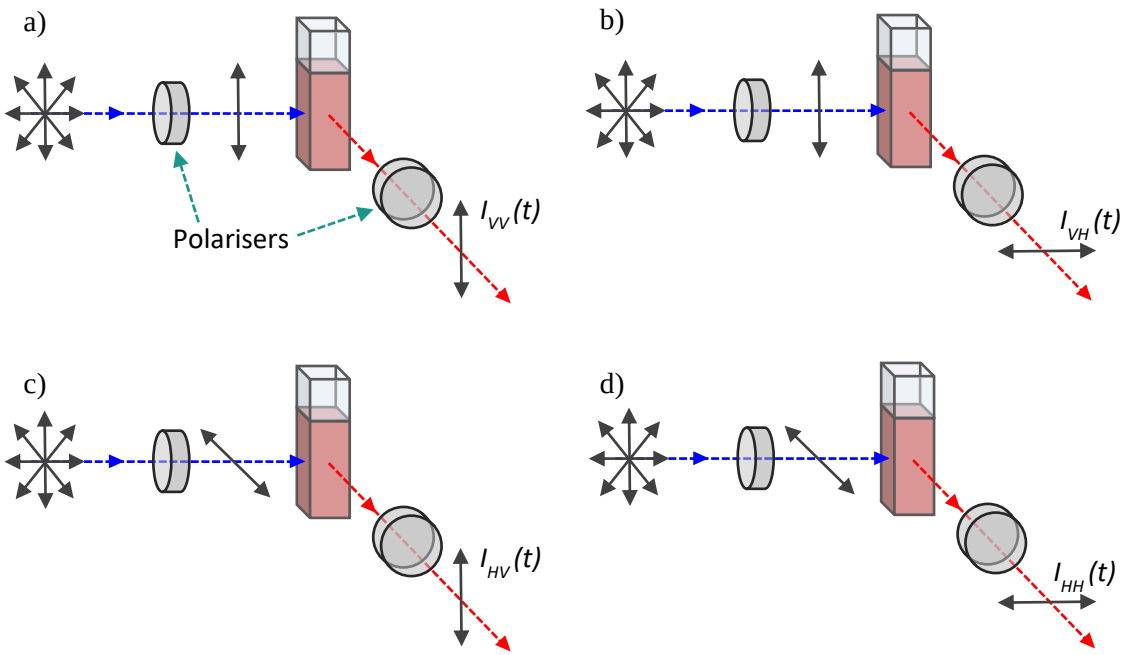

Figure 2.8: Geometry for fluorescence anisotropy measurements and the corresponding polarisations of light as it passes through the polarisers, where a) and b) show the configurations for decay curves I_{VV} and I_{VH} which are typically measured to ~ 10,000 counts difference in the peak of the two decays, and c) and d) for I_{HV} and I_{HH} to calculate the G-factor, which are typically measured to ~ 1000 counts in the peak of each of these curves.

Measurements of I_{VV} and I_{VH} are typically recorded until a peak difference of ~ 10,000 counts between the two curves has been reached. A time-resolved anisotropy function *R(t)* can be generated from the vertically and horizontally polarised decay curves obtained from the measurements to describe the depolarisation of fluorescence due to Brownian rotation through:

$$R(t) = \frac{[I_{VV}(t) - GI_{VH}(t)]}{[I_{VV}(t) + 2GI_{VH}(t)]} \tag{13}$$

where $G = I_{HV}(t)/I_{HH}(t)$ and is a correction factor that corrects for transmission efficiencies of the two emission polarisations[93], which is determined through measurements of the sample with the excitation polariser at a horizontal position and the emission polariser at both a vertical and horizontal position. The *G*-factor measurements are typically recorded until a peak of ~ 1000 counts has been reached for each decay curve, where the geometry for these measurements is also shown in Figure 2.8. A factor of 2 is included in the denominator due to depolarisation not

being detected in the direction of excitation but is identical to what is measured from I_{VH} in the emission channel. The denominator also describes the fluorescence decay of the sample as all three planes of polarisation are accounted for[89].

For anisotropy data analysis, NLLS reconvolution as described in Section 2.2.2.2 is applied firstly to the denominator in Equation 13, yielding the fluorescence decay parameters as usually acquired from a lifetime fit obtained from Equation 10. The fit of this data can be more difficult however due to the larger number of counts present. Once a suitable fit to this data has been acquired, Equation 13 can be rearranged to give:

$$d(t) = I_{VV}(t) - GI_{VH}(t) = R(t) \otimes [I_{VV}(t) + 2GI_{VH}(t)] \quad (14)$$

where the difference data *d(t)* can be fit to iteratively again using NLLS reconvolution analysis to find *R(t)* based on the lifetime parameters found from the fit of $I_{VV}(t) + 2GI_{VH}(t)$ previously, where *R(t)* describes the rotational kinetics in terms of the minimum number of rotational correlation times and associated amplitudes needed to describe the difference data. The χ^2 goodness-of-fit criterion described previously can also be applied here, where a value $\chi^2 < 1.25$ is usually taken to be an acceptable fit in both cases.

In the simplest case of a spherical rigid rotor in an isotropic medium where all the dye is rigidly attached to the nanoparticle, *R(t)* describes the fluorescence depolarisation due to Brownian rotation of the nanoparticle given by:

$$R(t) = R_0 \exp\left(-\frac{t}{\tau_r}\right) \quad (15)$$

where R_0 is the initial anisotropy and in practice is usually < 0.4[94] and τ_r is the rotational correlation time of the nanoparticle which can be described by the Stokes-Einstein equation:

$$\tau_r = \frac{\eta V}{k_B T} \quad (16)$$

where η is the microviscosity, T is the temperature, k_B is the Boltzmann constant and V is the hydrodynamic volume $4\pi {r_p}^3/3$ of the nanoparticle defined by the hydrodynamic radius r_p, where V can be substituted into Equation 16 and the hydrodynamic radius can be found from the rearranged equation:

$$r_p = \left(\frac{3k_B T \tau_r}{4\pi\eta}\right)^{1/3} \tag{17}$$

In the case of the dye being in two different environments e.g. being freely rotating (τ_{r1}) and bound (τ_{r2}) to the nanoparticle, the anisotropy function can be described by:

$$R(t) = (1-f)R_0 \exp\left(-\frac{1}{\tau_{r1}}\right) + fR_0 \exp\left(-\frac{1}{\tau_{r2}}\right) \tag{18}$$

where f is the fraction of fluorescence associated with the rotational correlation time τ_{r2} of the dye bound to the nanoparticle, and $1 - f$ the corresponding fraction for τ_{r1} of the dye rotating freely. This case represents the most complex model that can be analysed in this work, as this is limited by the DAS6 software used for analysis which also assumes all species present in the sample are spherical.

2.2.5 Fluorescence Lifetime Imaging Microscopy

Fluorescence lifetime imaging microscopy (FLIM) is another powerful fluorescence technique that has gained a lot of interest in recent years for biological applications in particular. As previously discussed for fluorescence lifetime spectroscopy measurements, FLIM images can be taken in both the time domain using TCSPC as previously described as well as using time-gated cameras, or in the frequency domain by measuring the phase shift and demodulation[95]. While working in the frequency domain allows for faster acquisition, the work in this thesis focuses on time-domain imaging which has advantages such as the ability to resolve data more easily from weakly emitting fluorophores as well as being more flexible in terms of measurable time ranges that can be achieved[96].

Fluorescence intensity imaging can also be used for biological studies, where the associated instrumentation is often far cheaper than that required for FLIM. However, information is limited when using intensity-based imaging due to the dependence on fluorophore concentration, photobleaching, and quenching factors that can affect the emission from a probe[97]. In addition to these factors, FLIM allows for the resolution of multiple fluorophores with varying lifetimes that may fluoresce at the same wavelength and would therefore be indistinguishable using intensity-based imaging alone. A FLIM image is therefore based on the contrast produced by the different fluorescence lifetimes within a sample rather than the emission intensity. Since the fluorescence lifetime of a fluorophore depends on its environment but not on its concentration, FLIM becomes an advantageous technique to study various environmental and molecular effects independent of these factors[75], where examples include the interactions between proteins, FRET-based studies, changes in lifetime upon binding to biological targets, and pH sensing in different cellular environments[98]. The first breakthrough in FLIM imaging came in 1988 when an ultrafast pulsed laser was used in combination with a laser scanning microscope and TCSPC, which was used to generate FLIM images of porphyrins in live cancer cells[99]. Since then many variations of FLIM imaging have been developed, including time-gated FLIM which is a wide-field technique where a time-gated camera is used to sample a fluorescence decay at several delays after the excitation pulse[100], stimulated emission depletion (STED)-FLIM that incorporates a secondary beam to deplete the excited state population via stimulated emission to suppress fluorescence outside the focus which can in turn be used to overcome the classical diffraction limit[101], as well as two photon FLIM where using a laser with femtosecond pulse widths can produce two-photon absorption to excite a fluorophore, allowing for deeper penetration into samples as well as suppressing background fluorescence[75].

In the work presented in this thesis FLIM measurements were made using the prototype HORIBA Lifetime Imaging Camera based on the QuantiCam single photon avalanche diode (SPAD) camera. A SPAD is a photodiode with a p-n junction that is reverse biased at a voltage exceeding its breakdown voltage. When a single photon reaches the active device, an electron-hole pair is created which then triggers a self-sustaining avalanche of secondary carriers[39,102]. The generated current

rises quickly to a steady level in the order of milliamperes, where the leading edge of the pulse indicates the arrival time of the photon if the primary carrier is photo-generated[102]. Appropriate electronics are required to detect the leading edge of the avalanche pulse, lower the SPAD bias to below the breakdown voltage to quench the avalanche and reset the photodiode to operating levels[102]. An array of suitable SPADs can be created to then produce a SPAD imager. The equipment setup for the HORIBA Lifetime Imaging Camera which utilises such a SPAD array is shown in Figure 2.9.

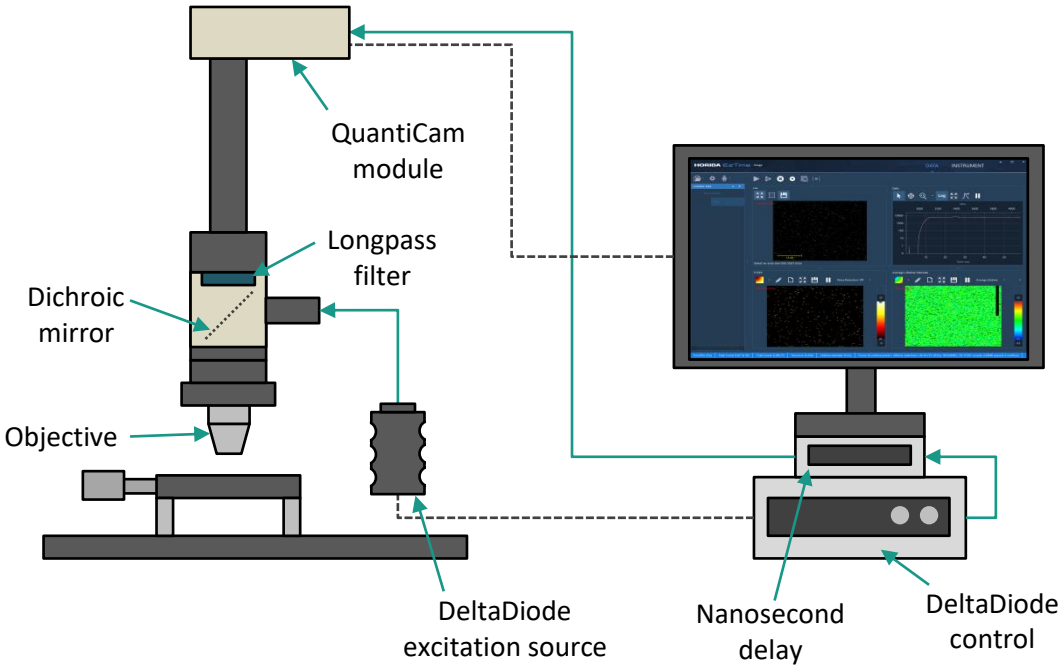

Figure 2.9: System setup for use of the QuantiCam Lifetime Imaging Camera and EzTime software for data acquisition

In the setup shown in Figure 2.9 a DeltaDiode pulsed laser diode sources is used for excitation of samples, allowing for repetition rates of up to 100 MHz. Excitation light reaches the dichroic mirror which will direct the light towards the sample via the 20x objective, which also collects the fluorescence signal from the sample. The fluorescence signal is transmitted through the dichroic mirror where it then also passes through a longpass filter for emission wavelength selection before reaching the QuantiCam. The QuantiCam is a complementary metal-oxide semiconductor (CMOS) fabricated 192 x 128 pixel SPAD array, where each individual SPAD has its own TCSPC electronics-based TDC incorporated within the pixel[103,104]. This

SPAD array allows for the rapid collection of fluorescence lifetime data in every one of the 25,000 pixels simultaneously which is fed into the EzTime PC software for collection and data analysis, where this rapid collection of data overcomes the common problem of slow acquisition times with previously developed FLIM techniques. Tail fitting of the decay is employed when lifetime analysis is required instead of reconvolution analysis, as an IRF is not typically measured using this system. The ability to acquire such a considerable amount of lifetime data simultaneously makes this system over an order of magnitude fast than conventional scanning FLIM microscopes, where in combination with the ability to record images at up to 30 frames per second enables real-time video rate studies of mobile samples such as fluid biopsies and fundamental live cell processes, which has not yet been realised in any commercially available systems[105].

3. A Liquid Light Guide-Based Fluorescence Lifetime System

3.1 Introduction

The development of fibre bundles for medical applications first began in 1952 when Harold H. Hopkins started the development of an endoscope based on glass fibre bundles[106]. The first practical prototype of such fibre bundles did not arrive until 1957 when Basil Hirschowitz demonstrated the use of a flexible fibre optic endoscope using clad fibres on a patient[106]. Since then, fibre bundle-based techniques such as endoscopy have been developed for numerous surgical applications including the detection and treatment of various cancers, where the improvement and development of fibre optics in surgery is still of high interest today.

An optical fibre typically consists of three elements as shown in Figure 3.1 – the core, cladding and coating. The fibre optic core material is usually silica glass or plastic, with varying thicknesses depending on the application and modality. The cladding surrounds the core and has a lower refractive index to create an interface that confines the light to the core[107], allowing light to propagate through the fibre via total internal reflection also shown in Figure 3.1. The core and cladding are then covered in a protective coating and sometimes external jacket to prevent damage.

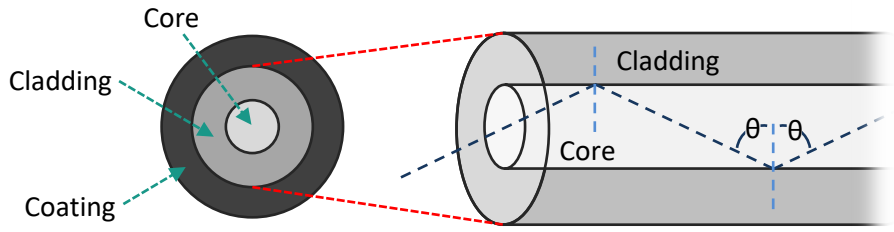

Figure 3.1: Typical fibre optic design consisting of a core, cladding and coating, where light propagates through the fibre via total internal reflection due to the lower refractive index of the cladding in comparison to that of the core.

Optical fibres have many uses in areas such as telecommunications and sensing, however it is their medical applications that are of interest in this work. The most common medical application for optical fibres is in endoscopy, where the fibre bundles in an endoscope can be used to image inside the body. There are many types

of endoscopic procedures that can be used for the detection of various cancers which have been described in Section 1.1.1. The combination of fluorescence with optical fibre-based procedures has also been of interest in recent years. An example of a recent study utilised the FDA-approved fluorophore ICG to determine tumour margins in the pituitary and parasellar regions of the brain using an endoscopic system[108], where another example includes the development of a wide-field fluorescence endoscope for the detection of cathespin proteases, which have been shown to be promising targets in cancer imaging[109]. Studies such as these demonstrate how fluorescence can provide greater accuracy in determining tumour margins compared to standard white light imaging but can still be utilised using well-established techniques such as endoscopy.

Liquid light guides offer an alternative method to silica fibres for the transmission of light. The liquid light guide design is much like a single silica fibre but with a larger core diameter in comparison, where the core consists of a sealed liquid to carry light instead of a conventional glass core. Figure 3.2 shows the basic principle of operation of a liquid light guide, as well as a cross sectional view of the light guide compared to a fibre bundle.

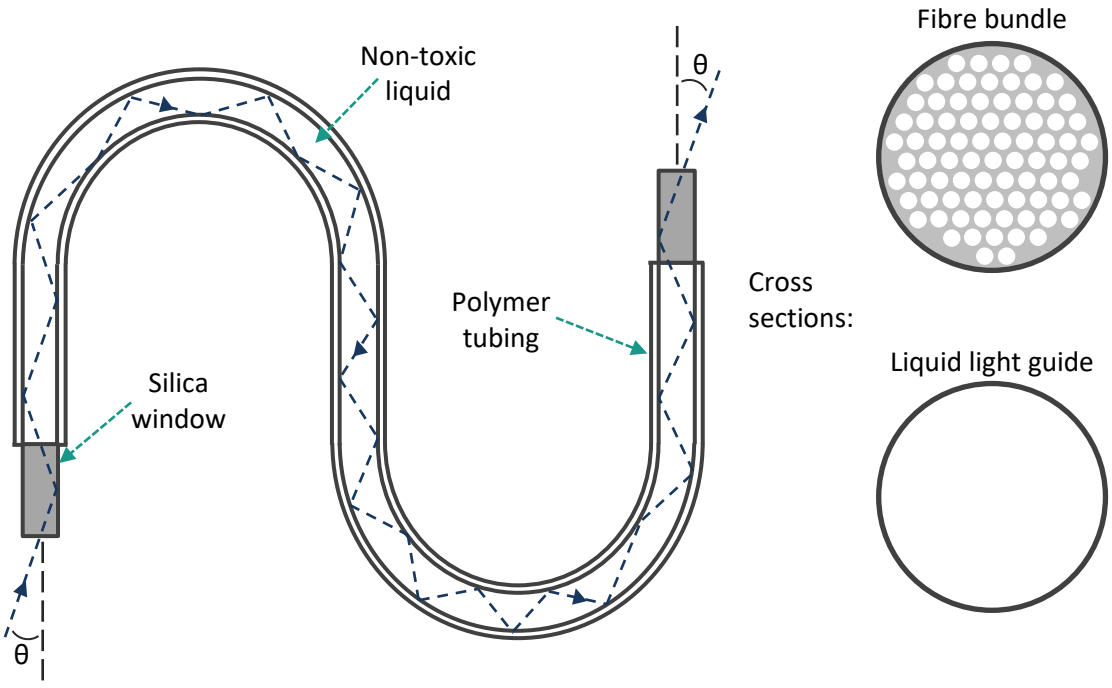

Figure 3.2: Basic principle of operation and design of a liquid light guide, with a comparison of the cross sections to demonstrate how more light can be lost in a fibre bundle. Light also propagates through the light guides via total internal reflection as seen in typical silica fibres.

Liquid light guides have a number of advantages compared to conventional silica fibre-based bundles often used for surgical applications. One advantage is the ability to transmit more light. Since liquid light guides have a cross-section which resembles an open pipe as shown in Figure 3.2, all the space can be used to transmit more light with total reflectance. Fibre bundles instead consist of tens of thousands of fibres (e.g. ~ 50,000 in an endoscope[110]) where there is space in between the individual fibres, and since the space in between the tubes does not transmit light there is a loss of light intensity when these bundles are used for light transmission. Another advantage of liquid light guides is their increased flexibility due to the polymer tubing used. Silica fibres are more prone to breakage when frequently bent[111]; therefore the robustness of liquid light guides makes them potentially more useful for application in surgical procedures. In addition to these factors liquid light guides often have a higher numerical aperture than silica fibre bundles, where the larger acceptance angle means more light can be collected. There may be typical dispersion effects of light travelling through an optical fibre present in a liquid light guide such as modal, material and chromatic dispersion, which are important to bear in mind when analysing the differences in measurements between those taken on the traditional fluorescence lifetime setup – which contains focusing optics – and the liquid light guide-based fluorescence lifetime systems.

Liquid light guides have similar applications to fibre bundles, where they are also being utilised in the research and development of imaging systems for surgery due to the advantages described. An example of their use in surgical research is in the design and development of near-infrared imaging systems that can be used during both laparoscopy and open surgery, where their higher transmission compared to fibre bundles made them more desirable[112]. The high throughput of these light guides has also been utilised for the illumination of breast tissue samples for surgical margin analysis using fluorescence and reflectance spectroscopy[113]. The advantages listed have led to liquid light guides being chosen for implementation in a fibre-based fluorescence lifetime system in this work. The Photophysics Group have previously utilised the advantages of liquid light guides in miniaturised fluorescence lifetime systems where they have been used in a multiplex arrangement allowing for multiple detection channels[114] as well as being implemented in a fluorescence sensor based on

energy transfer for the detection of ions[115]. While this previous work demonstrated the suitability of liquid light guides in miniaturised and more portable fluorescence lifetime systems, the setups were more complex than what is investigated in this chapter, where many developments and improvements have since been made in various components used in fluorescence lifetime systems today. As discussed in Chapter 1 there is a great need for an instrument that can be used intraoperatively to assist surgeons in the assessment of tumour margins, where the development of fluorescence-based instruments has already gained significant interest for such an application[116,117]. To combine the advantages of liquid light guides and fluorescence lifetime techniques, the work presented in this chapter looks to demonstrate the ease of incorporating liquid light guides into a modern fluorescence lifetime system. Fluorescence-based techniques in previous developments for margin estimation often focus on using FLIM[112,118,119]; however in this work we also utilise fluorescence lifetime spectroscopy as a potential tool for calibrating a figure of merit for a lifetime-based instrument for estimating tumour margins. The lifetime system developed and described has been simplified compared to conventional fluorescence lifetime systems for cost-effectiveness, and samples can be measured both 'inside' and 'outside the box', demonstrating the versatility of the system. Measuring samples 'outside the box' in particular makes the system more appropriate for practical applications outside the laboratory, where this system design has been utilised in a later section for measuring phantom tumour margins to demonstrate its use as a calibration tool for margin estimation.

3.2 System Setup with Sample Chamber

3.2.1 Instrument Design & Experimental Setup

Two 1 m liquid light guides were purchased from Newport (model no: 77566), where the light guides chosen had a transmittance range of 340 – 800 nm, a core diameter of 3 mm, and a numerical aperture of 0.59 resulting in an acceptance cone of 72°. The light guides were first integrated into a fluorescence lifetime system consisting

of a conventional HORIBA TemPro and sample chamber, where the schematic and photographs of the finished system are shown in Figures 3.3.

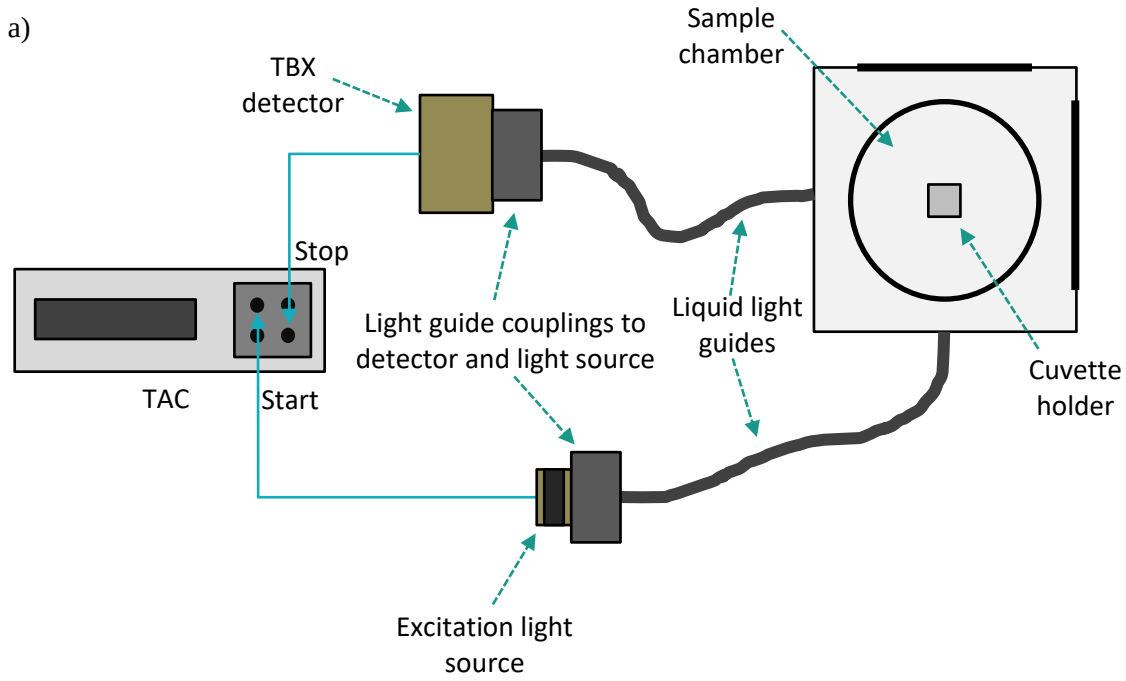

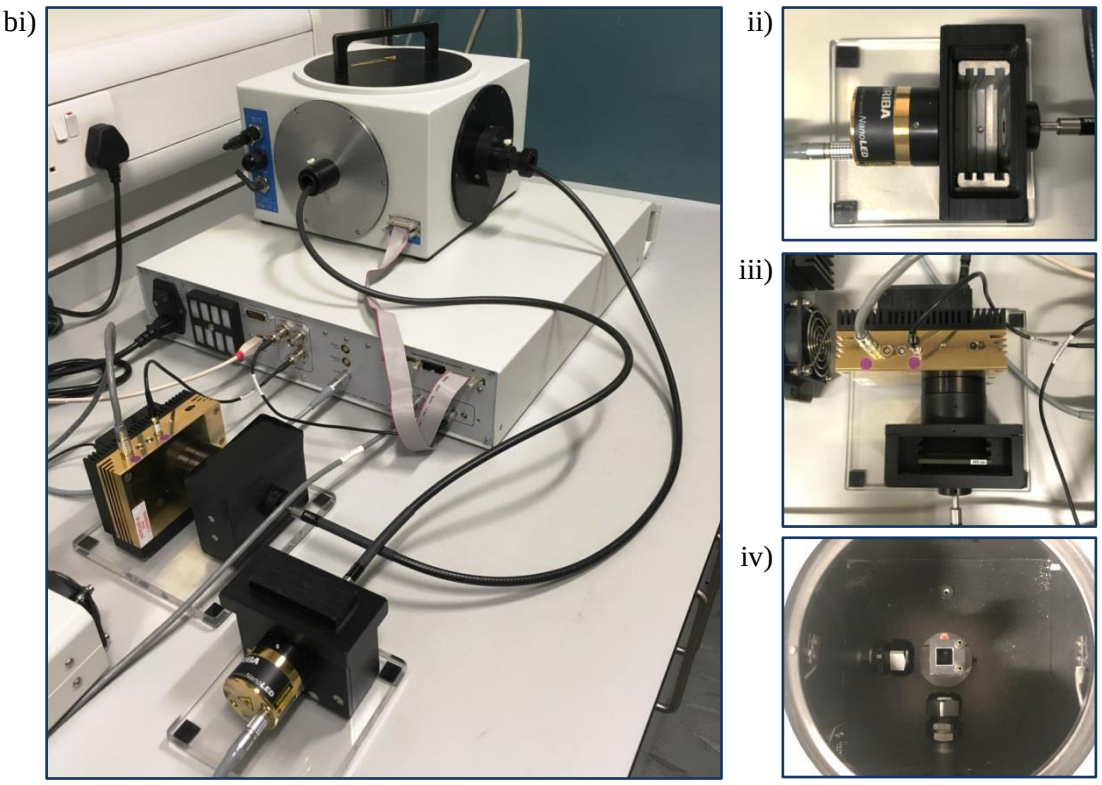

Figure 3.3: a) Schematic of the fluorescence lifetime system incorporating liquid light guides as a means of excitation and collecting fluorescence into an already existing sample chamber, and b) photographs of i) the final setup, with more detailed views of the couplings between the light guides and ii) the excitation source and iii) detector, and iv) the positioning of the light guides within the sample chamber.

The schematic in Figure 3.3 a) illustrates how the liquid light guides were utilised for the measurement of fluorescence lifetimes as a means of transmitting the signal from the excitation source as well as collecting fluorescence from the sample. The excitation source and detector were connected to the TAC start and stop positions on the DeltaFlex system in forward mode as normal. The photographs in Figure 3.3 b) show in more detail the various parts that were designed and produced in order to incorporate the liquid light guides into the system. Figure 3.3 bii) and iii) show the holders designed for coupling NanoLED excitation sources and TBX detectors to the liquid light guides, where each of the couplings had holders for neutral density or longpass filters as required. Each coupling was also designed to be as light tight as possible to minimise the collection of background light. Figure 3.3 biv) shows in more detail how the light guides were coupled to the sample chamber. The original arms of the HORIBA TemPro system were first removed from the sample chamber, where new plates were produced that would hold the light guides securely in place. Swapping out these arms reduced both the size and weight of the overall setup. The positioning of the light guides shown in Figure 3.3 biv) was adjustable, where they could be moved further away or closer to the cuvette holder as desired. Measurements on this system were performed in a dark room to further minimise any background light being collected by the detector.

Comparison fluorescence lifetime measurements were performed on a HORIBA DeltaFlex system, where this system instead utilises monochromators as a means of selecting the emission wavelength for measurements. Monochromators are generally bulky and add a lot of weight to the overall setup; therefore a filter-based system would be more desirable for a setup to be used in applications outside of the laboratory. Both systems utilised the TCSPC technique described previously.

3.2.2 Conventional Fluorophore Measurements

To assess the suitability of the liquid light guide-based system described in Section 3.2.1 for measuring fluorescence lifetimes, several fluorophores were initially measured. Four dyes with varying excitation, emission and lifetime properties were

chosen, which included CG436 (6-methoxy-1-methyl quinolinium bromide), Rhodamine 6G, MeADOTA (*N*-methyl-azadioxatriangulenium tetrafluoroborate) and JA120, where the structure of these fluorophores are shown in Figure 3.4.

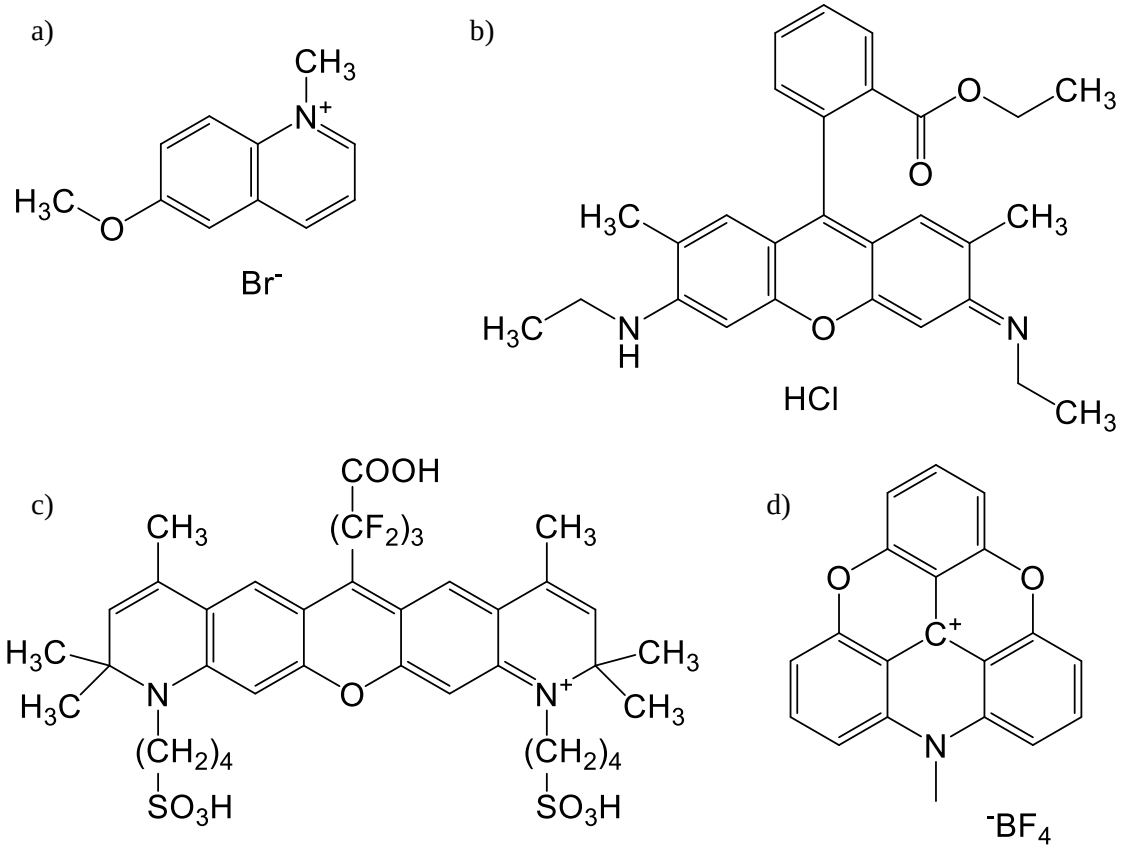

Figure 3.4: Chemical structures of a) CG436, b) Rhodamine 6G, c) JA120 and d) MeADOTA, which were chosen to test the liquid light guide setup over a range of excitation and emission wavelengths as well as range of fluorescence lifetime properties.

The fluorescence lifetime properties of the fluorophores chosen are all documented in literature[61,120–122], therefore results obtained on the liquid light guide system as well as results obtained on a conventional HORIBA DeltaFlex system could be verified quickly. The excitation and emission wavelengths used for these fluorophores ranged from 339 nm (CG436) – 638 nm (JA120) and 440 nm (CG436) – 685 nm (JA120) respectively. The primary fluorophore of interest in this project – NAD(P)H – is excited at 339 nm, therefore measurements of the quinolinium fluorophore CG436 can confirm the system's suitability for excitation in this region. Conversely, JA120 is a xanthene-based probe whose fluorescence properties are towards the NIR region of the spectrum. This is a desirable region of the spectrum to

work in for surgical applications due to the deeper penetration of light into tissue as well as almost no autofluorescence occurring at these wavelengths, therefore it is worthwhile to demonstrate the capabilities of the system in this region as well.

3.2.2.1 Sample Preparation

Each dye used was obtained in powder form, where CG436 was synthesised by a previous student within the Photophysics research group, Rhodamine 6G (R6G) was purchased from Sigma Aldrich, MeADOTA was supplied by collaborators at the University of Copenhagen, and JA120 was supplied by another previous collaborator at the University of Siegen. A small amount of each dye was dissolved in either water (CG436, JA120) or methanol (R6G, MeADOTA), where the volume required of each to obtain an absorbance of ~ 0.1 in 3 mL of solvent was determined. For the purpose of these measurements, an absorbance of ~ 0.1 is strong enough to generate a good fluorescence signal, but not strong enough for dye-dye interactions to interfere[123]. The calculated volume was then added to 3 mL of water for each dye, where the cuvettes were then sealed to perform the fluorescence lifetime measurements.

3.2.2.2 Results & Discussion

The fluorescence decays of each dye were measured on the liquid light guide-based fluorescence lifetime system and the conventional HORIBA DeltaFlex system for comparison. As well as varying in excitation and emission wavelength, these dyes also vary in fluorescence lifetime, where JA120 and R6G have monoexponential decays with short fluorescence lifetimes, and CG436 and MeADOTA have bi-exponential decays with longer fluorescence lifetime components. These dyes were chosen to give a broad range of excitation, emission and fluorescence lifetime properties to test the capabilities of the liquid light guide setup over a ~ 340 – 700 nm range. The excitation and emission wavelengths used for the measurement of each fluorophore can be found in Table 3.1 along with the fluorescence lifetimes

obtained on each of the systems. NanoLED excitation sources were used for each measurement, where a TAC range of 100 ns/200 ns was used for the measurements of JA120 and R6G (100 ns – monochromator-based system, 200 ns – filter-based system), and a TAC range of 400 ns was used for the CG436 and MeADOTA measurements (same TAC range on both systems).

Sample	λ_{ex} **(nm)**	λ_{em} **(nm)**	**System**	τ_1 **(ns)**	B_1 **(%)**	τ_2 **(ns)**	B_2 **(%)**	τ_{avg} **(ns)**	χ^2
CG436	339	440	LLG	17.1 ± 1.0	49.84	27.8 ± 0.5	50.16	21.2	1.11
			Mono.	18.4 ± 1.1	56.95	26.9 ± 0.6	43.05	21.3	1.12
R6G	474	560	LLG	4.01 ± 0.02	100	-	-	4.01	1.10
			Mono.	4.06 ± 0.01	100	-	-	4.06	1.19
Me-ADOTA	494	570	LLG	9.41 ± 0.34	8.63	18.5 ± 0.1	91.37	17.1	1.10
			Mono.	9.74 ± 0.28	2.27	19.1 ± 0.1	97.73	18.7	1.06
JA120	638	685	LLG	1.79 ± 0.01	100	-	-	1.79	1.13
			Mono.	1.75 ± 0.01	100	-	-	1.75	1.09

Table 3.1: Comparison of the fluorescence lifetime components and corresponding relative amplitudes (*B* values) of each component obtained for each sample measured on the liquid light guide (LLG) and monochromator (mono.)-based systems. Note that uncertainties of the lifetime values are provided as a standard deviation by the software where no such value is given for the *B* values, therefore the full value with all digits is given but may not be reliable to the last digits. Typical variation of such *B* values in measurements of the same sample has been found to be ~ 5%. It is also likely that only the first non-trivial digit of the uncertainties given for the lifetime values are significant.

Figure 3.5 shows a comparison of the fluorescence decays of R6G and CG436 on each of the systems as examples, illustrating that the fluorescence decays obtained on the liquid light guide-based system closely resemble those obtained on the conventional monochromator-based system. This is also reflected in Table 3.1 where the lifetime parameters obtained for each of the fluorophores are in good agreement on both lifetime systems, demonstrating that the liquid light guide-based system is capable of obtaining reliable fluorescence lifetime data over a range of wavelengths and time scales.

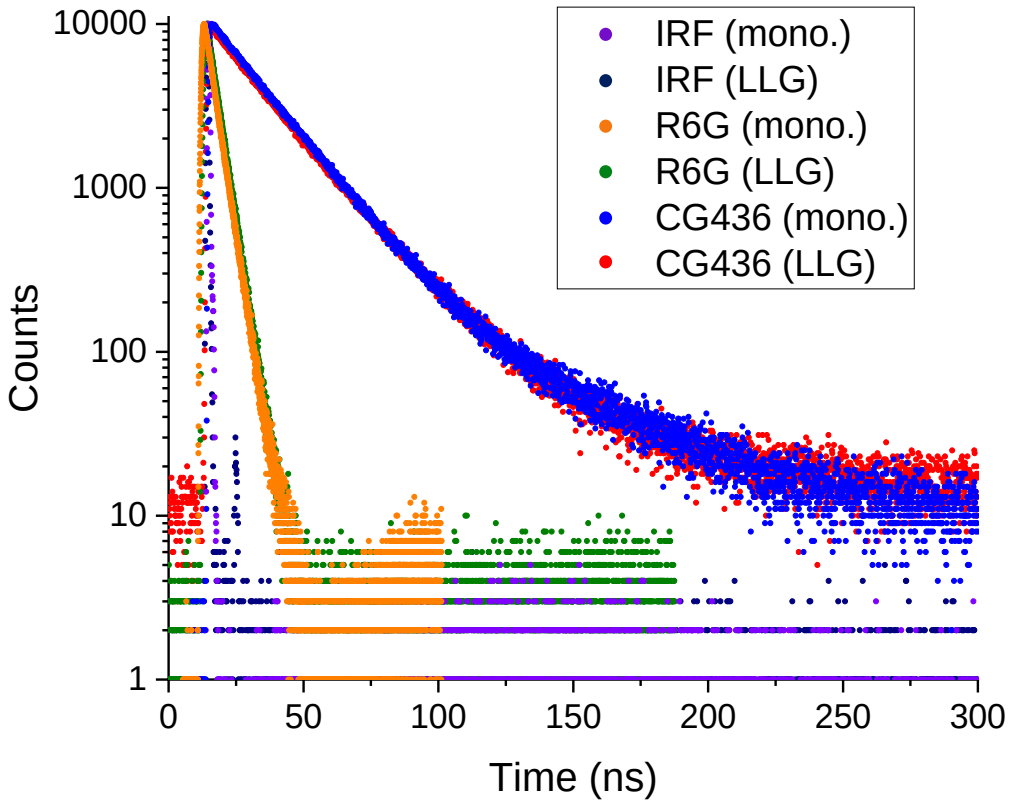

Figure 3.5: Comparison of the fluorescence decays obtained for Rhodamine 6G (R6G) and CG436 in water on the liquid light guide (LLG) and monochromator (mono.)-based systems. The decays of two fluorophores only have been shown here for clarity, where a comparison of those obtained for MeADOTA and JA120 can be found in Appendix A.

3.2.3 NADH in Solvent

NADH in Trizma buffer was also measured on the liquid light guide-based fluorescence lifetime system to further assess the suitability of the instrument for measuring the main fluorophore of interest. Measurements were conducted using a 339 nm NanoLED excitation source and a 450 nm emission wavelength. These measurements were for the purpose of assessing the suitability of measuring much shorter fluorescence decays, therefore the characteristics of NADH are not discussed here in detail and are instead investigated in Chapter 4.

3.2.3.1 Sample Preparation

The Trizma buffer was prepared prior to the addition of NADH, where 0.728 g of Tris HCl (Sigma Aldrich) and 0.047 g of Tris Base (Sigma Aldrich) were added to

100 mL water and mixed until fully dissolved to obtain a buffer solution of pH 7.0 at 25°C[124]. 1.13 mg of powdered reduced disodium salt hydrate of β-nicotinamide adenine dinucleotide (β-NADH, Sigma Aldrich) was dissolved in 20 mL of the Trizma buffer, where 1.5 mL of this NADH solution was added to a cuvette followed by another 1.5 mL of the Trizma buffer alone. The sample was then sealed with parafilm to be used for measurements, where samples were stored in the fridge at ~ 4°C when not in use.

3.2.3.2 Results & Discussion

Figure 3.6 shows the fluorescence decay obtained for NADH in Trizma on both the liquid light guide and monochromator-based fluorescence lifetime systems for comparison.

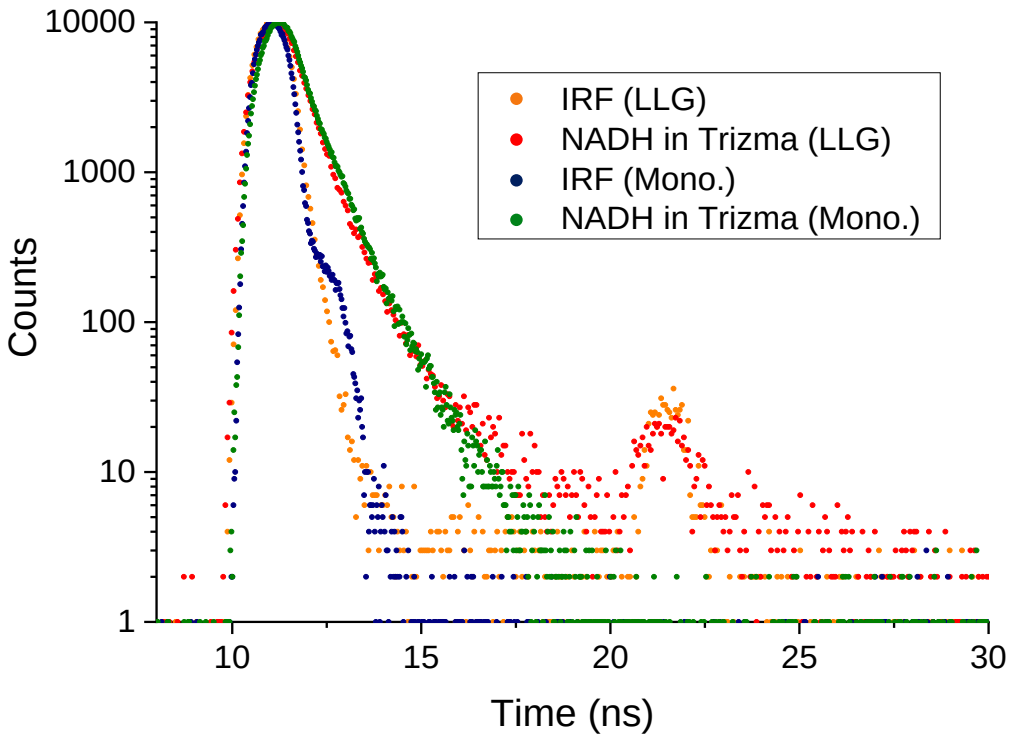

Figure 3.6: Fluorescence decay comparison of NADH in Trizma obtained on the liquid light guide-based (LLG) and monochromator-based (mono.) systems, where λ_{ex} = 339 nm and λ_{em} = 450 nm. A secondary peak due to reflections at the windows of the light guides is also seen for the measurements on the LLG system.

The fluorescence decays for NADH in Trizma on both systems are very similar; however at such a short timescale systematic effects are more prominent and therefore affect the fluorescence lifetime analysis. Figure 3.6 highlights a secondary peak in the data that occurs ~ 10.7 ns after the initial peak in both the IRF and fluorescence lifetime measurements. Late peaks after the instrumental pulse have previously been reported in linear focused photomultipliers[125,126], where backscattering of primary electrons at the first dynode at a delayed time has been suggested as a possible explanation for late peaks[126]. Another explanation is reflection occurring at the end of the liquid light guide. To test for this, the path length from the excitation source to the sample was doubled by coupling two liquid light guides together, giving a 2 m path length in total. Figure 3.7 shows the measurement of NADH in Trizma with the system in this configuration.

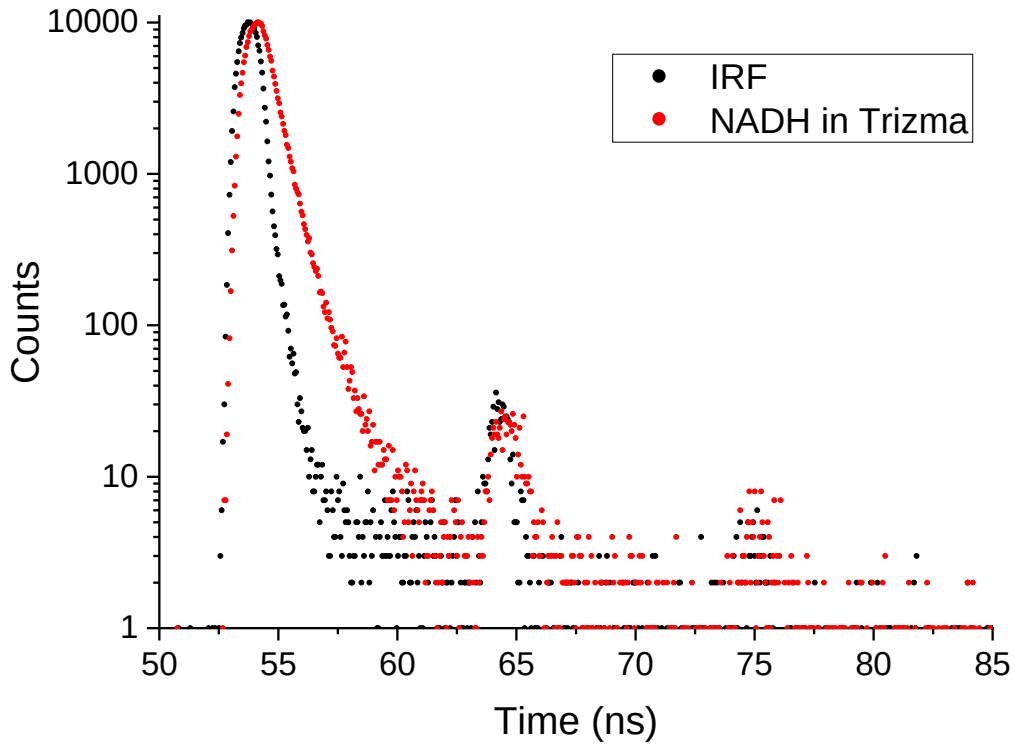

Figure 3.7: Fluorescence decay of NADH in Trizma with the LLG path length from the excitation source to the sample doubled, providing further confirmation that the additional peaks are due to reflections rather than backscattering of electrons in the PMT.

Figure 3.7 illustrates a third late peak occurring ~ 10.7 ns after the secondary peak, demonstrating that there must be reflection occurring at the interface of the liquid

light guides. Based on the time of 10.7 ns between the peaks and the additional 2 m distance the light travels, the speed of light within the fibre v is calculated to be ~ 1.87 x 10^8 ms^{-1}. Based on this speed, a refractive index n of the liquid core of the light guide can be calculated using:

$$n = \frac{c}{v} \tag{19}$$

where c is the speed of light in a vacuum. From Equation 19 the light guide was found to have a refractive index of ~ 1.60.

While the secondary peak is more prominent at such short timescales, the fluorescence decays obtained on the liquid light guide-based system could still be analysed relatively well as it is a weak feature. Its appearance was not of any immediate concern as NAD(P)H would most likely be measured in the cellular environment in future applications, where due to the increase in fluorescence lifetime under these circumstances the peak would have very little influence on the decay.

3.3 System Setup with Translational Stage

3.3.1 Instrument Design & Experimental Setup

To have the ability to move the sample incrementally in order to measure the fluorescence lifetime at different positions, a translational stage was purchased from ThorLabs (model number: PT1/M) to be incorporated into a new sample stage. A new holder for the liquid light guides was also designed and built so that these could be held at a fixed position and distance from the sample. A schematic as well as photographs of the setup are shown in Figures 3.8.

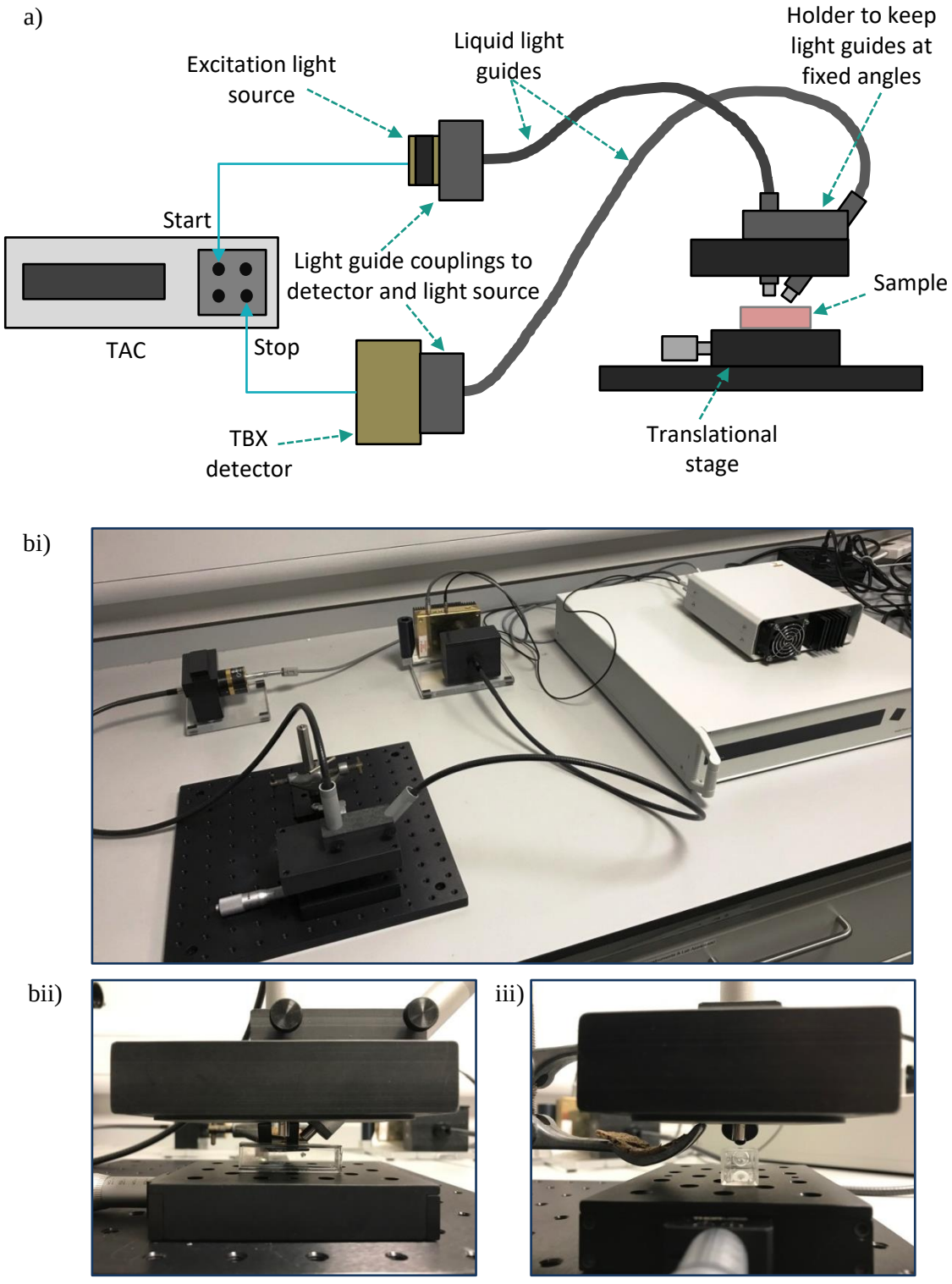

Figure 3.8: a) Schematic of the fluorescence lifetime system incorporating liquid light guides and a translational stage to place the sample where the same couplings for the light guides to the excitation source and detector were used as in the previous setup, and b) photographs of the i) full setup with the translational stage, with a more detailed view of the sample stage design in ii) and iii).

The schematic in Figure 3.8 a) shows that the liquid light guide carrying excitation light is perpendicular to the sample, where the liquid light guide carrying fluorescence to the detector is at 45° to minimise excitation light being collected by this light guide. This light guide was fixed at 45°, where the angle could not be adjusted. Longpass filters are still utilised in this setup, where the same couplings as the previous setup for the excitation source and detector to the light guides were used to further ensure only fluorescence is being collected by the detector. The photographs in Figure 3.8 b) show how the overall setup looked as well as a more detailed view of the sample stage. The sample stage could be moved left to right as viewed in Figure 3.8 b ii) in one plane over a 25 mm distance. The liquid light guide holder could be moved up and down as required using the clamp stand, and in addition to this, the position of the light guides themselves in the holders could be moved if necessary.

For fluorescence lifetime measurements using this setup, the surface interface of the liquid light guides were typically positioned at a height of 5 mm from the sample surface, which based on the cone angle could potentially illuminate ~ 10.2 mm of the sample surface from this height. Measurements were performed in a dark room, where a black cloth was also placed over the setup to further minimise unwanted photons being detected. Samples were measured in plastic cuvettes which were laid on their sides to provide a larger sample surface area, where the ability for measuring across a length of 25 mm was utilised in phantom tumour margin measurements in Chapter 5.

3.3.2 Conventional Fluorophore Measurements

In a similar way to Section 3.2.2, conventional fluorophores were first measured to assess the initial setup of the translational stage with the liquid light guides. Here, R6G and CG436 were measured using the same excitation and emission wavelengths as described in Section 3.2.

3.3.2.1 Sample Preparation

Samples of R6G and CG436 in water were prepared similarly to the previous measurements, where the stocks prepared in Section 3.2.2.1 were used again to produce 4.8 mL solutions of each dye in cuvettes with an absorbance of ~ 0.1. A volume of 4.8 mL brought the cuvettes to near maximum capacity, which ensured that no air bubbles would appear when the cuvette was laid on its side for measurement.

3.3.2.2 Results & Discussion

Figure 3.9 shows the fluorescence decays of R6G and CG436 measured using the translational stage setup in comparison to those obtained on the conventional monochromator-based fluorescence lifetime system, where a comparison of the lifetime components obtained are shown in Table 3.2.

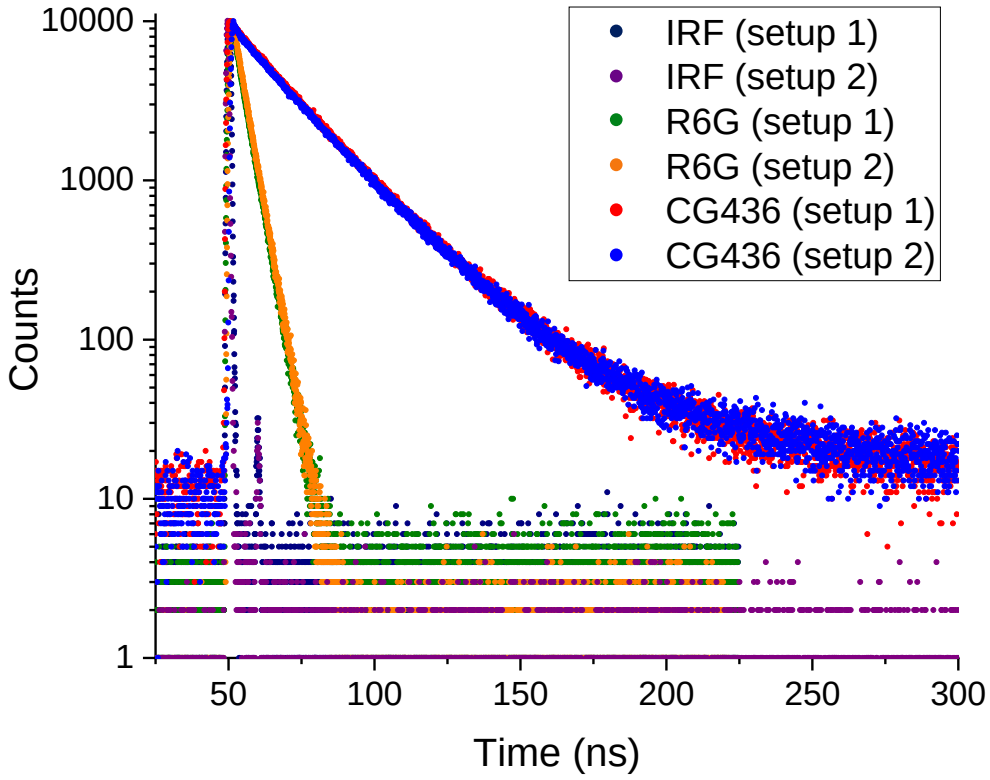

Figure 3.9: Comparison of the fluorescence decays of R6G and CG436 measured using the setup from Section 3.2 (setup 1) and the translational stage setup (setup 2), where the measurement parameters were the same as those used in Section 3.2.

Sample	λ_{ex} (nm)	λ_{em} (nm)	System	τ_1 (ns)	B_1 (%)	τ_2 (ns)	B_2 (%)	τ_{avg} (ns)	χ^2
CG436	339	440	Setup 1	17.1 ± 1.0	49.48	27.8 ± 0.5	50.52	21.2	1.11
			Setup 2	16.0 ± 1.0	46.49	27.9 ± 0.4	53.51	20.7	1.18
R6G	474	560	Setup 1	4.01 ± 0.02	100	-	-	4.01	1.10
			Setup 2	3.99 ± 0.01	100	-	-	3.99	1.03

Table 3.2: Fluorescence lifetime parameters obtained for the decay measurements shown in Figure 3.9 of R6G and CG436 on the original liquid light guide-based setup (setup 1) and the translational stage setup (setup 2), where good agreement in all parameters was observed between the two setups.

Both the fluorescence decays in Figure 3.9 and the corresponding lifetime values in Table 3.2 demonstrate that there were no immediate issues with the setup as they are in very close agreement with each other. Figure 3.9 also shows that the reflection peak is still apparent at the same position within this setup; however it again has no influence in this set of measurements. NADH in Trizma was also measured on the translational stage setup, where a comparison of this with the measurement on the first liquid light guide setup is shown in Figure 3.10. The fluorescence decays in Figure 3.10 show that the initial slopes are very similar in each setup, however from ~ 55 ns onwards the decay of NADH on the translational stage setup appears to be longer than that obtained on the original setup. It is possible this is due to fluorescence from the Trizma itself – while a new Trizma buffer was prepared for the translational stage measurements, the chemicals used were significantly older than what was used for the sample measured on the original liquid light guide setup. This Trizma buffer alone was measured using the same excitation source and fluorescence was collected at 450 nm for the same length of time as the NADH sample, where the sample was found to fluoresce under these conditions with a long decay component similar to what is seen in Figure 3.10.

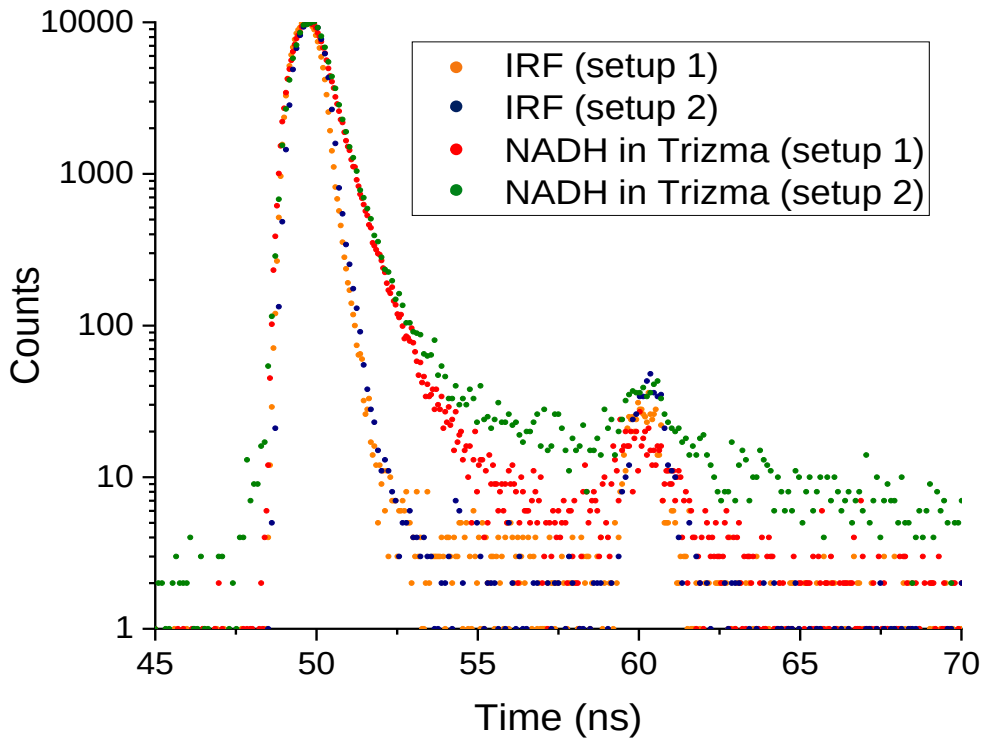

Figure 3.10: Comparison of the fluorescence decays of NADH in Trizma measured using the setup from Section 3.2 (setup 1) and the translational stage setup (setup 2), where λ_{ex} = 339 nm and λ_{em} = 450 nm. The longer decay of NADH in Trizma in setup 2 is most likely due to the Trizma buffer itself, as this was found to weakly fluoresce when measured alone under the same conditions.

3.4 Conclusions

Two variations of a liquid light guide-based fluorescence lifetime system have been designed and tested. Light guides were initially incorporated into an existing sample chamber, where measurements of conventional fluorophores demonstrated that this system produced fluorescence decays almost identical to that obtained on a conventional fluorescence lifetime system that incorporates monochromators. The second iteration of the light guide-based system incorporated a translational stage into the setup instead of a sample chamber, which allows the light guides to be moved to different positions above the sample. This system was also initially tested with conventional fluorophores, where again the results obtained were in excellent agreement with the first liquid light guide-based system as well as the conventional monochromator-based system.

Measurements of the shorter fluorescence decay of NADH on each system highlighted the appearance of reflected photons in the obtained decays. This could be due to photons being reflected at the window of the light guide coupled to the detector or at the window of the excitation light guide positioned at the sample, where they travel back down the light guide and back towards the detector/sample again. The probability of this occurring is low, where less than 100 photons were detected in the secondary peak. This could possibly be improved with better couplings to the detector or samples; however space between the light guide and the detector is required so that longpass filters can be added in order to select the emission wavelength. Space between the light guides and the sample would also be preferable so that the light guides can be moved across a sample easily. However, as discussed previously this should not cause issue when measuring the longer fluorescence lifetimes of NAD(P)H in the cellular environment, which would be the fluorophore of interest during surgery.

The results presented here demonstrate the capabilities of the liquid light guides for carrying excitation light and collecting fluorescence to produce accurate fluorescence lifetime measurements. This is essential for the translational stage setup in particular, where the ability to move the light guides across the sample is utilised in Chapter 5 for measurements of phantom margins to demonstrate its potential for calibrating a figure of merit for tumour margin applications.

4. Characterisation of NAD(P)H Fluorescence

4.1 Introduction

As previously discussed in Chapter 1, NADH and NADPH have very different roles in the body, yet they have very similar structures. A comparison of the chemical structures of NADH and NADPH is shown in Figure 4.1. Both structures consist of two nucleotides joined through phosphate groups, where NADPH contains an additional phosphate group attached to the ribose of adenosine, allowing it to interact with a different set of enzymes[127].

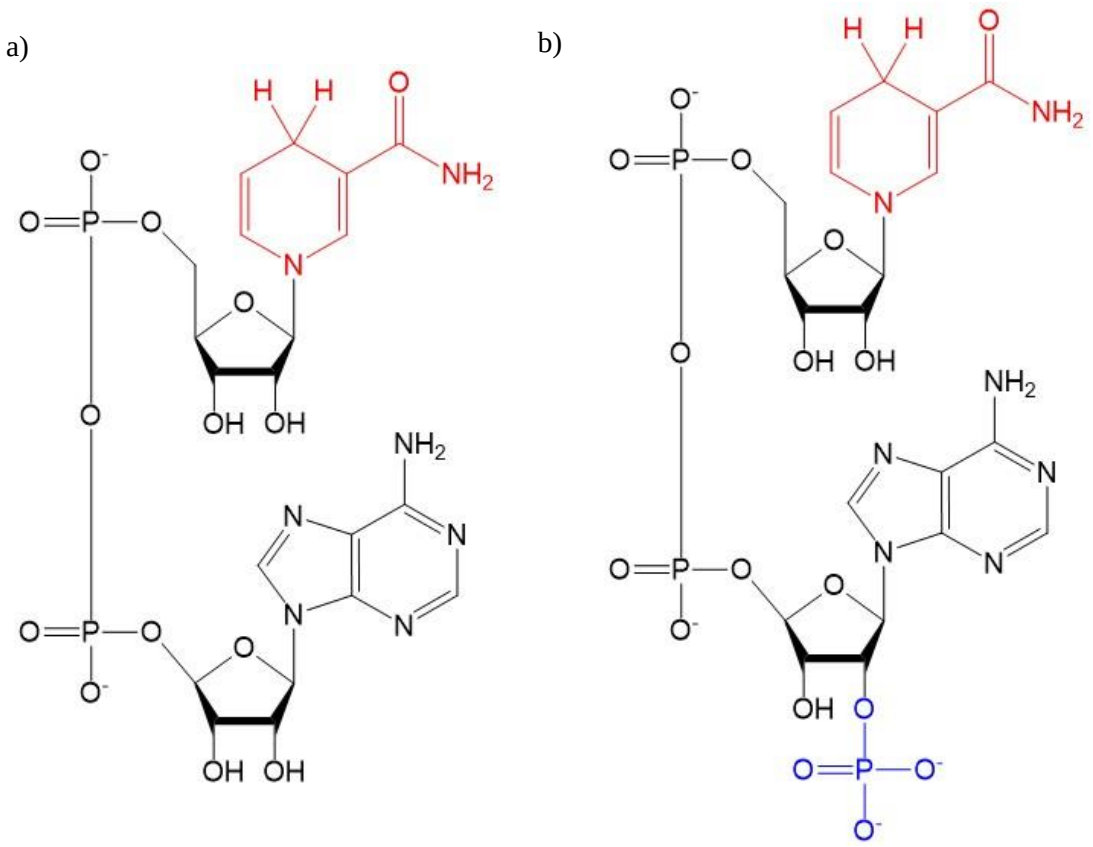

Figure 4.1: Chemical structure of a) NADH and b) NADPH, where the nicotinamide ring responsible for fluorescence is highlighted in red, and the additional phosphate group of NADPH is highlighted in blue.

The nicotinamide ring of NADH and NADPH is responsible for the fluorescence signal of interest in this work. NADH and NADPH have identical fluorescence properties despite the additional phosphate group of NADPH, since NADPH is phosphorylated at a remote site of the molecule far enough away from the

nicotinamide ring for it to remain unaffected. The absorption and fluorescence of NADH and NADPH are shown in Figure 4.2, where the almost perfect overlap of the spectra demonstrates these identical properties.

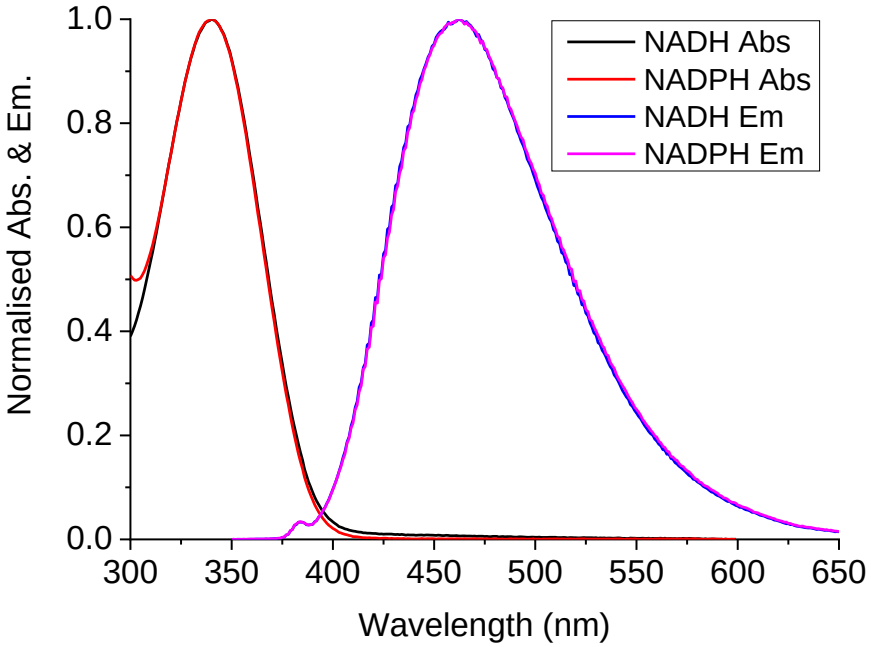

Figure 4.2: Normalised absorption and emission spectra of NADH and NADPH. Emission spectra were acquired using an excitation wavelength of 339 nm.

NAD(P)H has an absorption maximum at ~ 340 nm, where upon excitation at this wavelength the molecule will fluoresce with an emission peak of ~ 460 nm. There is an additional absorption peak at ~ 250 nm which is also present in $NAD(P)^+$, which is due to the adenine moiety[128]. The nicotinamide ring of $NAD(P)^+$ also absorbs, however its peak is blue-shifted from ~ 340 nm to ~ 220 nm. This is caused by a larger energy difference between the highest occupied molecular orbital and the lowest unoccupied molecular orbital in $NAD(P)^+$ than that of the molecule in its reduced form, resulting in more energy being required to excite the oxidised form[128]. While NAD(P)H absorbs at ~ 340 nm and has an emission peak of ~ 460 nm, $NAD(P)^+$ does not absorb or fluoresce significantly at these wavelengths[129].

The fluorescence lifetime of NAD(P)H has been widely studied. Early measurements of the fluorescence lifetime of NADH characterised the lifetime as ~ 0.4 ns at room temperature using a single exponential model[130,131]. Later studies utilising excitation via a UV-mode locked Argon ion laser revealed that a 2-exponential model best

described the fluorescence lifetime properties of NADH, where values of 0.25 ns and 0.69 ns in water were reported[132]. One of the most popular explanations for the 2-exponential decay is due to NADH existing in both a folded and open forms which in turn affects the interactions between the nicotinamide and adenine rings, where it is believed the longer lifetime component corresponds to NADH in a folded configuration and the shorter lifetime corresponding to NADH in its open form[132,133]. It has recently been suggested however that these two lifetimes instead correspond to structural differences in the nicotinamide ring in particular in each subpopulation of molecules[134]. The fluorescence lifetime of NAD(P)H has also been found to increase when bound to proteins, as well as the value being dependent on which protein it is bound to[75]. These interesting properties have led to various studies of NAD(P)H in the cellular environment, which have utilised its fluorescence for applications such as defining brain and lung tumour margins[35,135], assessing the REDOX state of cells[136] as well as discriminating between normal and pre-cancerous epithelia by observing the protein-bound fluorescence lifetime of NADH[137].

This chapter looks to document both the spectral and fluorescence lifetime properties of NAD(P)H in various solvents more thoroughly, where several environmental factors were investigated. These factors included viscosity, pH, temperature and oxygen level, all of which may prove useful to have a more complete understanding of initially before moving on to look at the properties of NAD(P)H in the more complex environments such as silica sol-gels and the cellular environment in later work.

4.2 Experimental Setup

Absorption measurements were obtained using a PerkinElmer Lambda 2 UV/Vis spectrometer, where samples were measured over a 300 nm – 700 nm window at a scan speed of 480 nm/min using a slit width of 1 nm. Measurements of the fluorescence emission were collected on a HORIBA FluoroMax-2 spectrometer, where samples were excited at 339 nm, and emission was obtained from 350 nm – 700 nm. Both slit widths were set to a 3 nm resolution for emission measurements

and samples were scanned in 1 nm increments, where the emission was collected for 0.5 s at each increment. The ratio of the corrected signals accounting for the excitation and emission wavelength correction factors and dark counts (*Sc/Rc*) was used to produce the final emission spectra shown.

Fluorescence lifetime measurements were acquired using a HORIBA DeltaFlex system using the TCSPC technique described previously, where samples were excited using a 339 nm NanoLED and emission wavelengths were selected using a monochromator with a 16 nm slit resolution. A TAC range of 100 ns was used for all measurements. Data analysis to determine the fluorescence lifetimes and corresponding parameters for all measurements was performed using the DAS6 package using NLLS reconvolution analysis as previously described.

4.3 NADH Fluorescence in Simple Solvents

Before looking into the fluorescence properties of NAD(P)H in the more complex sol-gel and cellular environments, NADH was first studied in various solvents to better understand its fluorescence properties in these simpler environments.

4.3.1 Sample Preparation

All chemicals were purchased from Sigma Aldrich. To prepare the NADH samples for measurements, 5.68 mg of powdered β-NADH was dissolved in 200 ml of various solvents, which included water, ethylene glycol, phosphate-buffered saline (PBS), and Tris(hydroxymethyl)aminomethane (Trizma) to obtain solutions of NADH at 40 μM concentrations. The solvents PBS and Trizma were prepared prior to the addition of NADH. PBS was prepared by dissolving one PBS tablet in 200 ml of water and stirred for 5 minutes to obtain a solution of pH 7.4 at 25 °C. Trizma was prepared as described previously in Section 3.2.3.1. Once the NADH had dissolved in the solvents, 3 mL of each sample was added to plastic cuvettes and sealed with parafilm to be used in measurements. Samples were stored in the fridge at ~ 4 °C and β-NADH was stored at ~ - 20 °C in the freezer when not in use.

4.3.2 Results & Discussion

Absorption measurements of NADH in the different solvents were initially performed, where the differences in absorbance spectra are shown in Figure 4.3.

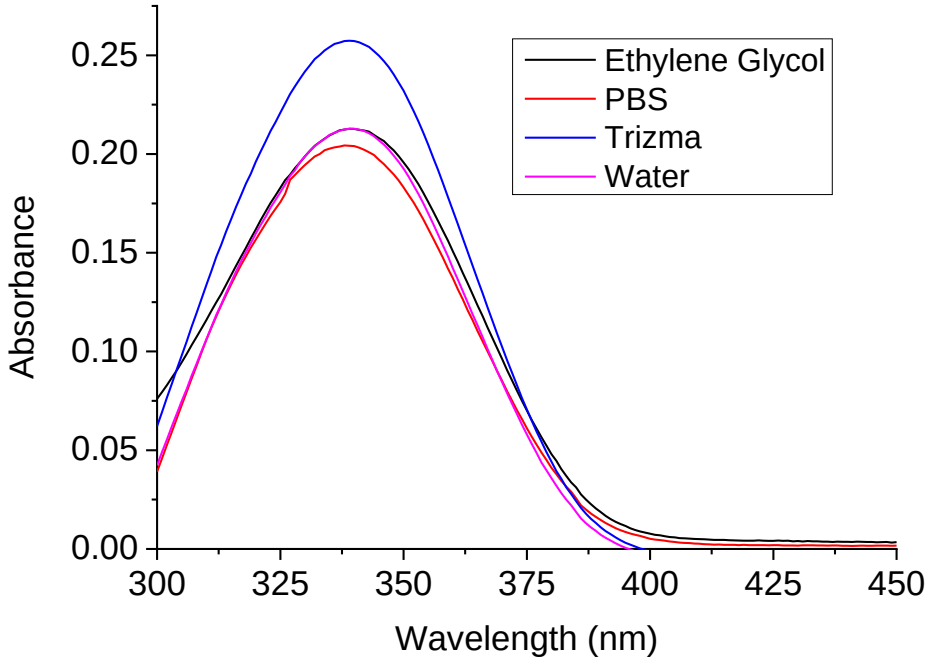

Figure 4.3: Absorbance spectra of NADH in ethylene glycol, PBS, Trizma and water at a 40 µM concentration, where the highest absorbance of NADH was observed in Trizma.

The spectra in Figure 4.3 reveal a solvent dependency on the absorption properties of NADH, where there is a higher absorbance in Trizma compared to the other solvents. The peak wavelength of absorption was 338 nm for NADH in PBS and 339 nm in the other solvents, therefore samples were excited at 339 nm to obtain the emission spectra shown in Figure 4.4. These emission spectra give a better indication of the solvent effects occurring. The emission intensity of NADH was highest in ethylene glycol, which had the highest viscosity out of the solvents used in the measurements. A higher viscosity will often increase the quantum yield of a fluorophore by reducing dissipative pathways due to the reduction in the number of collisional interactions between the fluorophore and solvent molecules as well as increased structural rigidity, therefore slowing down the deactivation process of fluorescence[138].

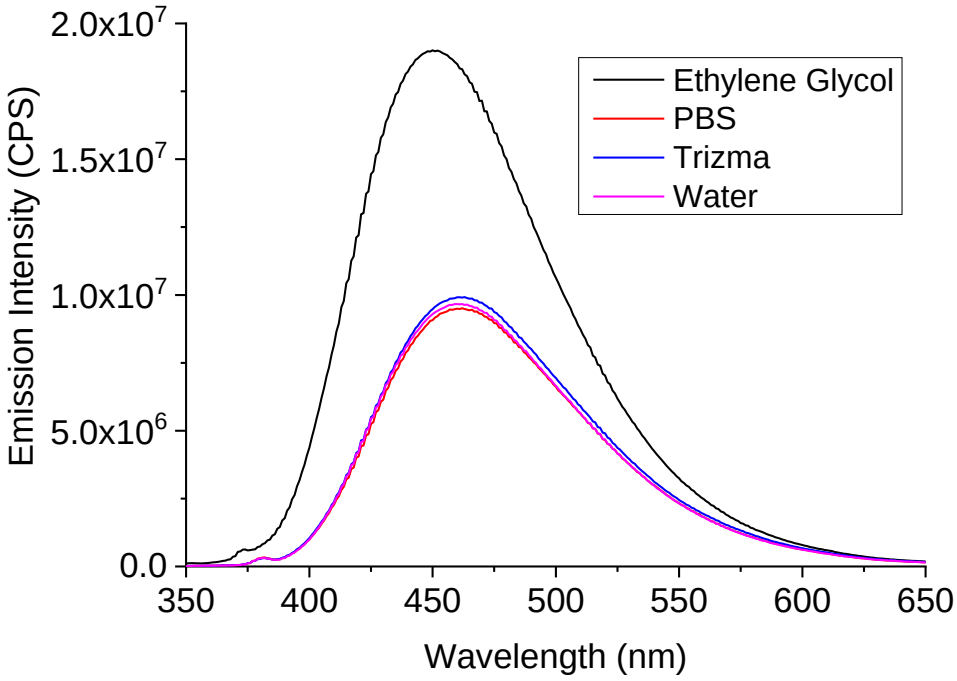

Figure 4.4: Emission spectra obtained for NADH in the same solvents at a 40 µM concentration, where samples were excited at 339 nm and emission collected over a 350 nm – 650 nm range. An increase in emission intensity and blue-shift in peak wavelength position is observed for NADH in ethylene glycol, which is due to its increased viscosity and lower polarity respectively compared to the other solvents.

Figure 4.4 also highlights a slight redshift in the peak emission of NADH in the other solvents (λ_{max} = ~ 460 nm) compared to NADH in ethylene glycol (λ_{max} = 450 nm), which is most likely due to the difference in the solvent polarities. After excitation, the solvent molecules reorient themselves around the fluorophore in terms of their dipole moments in order to lower the energy of the excited state. The increase in solvent polarity of Trizma, PBS and water compared to ethylene glycol increases this effect, causing a greater reduction in energy of the excited state and therefore resulting in emission of a photon at an even longer wavelength[75].

The fluorescence decay of NADH in each solvent was also measured, where typical decays obtained in each solvent are shown in Figure 4.5. Each sample was also measured at emission wavelengths ranging from 420 – 480 nm to assess if there was any change in the lifetime properties of NADH at these different wavelengths; however no significant differences were seen in the lifetime values obtained in any of the solvents.

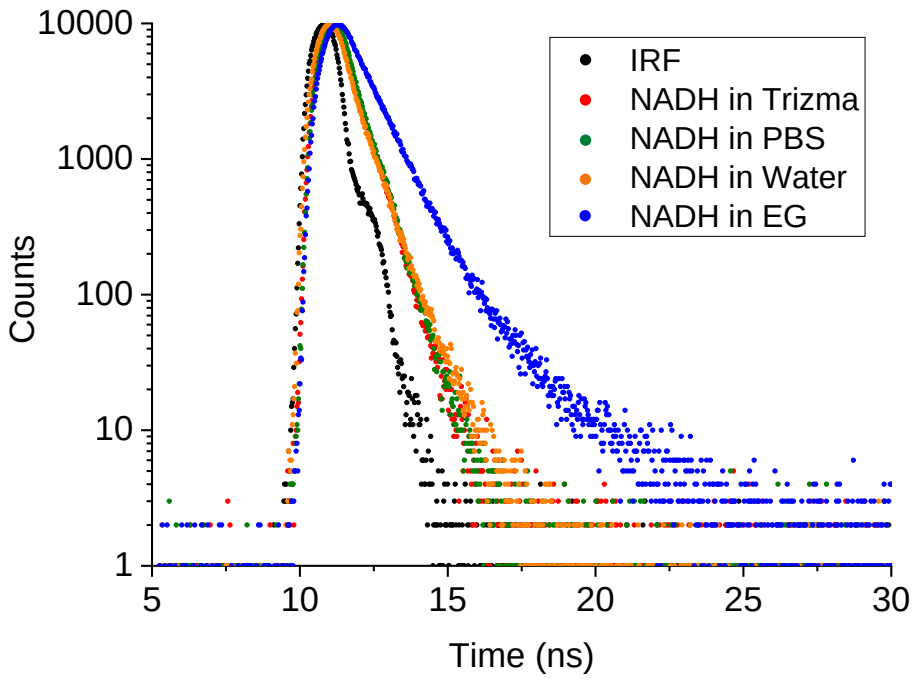

Figure 4.5: Fluorescence decay of NADH in each solvent (where EG = ethylene glycol) at a 40 µM concentration, where λ_{ex} = 339 nm and λ_{em} = 460 nm. The increased viscosity of EG again has the greatest influence on the decay, where the obtained lifetime parameters were almost double that observed in the other solvents.

The fluorescence decay of NADH was best fit to a 2-exponential decay in all cases. Figure 4.5 shows the difference in the fluorescence decays obtained in each of the solvents, where again the most significant difference is seen in ethylene glycol compared to the other solvents. The fluorescence decay of NADH in ethylene glycol is considerably longer than that seen in Trizma, PBS and water. The differences can be seen in greater detail in Table 4.1, showing the individual lifetime components determined for NADH in each solvent. As the viscosity has already been shown to affect the fluorescence of NADH, the results in Table 4.1 demonstrate how it may also be contributing to the difference in lifetime parameters found for NADH in ethylene glycol compared to the other solvents. Both τ_1 and τ_2 for NADH in ethylene glycol are approximately double the values found in other solvents, and there is also an increase in contribution of τ_1 observed for NADH in ethylene glycol. Since collisional interactions and therefore dissipative pathways are reduced, the time spent in the excited state is prolonged therefore giving a longer fluorescence lifetime[139]. This is reflected in the results shown in both Figure 4.5 and Table 4.1 and is also consistent with what is observed in Figure 4.4.

Solvent	τ_1 (ns)	B_1 (%)	α_1	τ_2 (ns)	B_2 (%)	α_2	τ_{avg} (ns)	χ^2
Trizma	0.31 ± 0.03	79.68	0.90	0.68 ± 0.03	20.32	0.10	0.35	0.94
PBS	0.32 ± 0.03	76.86	0.88	0.68 ± 0.03	23.14	0.12	0.36	1.04
Water	0.34 ± 0.03	74.64	0.88	0.82 ± 0.03	25.36	0.12	0.40	1.01
EG	0.68 ± 0.02	81.98	0.92	1.64 ± 0.05	18.02	0.08	0.76	1.11

Table 4.1: Fluorescence lifetime parameters, percentage contributions and normalised pre-exponentials obtained for NADH in each of the solvents at a 40 µM concentration as shown in Figure 4.5, along with the associated goodness of fit for measurements using λ_{ex} = 339 nm and λ_{em} = 460 nm.

4.4 Environmental Effects on NADH Fluorescence Lifetime

Various environmental factors that are worth considering when studying the fluorescence properties of NAD(P)H in more complex environments have also been investigated in the simple solvent environment to see what kind of influence they may have on the properties of NAD(P)H. Such environmental factors that have been investigated include temperature, pH and oxygen levels.

4.4.1 Temperature Effects

As all measurements had been previously made at room temperature, the effect on the fluorescence lifetime of NAD(P)H at 37 °C was then investigated to mimic body temperature, as this is how NAD(P)H would be measured in the surgical environment.

4.4.1.1 Sample Preparation

Samples of NADH were prepared as previously described in Section 4.3.1, where in this case smaller volumes were instead prepared by dissolving 0.85 mg of β-NADH in 30 mL of each solvent to obtain samples of 40 µM concentrations. Fluorescence

lifetime measurements of each sample were made at room temperature (~ 20 °C) and body temperature (37 °C), where the higher temperature was achieved by attaching a Cole-Palmer Polystat digital heated recirculator to the sample holder in the fluorescence lifetime system. Samples were placed in the holder for ~ 10 minutes to ensure they had reached the desired temperature.

4.4.1.2 Results & Discussion

The fluorescence decays of NADH measured in each solvent at both room and body temperature are shown in Figure 4.6.

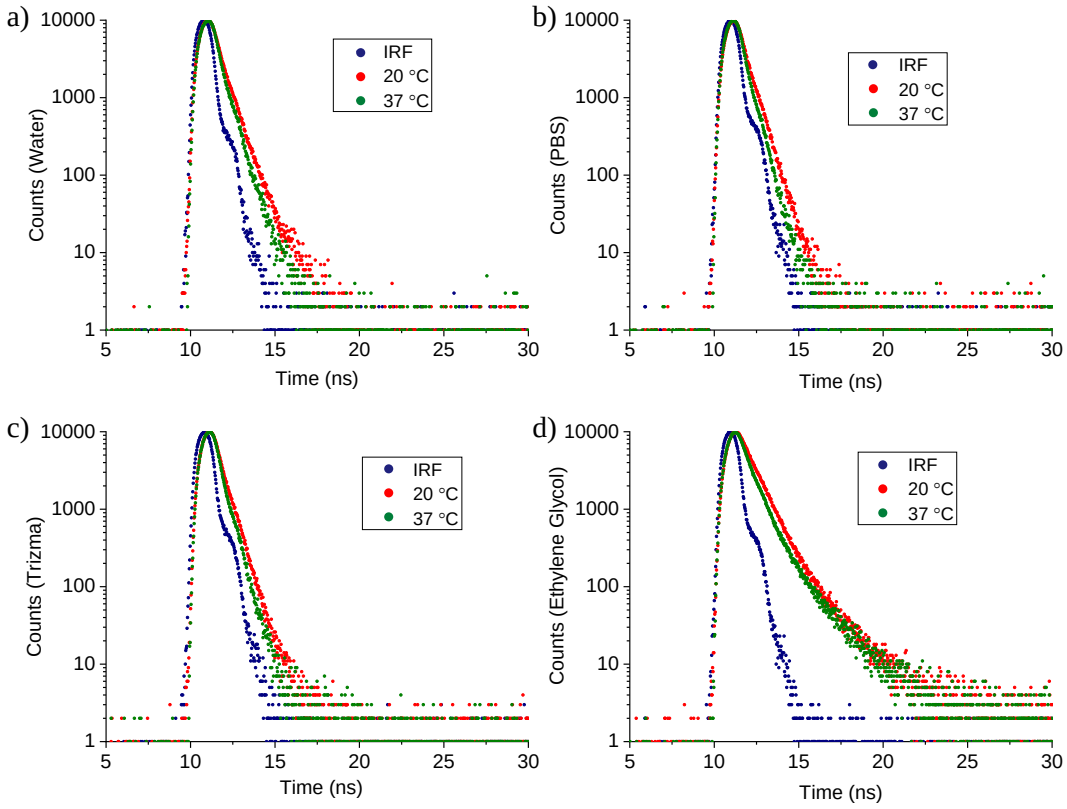

Figure 4.6: Fluorescence decay of NADH at a 40 µM concentration in a) water, b) PBS, c) Trizma and d) ethylene glycol at both room and body temperature (37 °C), where λ_{ex} = 339 nm and λ_{em} = 460 nm. An increase in temperature caused a decrease in the fluorescence decay in all solvents.

A visible shortening of the fluorescence decay of NADH is observed in every solvent upon increase of temperature. A comparison of the individual lifetime components found for each measurement is shown in Table 4.2.

Solvent	Temp. (°C)	τ_1 (ns)	B_1 (%)	α_1	τ_2 (ns)	B_2 (%)	α_2	τ_{avg} (ns)	χ^2
Trizma	20	0.31 ± 0.03	79.68	0.90	0.68 ± 0.03	20.32	0.10	0.35	0.94
	37	0.26 ± 0.04	82.71	0.91	0.57 ± 0.04	17.29	0.09	0.29	1.11
PBS	20	0.32 ± 0.03	76.86	0.88	0.68 ± 0.03	23.14	0.12	0.36	1.04
	37	0.20 ± 0.09	58.64	0.75	0.43 ± 0.02	41.36	0.25	0.26	1.05
Water	20	0.34 ± 0.03	74.64	0.88	0.82 ± 0.03	25.36	0.12	0.40	1.01
	37	0.27 ± 0.03	81.92	0.92	0.67 ± 0.04	18.08	0.08	0.30	1.14
EG	20	0.68 ± 0.02	81.98	0.92	1.64 ± 0.05	18.02	0.08	0.76	1.11
	37	0.52 ± 0.02	79.40	0.92	1.52 ± 0.04	20.60	0.08	0.60	1.09

Table 4.2: Corresponding fluorescence lifetime parameters for the measurements of NADH at room and body temperature shown in Figure 4.6, where a decrease in the value of every lifetime component is observed due to the increase in collisional interactions at the higher temperature.

The parameters obtained in Table 4.2 show that both τ_1 and τ_2 decrease in value as the temperature is increased, and that no significant trends were observed in the change in the normalised pre-exponentials or contributions of either component. A decrease in fluorescence lifetime is to be expected. A higher temperature will reduce the viscosity of the solvents, increasing dissipative pathways due to the increase in collisional interactions between the fluorophore and solvent molecules, which will in turn reduce the fluorescence lifetime. This could suggest that if fluorescence lifetime measurements of NAD(P)H were conducted within the body, the parameters obtained may be slightly shorter than what would be measured in vitro.

4.4.2 pH Effects

Cancer cells are reported to typically have a higher intracellular pH of ~ 7.2 – 7.7 compared to a pH of ~ 7.0 – 7.2 in healthy cells[140]. Conversely, a lower extracellular pH of ~ 6.2 – 6.9 was also reported for cancer cells, compared to an extracellular pH of ~ 7.3 – 7.4 in healthy cells[140]. In order to assess the effect of pH on the properties of NAD(P)H, measurements of NADH were taken in water over a broad range of pHs.

4.4.2.1 Sample Preparation

30 mL solutions of water were initially prepared at pHs of approximately 3, 5, 7, 9 and 11. To reduce the pH of the water hydrochloric acid was added, whereas sodium hydroxide was added to increase the pH. Only a few drops were added at a time in order to make only minor adjustments. Once the solutions were at appropriate pHs, 0.85 mg of the powdered β-NADH was added to obtain samples at a 40 μM concentration, where 3 mL of each sample was added to a cuvette and sealed with parafilm for use in measurements.

4.4.2.2 Results & Discussion

Figure 4.7 shows the lifetime components obtained over the pH range of ~ 3 – 11 and the normalised pre-exponentials of each component respectively, where the normalised pre-exponentials provide information on the relative concentrations of each emitting species.

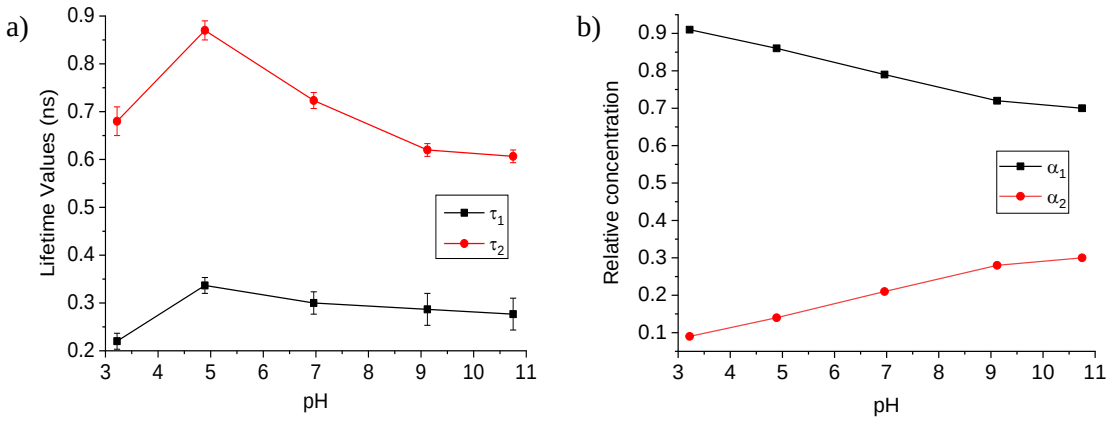

Figure 4.7: a) Fluorescence lifetime components τ_1 and τ_2 for the fluorescence decays of NADH measured at a 40 µM concentration over a pH range of ~ 3 – 11, along with b) the corresponding normalised pre-exponential factors giving an indication of the relative concentration of each component present in the sample.

An increase in value of both lifetime components is observed from pH 3 to pH 5 in Figure 4.7 a), which then starts to gradually decrease from pH 5 to pH 11. In addition to this, there is a steady decrease in the relative concentration of τ_1, which drops from 0.91 to 0.7 over this pH range. These results indicate that the fluorescence lifetime properties of NADH are somewhat influenced by the pH of its immediate environment both in terms of the lifetime values and relative concentrations of each species of NADH present, but they are not affected to a great extent. The values obtained at ~ pH 7 resemble those seen in previous measurements of NADH in the solvents similar to water. It would be expected that NADH would be most stable around this pH as the product guidelines suggest storage at ~ pH 8, where acidic solvents are prone to decomposing NADH[141] which may explain the larger differences observed in the lifetime values at the lower pHs. However, as there is not a large change seen overall across a pH range of ~ 3 – 11, it is unlikely there would be significant changes observed in the fluorescence lifetime over the smaller intra/extracellular pH ranges of healthy and cancerous cells that could be attributed to pH alone.

4.4.3 Oxygen Effects

The effect of oxygen on the fluorescence lifetime of NADH has also been investigated. Depleted oxygen is a common trait in many malignant tumours[142], therefore a difference in fluorescence lifetime of NAD(P)H between the two environments with and without oxygen could provide a potential method for determining between healthy and cancerous cells.

4.4.3.1 Sample Preparation

Samples of NADH in the various solvents at a 40 μM concentration were prepared in the same way as described in Section 4.4.1.1. 3 mL of each sample was added to a cuvette, which was sealed with a rubber stopper and further secured with parafilm. To remove oxygen from the samples, argon gas was bubbled through the solutions for ~ 5 minutes per sample using BD Microlance 3 needles, where the samples were then resealed with more parafilm afterwards. Fluorescence lifetime measurements were conducted immediately after each sample had been resealed.

4.4.3.2 Results & Discussion

The fluorescence lifetime of NADH was measured before and after oxygen removal in the four solvents used previously. Figure 4.8 shows the fluorescence decays obtained for NADH in ethylene glycol and water, where the biggest visual differences in the decays were observed.

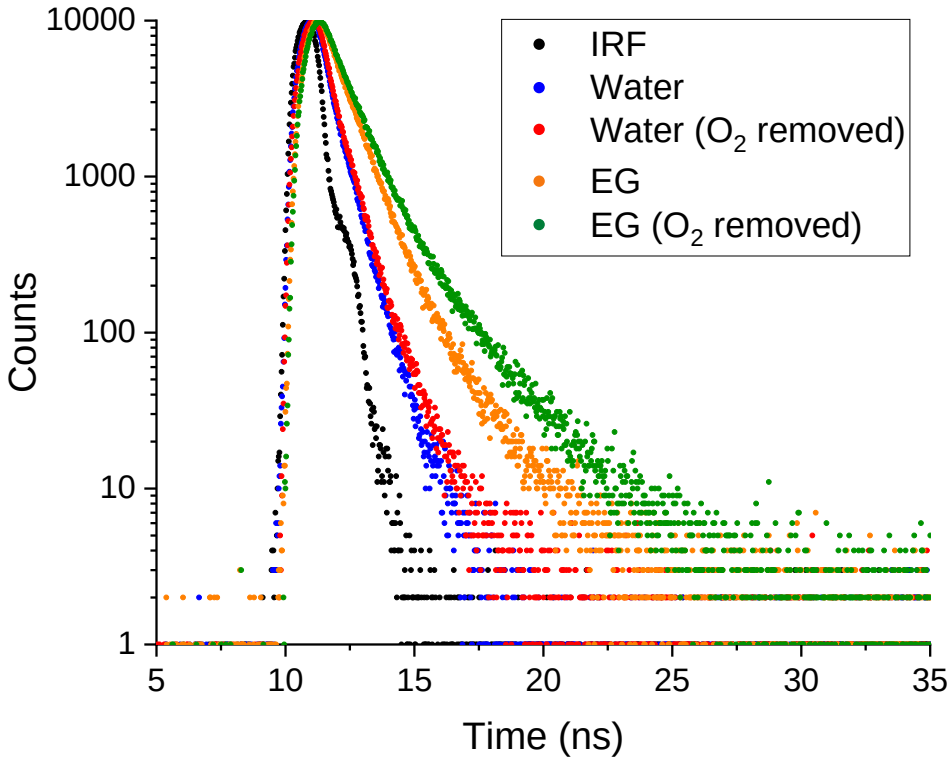

Figure 4.8: Fluorescence decays of NADH in water and ethylene glycol (EG) at a 40 µM concentration, measured before and after oxygen was removed from the samples. The difference in decays was not as significant for NADH in Trizma and PBS, however these decays can be found in Appendix B for comparison.

Table 4.3 shows the results obtained in each solvent in more detail, showing a comparison of the fluorescence lifetime components obtained in each case. The fluorescence decays in Figure 4.8 as well as the corresponding fluorescence lifetime parameters for NADH in water and ethylene glycol in Table 4.3 show that the removal of oxygen from the sample had the greatest effect in these solvents. In both solvents a visible increase of the fluorescence decays can be seen, where the value of both lifetime components of NADH increase in both cases after oxygen has been removed, however the increase in the lifetime components of < 1 ns may depend on the analysis using a 2-exponential model and therefore not be as reliable. In comparison to this, we see very little change in the lifetime components of NADH in Trizma and PBS, however a rise in the average lifetime of NADH in Trizma is observed due to the increased contribution from the larger lifetime component. Oxygen is known to be an extremely efficient quencher, and so a change in both the fluorescence decays and lifetime parameters is expected.

Solvent	τ_1 (ns)	B_1 (%)	α_1	τ_2 (ns)	B_2 (%)	α_2	τ_{avg} (ns)	χ^2
Trizma	0.31 ± 0.03	79.68	0.90	0.68 ± 0.03	20.32	0.10	0.35	0.94
after O_2 removal	*0.33 ± 0.04*	*69.91*	*0.84*	*0.74 ± 0.03*	*30.09*	*0.16*	*0.40*	*1.15*
PBS	0.32 ± 0.03	76.86	0.88	0.68 ± 0.03	23.14	0.12	0.36	1.04
after O_2 removal	*0.27 ± 0.05*	*51.52*	*0.71*	*0.61 ± 0.02*	*48.48*	*0.29*	*0.37*	*1.05*
Water	0.34 ± 0.03	74.64	0.88	0.82 ± 0.03	25.36	0.12	0.40	1.01
after O_2 removal	*0.38 ± 0.02*	*74.66*	*0.88*	*0.96 ± 0.02*	*25.34*	*0.12*	*0.45*	*1.06*
EG	0.68 ± 0.02	81.98	0.92	1.64 ± 0.05	18.02	0.08	0.76	1.11
after O_2 removal	*0.81 ± 0.02*	*77.71*	*0.90*	*2.17 ± 0.04*	*22.29*	*0.10*	*0.94*	*1.08*

Table 4.3: Fluorescence lifetime parameters determined for NADH in each solvent before and after oxygen removal. A 2-exponential fit was most suitable for this data, as a 1-exponential fit indicated that at least one additional component was required, and a 3-exponential fit did not improve the χ^2 value.

The bigger change in the lifetime of NADH in ethylene glycol compared to the other samples could be due to the difference in viscosities of the solvents. While oxygen diffusing back into the sample after the Argon gas had been used to remove it was prevented as much as possible, there is still a possibility that oxygen was able to leak back into the samples. For the samples of lower viscosity such as NADH in water – which yields a larger diffusion coefficient than NADH in ethylene glycol based on the Stokes-Einstein relation for molecules diffusing in liquids[143] – oxygen would be able to diffuse back into the solvent quicker, meaning a smaller difference in the fluorescence lifetime would be observed by the time the sample was measured.

4.4.4 Fluorescence Anisotropy Measurements

Anisotropy measurements of NADH in the simple solvent environment were also conducted. As two different species of NADH are known to exist when free in solution, anisotropy measurements were undertaken to determine if any difference in the rotational dynamics of each species could be observed.

4.4.4.1 Sample Preparation

Samples of NADH in ethylene glycol at a 40 μM concentration were prepared in the same way as described in 4.4.1.1, where 3 mL was added to a cuvette and sealed with parafilm for measurement. Ethylene glycol was chosen as the solvent for these measurements due to its higher viscosity, as this would slow down the rotation of smaller conformations.

4.4.4.2 Results & Discussion

The sum and difference data acquired for NADH in ethylene glycol and subsequently used for analysis are shown in Figure 4.9 a), where the resulting anisotropy is shown in Figure 4.9 b).

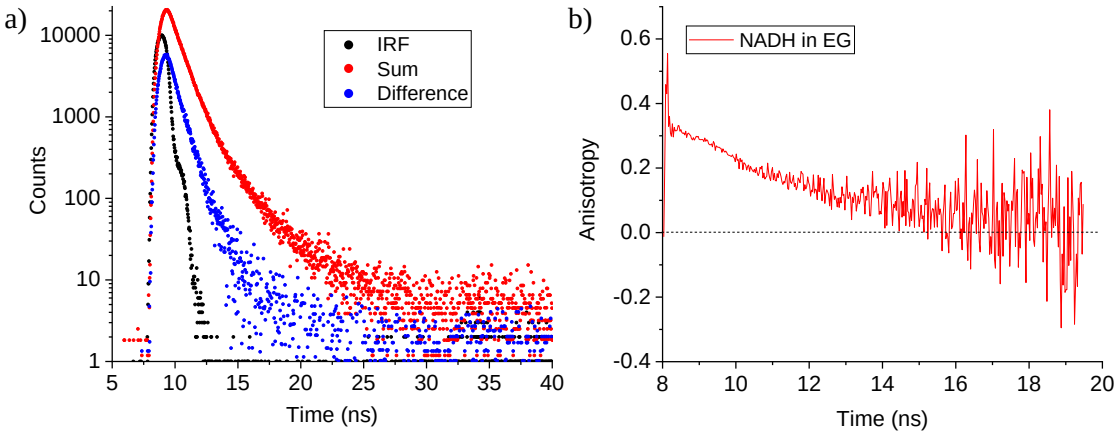

Figure 4.9: a) The sum and difference data acquired from the measurement of NADH in ethylene glycol, and b) the resulting anisotropy decay. The difference data was used to obtain the rotational correlation times as this provides more reliable results than a direct analysis of the residual anisotropy decay.

The results of the analysis of the sum and difference data used in this instance to determine the rotational correlation times of NADH in ethylene glycol are shown in Table 4.4.

	τ_{f1} (ns)	B_1 (%)	α_1	τ_{f2} (ns)	B_2 (%)	α_2	τ_{avg} (ns)	χ^2
Sum	0.77 ± 0.02	81.00	0.92	2.04 ± 0.05	19.00	0.08	0.87	1.27
	τ_{r1} (ns)			τ_{r2} (ns)				
Difference	0.43 ± 0.24	4.43	0.37	5.49 ± 0.04	95.57	0.63	0.94	1.07

Table 4.4: Results from the analysis of the sum and difference data of NADH in ethylene glycol, where τ_{f1} and τ_{f2} correspond to the fluorescence lifetimes of species present in the sample, and τ_{r1} and τ_{r2} are the rotational correlation times of the species. Two rotational correlation times indicates there are two different sized species present.

A 2-exponential fit was adequate to describe the sum data acquired. The values found for τ_{f1} and τ_{f2} are close to that observed for previous measurements of NADH in ethylene glycol in Section 4.3.2, however both values are slightly higher. This could be due to the higher number of counts used in the sum fit, where there were ~ 20,000 counts in the peak compared to the typical value of 10,000. The difference data also required 2-exponentials to adequately describe the decay, indicating two differently sized species within the sample. The associated correlation times could be due to the folded and unfolded conformations of NADH present, where the folded conformation would likely be represented by the shorter rotational time of 0.43 ns and the unfolded conformation by the longer time of 5.49 ns. Rough calculations of the size of each species can be determined using Equation 17 from Chapter 2, where sizes of ~ 0.6 nm and ~ 1.4 nm have been calculated from the rotational times of 0.43 ns and 5.49 ns respectively. A large difference in size such as that found here between the two species seems more likely to be due to folded and unfolded conformations of NADH rather than the different conformations of the nicotinamide ring in NADH where the amide group is rotated as discussed in the work by Blacker

et. al.[134], as it seems that the rotation of this group would be unlikely to cause as large a difference in rotational times.

4.5 Conclusions

The fluorescence properties of NADH have been studied under various conditions. The results in Section 4.3 highlighted that NADH is an environmentally sensitive fluorophore. Solvent properties such as its polarity and viscosity were found to influence the emission and fluorescence lifetime of NADH, where the more polar solvents caused a redshift in the peak emission wavelength and the more viscous solvent increased both the emission intensity and the fluorescence lifetime.

Various environmental factors with relevance to cancer cell studies were investigated in Section 4.4. Factors such as pH, temperature and oxygen levels have been studied, where the pH was found to have the least influence in these measurements. Increasing the samples to body temperature caused a decrease in the fluorescence decay, where removal of oxygen caused a significant increase in the fluorescence decay in two of the solvents. As samples were only subject to oxygen removal for ~ 5 minutes, future studies where this time is increased may be beneficial to see how the fluorescence lifetime of NADH is affected after prolonged deprivation of oxygen, as this is a more accurate representation of the tumour environment. Fluorescence anisotropy measurements of NADH in solution were also conducted, where two rotational correlation times were obtained. This is thought to be most likely due to the folded and unfolded conformations of NADH that would be present in the sample, as the reasonably large difference in size of ~ 0.8 nm between the two species would indicate this. Results indicating the presence of folded and unfolded NADH from such anisotropy measurements of NADH free in solution have not been previously reported in the literature, demonstrating the ability of this technique to potentially discriminate between the two conformations. The results presented in this section demonstrate how various environmental factors can influence the fluorescence properties of NADH and should be taken into consideration when moving forward with measurements of NAD(P)H in more complex environments.

5. Silica Sol-Gels as Human Tissue Phantoms

5.1 Introduction

Tissue-mimicking phantoms are materials that can mimic the optical properties such as the absorbance and scattering of tissue, as well as reflect the geometries of different tissues as required. Phantoms are often required for quality control and validation of system performance and use, where purposes can include use in optimising and testing system designs, comparing the performance of different systems as well as for calibration and testing stability and reproducibility of instruments[144]. The characteristics of a phantom can be controlled based on the precursors used to create it, where different characteristics may be required depending on what tissue needs to be simulated and for what application. This has led to the development of various types of tissue phantoms, and with the continuing development of instruments for molecular and tissue imaging applications, the need for the improvement and standardisation of tissue phantoms alongside these developments becomes increasingly essential[144].

This chapter looks to explore the use of silica sol-gels as simple tissue phantoms due to their highly scattering properties, where the characterisation of the particle sizes in such sol-gels is investigated using the fluorophore MeADOTA[61]. Being able to accurately measure the size of the nanoparticles in a sol-gel network in turn allows for greater control of the scattering properties, where the sol-gel precursors could be adapted as required to produce a gel that mimics the scattering properties of the tissue of interest. In addition to this, the properties of other fluorophores relevant to tumour margin estimation have been investigated in the sol-gel environment, where the combination of the fluorophores and sol-gels were then used to create phantom tumour margin samples. The ability of the translational stage-based fluorescence lifetime system described in Chapter 3 for detecting these phantom tumour margins was assessed to determine if this setup could be used as a calibration tool for margin estimation, where comparative FLIM measurements of ICG in a phantom margin were also conducted.

5.1.1 Optical Properties of Tissue

There are many characteristics of tissue that can affect the way light interacts with it, where the most common properties used to describe tissue include its absorption coefficient $\mu_a(\lambda)$, anisotropy coefficient $g(\lambda)$, scattering coefficient $\mu_s(\lambda)$, and refractive index n' [145] – all of which will vary depending on the type of tissue that is being measured. These properties can be used to determine how light may propagate through tissue, where photons can be absorbed by chromophores such as haemoglobin and melanin present in the tissue, reflected at the tissue-air interface, scattered, which therefore changes the direction of propagation of the photon, or can be remitted without interaction with any endogenous fluorophores[146].

The scattering of light in tissue is due to the presence of cells, where the changes in refractive index in a cell and its components compared to the surrounding tissue will cause a photon to change its path of propagation[147]. The anisotropy coefficient gives an indication of the forward direction retained after a scattering event based on the expected scattering angle. The size and morphology of the different cellular components will also affect the way light is scattered, where cell membranes and nuclei in particular have been shown to be a significant source of light scattering[148,149]. When the scattering that occurs is due to components with a characteristic size much smaller than the wavelength of light the scattering is termed Rayleigh scattering, and for scattering caused by particles on the order of or larger than the wavelength of light the term Mie scattering is instead used[150]. Both types of scattering can occur within tissue, where Rayleigh scattering refers to the light being isotropically scattered and Mie scattering when the light is predominantly forward scattered by a component of the tissue. The total attenuation coefficient $\mu_t(\lambda)$ is given by the sum of the absorption coefficient and scattering coefficient $\mu_a(\lambda) + \mu_s(\lambda)$. Properties such as these have been measured and tabulated for various tissue types and at various wavelengths of incident light[147,151,152], which can be useful references when looking to mimic a tissue of interest, but it also highlights the complexity of tissue optics.

5.1.2 Tissue Phantoms

Many tissue phantom variations have been developed to mimic the required properties of tissue, where phantoms can be designed in various forms such as aqueous suspensions, gelatines, resins and silicone depending on the application[144]. Various components can be added to the phantom matrix to mimic the properties of interest, where for each property different components will have their own advantages and disadvantages of their use in a phantom. Examples of absorbers that can be added include haemoglobin, molecular dyes or ink. Haemoglobin is useful for producing a more accurate biological simulation; however it is not as stable as the use of dyes or inks which can last days/weeks compared to only hours for haemoglobin. Examples of some of the most common scattering agents include lipids such as milk or Intralipid, which like haemoglobin for absorption are a good biological representation of what causes scattering in tissue. Polystyrene microspheres and metal oxide powders such as titanium dioxide can also be used as scattering agents, where the control over their size is excellent in terms of repeatability[144].

Publications on tissue phantoms appears to have grown steadily over the last 20 years based on a ScienceDirect search, where to date over 1,900 publications are available from 2019 alone[153] covering both new designs of phantoms themselves as well as their use in demonstrating new medical applications. Examples of recent publications include designing brain tissue phantoms for ultrasonic transcranial studies[154], using phantoms for the characterisation of time-resolved diffuse optical imaging systems[155] to be used for example for acquiring whole-head images of the infant brain[156], improving the production of agarose-based phantoms for use in magnetic resonance elastography (MRE)[157], as well as using a beeswax and polymer-based phantom to measure potential radiation doses that would be received in different organs of the body of a child[158]. While phantoms have a critical role in the development of many medical technologies, they are not without their drawbacks. Examples of such drawbacks that have been highlighted include being expensive to customise certain properties of tissue, inconsistency in the preparation leading to unwanted variation between phantoms[157], limited availability of commercial phantoms for certain

applications[159], as well as the difficulty in accurately mimicking the properties of complex organs such as the brain[160]. Such drawbacks highlight the continual need for improvement and development of tissue phantoms to aid the development of instrumentation.

5.1.3 Silica Sol-Gels

Silica sol-gels offer a potential avenue for tissue phantom development due to their ease of manufacture, the scattering nature of the nanoparticles within the sol-gel network and the ability to control the size of such nanoparticles and therefore the scattering properties. Indeed sol-gels have already found many applications in both medicine[161,162] and phantom development[163,164], therefore making them an ideal candidate for phantom studies in this work. Silica hydrogels are typically manufactured on an industrial scale, where mono silicic acid ($Si(OH)_4$) condenses to form siloxane monomeric structures ($–Si–O–H–$) which aggregate to form nanoparticles that grow in size. The network of particles will span the vessel in which they are contained at a time t_g, known as the gelation time. The polymerisation of hydrogels occurs through a series of hydrolysis and condensation reactions given by the following equations:

Hydrolysis: $$Na_2O.xSiO_2.yH_2O + H_2SO_4 \rightarrow Si(OH)_4 + Na_2SO_4 \quad (20)$$

Condensation: $$Si(OH)_4 + Si(OH)_4 \rightarrow 2SiO_2 + 4H_2O \quad (21)$$

Silica alcogels tend to offer higher purity and better -defined structures compared to hydrogels derived from sodium silicate, where tetraethyl orthosilicate (TEOS) or tetramethyl orthosilicate (TMOS) are used instead as a precursor in the sol-gel preparation. In the case of TEOS which is used in this work, this leads to a hydrolysis reaction given by:

Hydrolysis: $$Si(OC_2H_5)_4 + 4H_2O \rightarrow Si(OH)_4 + 4C_2H_5OH \quad (22)$$

This then leads to the same condensation reactions shown in Equation 21.

Since different sized particles have different scattering properties, having a cost-effective way of determining these particle sizes may allow for the more accurate and reproducible representation of tissue scatter in sol-gel phantom design. The Photophysics Group have previously demonstrated the capabilities of fluorescence anisotropy for measuring silica nanoparticles in a 1 – 10 nm range dispersed in solution, using both electrostatically and covalently attached dyes for the measurement of both stable LUDOX silica colloids and silica nanoparticles growing in the sol-gel process[165–167]. Fluorescence anisotropy has been shown to be capable of ~ 0.1 nm resolution and is both lower in cost and easier to use than more conventional methods for nanoparticle sizing such as small-angle x-ray scattering, small-angle neutron scattering, scanning electron microscopy and transmission electron microscopy. Despite the clear advantages of fluorescence anisotropy in nanoparticle metrology, there is still a need for improved dyes for this application. Potential errors and limitations include the possibility of dye aggregating on the nanoparticle causing depolarisation by means of energy transfer, the fluorescence lifetime of the dye restricting the upper limit of measurable rotational time, depolarisation due to dye wobbling or translating on the nanoparticle reducing the dynamic range of anisotropy measurement, and photochemical changes in the dye leading to a change in its fluorescence properties. There is also the added difficulty of intrinsic fluorescence when studying silica colloids, which can be difficult to quantify and can hide particle rotational information. The intrinsic fluorescence of silica colloids is particularly problematic when exciting in the ultraviolet region in particular. Figure 5.1 shows the difference in the fluorescence emission of a silica colloid LUDOX SM-30 at a 5% concentration in water at various excitation wavelengths. When the LUDOX is excited at 279 nm there is considerable fluorescence emission in the 300 – 350 nm region, whereas this diminishes rapidly as the excitation wavelength is increased. The lowest excitation wavelength used in this work is 339 nm. While there is still some fluorescence emission from silica at this excitation wavelength it will not interfere with measurements due to its longer fluorescence lifetime in comparison to NADH which is measured at this wavelength, as well as a much longer acquisition time being required to obtain sufficient data for the lifetime of silica under these conditions (see Section 5.4.2.2 for more details).

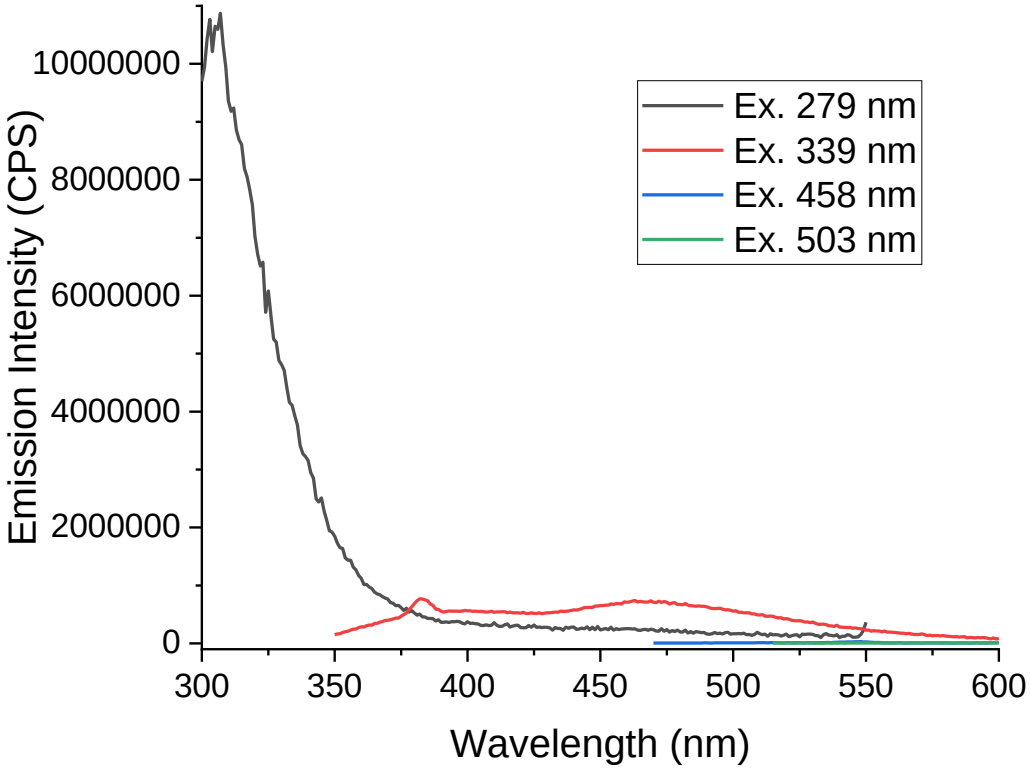

Figure 5.1: Fluorescence emission from LUDOX SM-30 diluted in water at various excitation wavelengths. Excitation at 279 nm resulted in greater fluorescence emission in the 300 – 350 nm range compared to the emission obtained using higher excitation wavelengths. Emission from silica is unlikely to interfere in measurements due to excitation wavelengths ≥ 339 nm being utilised in this work.

Both stable silica nanoparticles and growing silica sol-gel structures have been studied in this chapter using MeADOTA as a fluorescent label in fluorescence anisotropy measurements to better understand the development of a silica sol-gel network, as well as demonstrate the suitability of using MeADOTA for measuring a range of particle sizes on the nanometre scale. In addition to this, sol-gels are further utilised in the design of a phantom tumour margin, demonstrating the ease of preparing such a sample using sol-gels as well as the accuracy of determining the margin position using both FLIM and the fluorescence lifetime system that incorporates liquid light guides and a translational stage described in Chapter 3.

5.2 Experimental Setup

Fluorescence anisotropy measurements were performed on a HORIBA DeltaFlex system as described in Chapter 2 using TCSPC, where the general protocol for

anisotropy measurements has already been described in the same chapter. Excitation of MeADOTA was achieved using a 503 nm DeltaDiode operating at a 2 MHz repetition rate, and emission was collected at 570 nm. Anisotropy measurements using MeADOTA were performed over a 400 ns TAC range until a difference of 10,000 counts was achieved between I_{VV} and I_{VH} (unless otherwise stated). For the comparative R6G measurements, samples were also excited using a 503 nm DeltaDiode and emission collected at 570 nm, where a 100 ns TAC range was instead used.

For measurements of R6G, NADH and ICG in the sol-gel phantoms, samples were excited using a 494 nm NanoLED, 339 nm NanoLED and 775 nm DeltaDiode respectively, where emission was collected using 570 nm, 450 nm, and 835 nm longpass filters respectively. Samples were measured using the translational stage setup described in Chapter 3, where the cuvettes were initially placed with the very edge of the fluorophore-doped sol-gel directly under the liquid light guide collecting fluorescence. Samples were then moved in either ½ mm or 1 mm increments where the fluorescence lifetime was measured at each increment until the 25 mm position, where at this point both liquid light guides were above the region that contained un-doped sol-gel only. Figure 5.2 demonstrates the measurement protocol in more detail.

Measurements of ICG in the phantom margin were also performed on the HORIBA QuantiCam Lifetime Imaging Camera using the setup described previously in Chapter 2. Excitation was achieved using a 775 nm DeltaDiode operating at an 80 MHz repetition rate. An 801 nm dichroic mirror (Edmund Optics) with a reflection range of 450 – 790 nm and transmission window of 814 – 1100 nm was used to carry excitation light toward the sample, where an additional emission longpass filter with a cut-on wavelength of 800 nm (Thorlabs) was also utilised to minimise the collection of scattered light. The sample was moved in 1 mm increments and measured at each position as in the previous experiments, where the acquisition time at each position was 1 second and the collected image size was 42.98 x 69.40 μm.

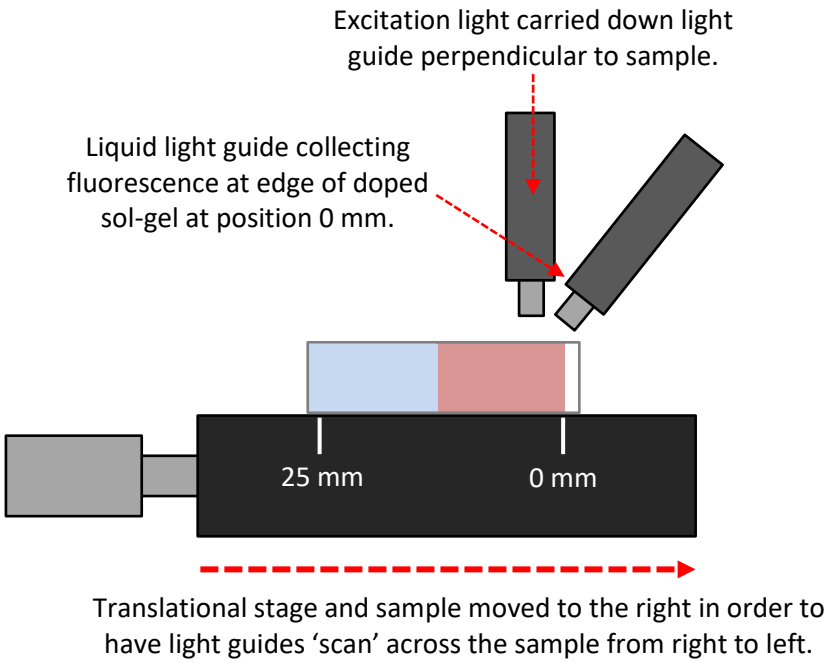

Figure 5.2: Sample setup for incremental measurements. The sample was initially positioned to have the light guide collecting fluorescence directly above the doped sol-gel edge at a 0 mm position. The stage was then moved in ½ or 1 mm increments as required towards the right, meaning the margin passed underneath the light guides at ~ 15 mm and both light guides were above the sol-gel only region at the 25 mm position. Figure not to scale.

Additional measurements of the fluorescence lifetime of ICG are also included in Section 5.4.3.2. These measurements were performed on a HORIBA DeltaFlex that incorporated improved timing electronics as well as an improved detection module (HORIBA HPPD-860) in comparison to those used for other lifetime measurements. This improved system was beneficial for ICG measurements due to its extremely short fluorescence lifetime.

5.3 Characterising Silica Nanoparticles Using MeADOTA

MeADOTA has been used in this work to measure both stable silica nanoparticles and growing silica nanoparticles in both hydrogels and alcogels due to its numerous advantages for use in fluorescence anisotropy. These advantages include its emission being towards the red region (λ_{em} *(max.)* ~ 560 nm), which should minimise background fluorescence from the silica, as well as its longer fluorescence lifetime (~ 20 ns), which allows for the measurement of longer rotational times.

5.3.1 LUDOX Nanoparticle Sizing

LUDOX silica colloids with varying particle radii that were studied previously[167] were chosen for comparison in this work, which covered particles of radii 3.5 nm, 6 nm, and 11 nm. These previous studies used the fluorescent dyes fluorescein 5(6)-isothiocyantate (FITC), R6G and 6-methoxyquinolinium (6-MQ) for fluorescence anisotropy measurements, where each dye comes with its own advantages and disadvantages for such an application. 6-MQ-based dyes have a long fluorescence lifetime component of ~ 25 ns making them suitable for the measurement of bigger silica nanoparticles; however it requires excitation in the ultraviolet region which can also excite the intrinsic LUDOX fluorescence. The fluorescence properties of LUDOX have previously been measured in this region and were shown to be complex[167]. While the cause of intrinsic LUDOX fluorescence is not clear, suggestions include being due to additives or trace metal ions in the silica, or even being from the silica itself, as fluorescence has been reported previously from glass samples prepared from silica[167,168]. The use of FITC and R6G can avoid interference from intrinsic LUDOX fluorescence as both dyes are excited at higher wavelengths (~ 500 nm), however the short fluorescence lifetimes of these dyes limits their use in measuring larger nanoparticles due to the minimal change in depolarisation that would occur during the fluorescence lifetime. As mentioned previously, MeADOTA combines both a longer fluorescence lifetime as well as a higher excitation wavelength making it suitable for this application.

5.3.1.1 Sample Preparation

LUDOX SM-AS (particle radii 3.5 nm), AM (6 nm) and AS-40 (11 nm) colloidal silica were obtained from Grace, which were diluted in water for measurement. SM-AS solutions were prepared at a 0.1% v/v concentration in water, and AM and AS-40 were prepared at a 2% v/v concentration. Sodium hydroxide or ammonium hydroxide were added to adjust the pH in order to stabilise the solutions (typically pH ~ 9 – 10).

5.3.1.2 Results & Discussion

Initially a silane derivative of ADOTA (Si-ADOTA) was utilised to covalently label the LUDOX colloids, where covalent labelling has been used previously with FITC bound to (3-aminopropyl) trimethoxysilane (FITC-APS) for the measurement of stable silica nanoparticles[169]. Covalent labelling can provide a more strongly bound fluorescent label compared to electrostatic binding and therefore minimise dye wobbling on the nanoparticle surface. In this case however, no depolarisation of Si-ADOTA was observed as the anisotropy decay did not fall to 0, indicating that Si-ADOTA aggregated with the LUDOX rather than binding solely to the LUDOX. Electrostatic labelling with MeADOTA instead proved successful, where the rotational correlational times and the corresponding particle sizes calculated for each colloidal silica nanoparticle sample measured are shown in Table 5.1, with the manufacturer-stated values also shown for comparison.

LUDOX	D_p **(cts)**	τ_{r1} **(ns)**	B_1 **(%)**	τ_{r2} **(ns)**	B_2 **(%)**	χ^2	r_p **(nm)**	r_m **(nm)**
SM-AS	3,000	3.48 ± 0.93	2.94	100 ± 18.0	97.06	1.18	4.6 ± 0.3	3.5
AM	3,500	4.08 ± 1.30	0.49	210 ± 19.5	99.51	1.05	5.9 ± 0.2	6.0
AS-40	12,000	12.1 ± 2.06	0.21	1424 ± 471	99.79	1.18	11.1 ± 1.1	11.0

Table 5.1: Fluorescence anisotropy decay analysis of various LUDOX colloids obtained using MeADOTA and Equation 17 and 18, where D_p is the number of counts in the difference peak, τ_r corresponds to the rotational correlation times, r_p is the calculated particle radius and r_m is the manufacturer radius. The τ_{r2} values were used to calculate the particle radii as these had the most significant contribution to the obtained decays.

Table 5.1 shows the agreement between typical measurements obtained using MeADOTA with the manufacturer's values apart from a slightly larger value obtained for SM-AS. This is most likely due to small aggregates of the colloid forming which can occur over time through atmospheric carbon dioxide entering the sample, leading to a lower pH and a higher average particle size. This has previously been observed in measurements of LUDOX SM-30 which are of equivalent size to

SM-AS. A value of 4.0 ± 0.4 nm was found in these previous measurements, which is within error to what was observed in this work[167]. In addition to this, the measurements of other equivalent particle sizes in this previous work using 6-MQ were also in good agreement with the MeADOTA measurements, however the 6-MQ measurements required ~ 100 x the number of counts and therefore an increase in measurement time to obtain comparable data afforded by MeADOTA. This difference is attributed to the 503 nm excitation of MeADOTA compared to the UV excitation of 6-MQ, where the intrinsic fluorescence decay of the colloid may mask the particle rotational information when labelled with UV dyes[121,167,170]. For comparison in Table 5.2, the precision of measurement with MeADOTA has been increased by increasing the number of counts in the difference peak.

LUDOX	D_p **(cts)**	τ_{r1} **(ns)**	B_1 **(%)**	τ_{r2} **(ns)**	B_2 **(%)**	χ^2	r_p **(nm)**	r_m **(nm)**
SM-AS	78,000	2.22 ± 0.17	3.86	78.0 ± 4.7	96.14	2.35	4.2 ± 0.1	3.5
AM	92,500	5.96 ± 0.53	0.83	216 ± 6.20	99.17	1.88	5.9 ± 0.1	6.0
AS-40	98,000	10.2 ± 1.92	0.16	1580 ± 342	99.84	3.96	11.5 ± 0.8	11.0

Table 5.2: Fluorescence anisotropy decay analysis of the LUDOX colloids measured with MeADOTA showing the same parameters as described in Table 5.1, but with up to ~ 26 times more counts in the peak of the difference curve D_p to test the precision of the measurements.

The results in Table 5.2 show that an increase in the number of counts makes little difference to the accuracy of the particle size obtained from the measurements, but the higher precision is reflected in the reduced statistical error. The precision in the measurements with MeADOTA are again shown to be significantly better than those obtained with 6-MQ despite the latter having a much higher count for D_p for all the colloids measured[167]. The χ^2 values are also larger in Table 5.2 than in Table 5.1. This is to be expected as the higher statistical precision can reveal small systematic errors such as scattered excitation, time-base non-linearity etc. No improvement in χ^2 was gained by adding further rotational times through residual anisotropy analysis.

5.3.2 Nanoparticle Growth in the Silica Sol-Gel Environment

The growth of silica nanoparticles in both hydrogels and alcogels has also been studied using MeADOTA. Previous studies utilised the fluorophore JA120 for the measurement of hydrogels due to advantages such as excitation at 650 nm and an ability to survive in acidic conditions. However, the fluorescence lifetime of JA120 is only ~ 1.8 ns in water, leading to a maximum size of ~ 4.5 nm being detected[165]. The longer lifetime of MeADOTA gives the ability to potentially measure larger particle sizes, and so hydrogels were prepared under similar conditions as the previous study to compare the particle sizes obtained when measured with a long- (MeADOTA) and short- (R6G) lifetime fluorophore.

The growth of silica alcogel structures has also been observed using MeADOTA. Previous work using Stöber (base-catalysed) conditions has demonstrated the control of silica nanoparticle size in the range of r_p = 3.1 nm – 3.8 nm measured using fluorescence anisotropy[166], where under such conditions orthosilicate gelation proceeds rapidly and less ramified to form more discrete nanoparticles. Earlier studies reported the growth of smaller silica structures over several weeks when prepared under acidic conditions and using R6G[171], where under these conditions cross-linking of more linear structures are observed prior to gelation[172].

The ability to control both the size and type of nanoparticle structure as well as characterise the size of particles produced to a high degree of accuracy could prove beneficial in the utilisation of sol-gel structures as tissue phantoms, as this would allow for the design of phantoms with particle properties specific to the tissue type of interest. The work presented in this section demonstrates how the use of MeADOTA in fluorescence anisotropy studies can successfully characterise nanoparticle size and growth in both silica hydrogel and alcogels.

5.3.2.1 Sample Preparation

Stock solutions of MeADOTA and R6G in methanol were initially prepared for use in anisotropy measurements. A small amount of each fluorophore in powder form

was dissolved in methanol, and the volumes of these stocks that were required to give an absorbance of ~ 0.1 for 3 mL samples were determined.

To study the growth of the acidic silica hydrogel nanoparticles, samples were prepared using similar methods to those described previously[165], and adjusted as necessary to produce a suitable volume of solution with an appropriate gel time to enable a direct comparison with previous results using the fluorophore JA120. Typically, 11.39 mL of Crystal 79 sodium silicate solution (PQ Corporation) diluted to an 8.14% v/v concentration in water was added to 5.73 mL of sulphuric acid at a 12% v/v concentration in water, giving a gelation time of ~ 50 h. The solution was mixed for 30 minutes and the initial pH was measured to be 0.94. 3 mL of the solution was added to two separate cuvettes, where MeADOTA was added and mixed into one cuvette and R6G into the other. Having a gel time of ~ 50 h was suitably long enough so that there would not be any significant changes in the nanoparticle sizes during the fluorescence anisotropy measurements, as these measurements took ~ 20 minutes to conduct. Measurements were conducted as quickly as possible to minimise the size distribution of the particles being detected due to the ongoing polymerisation of the hydrogel.

For silica alcogel measurements, TEOS-based gels were prepared under acidic conditions as described previously[171] and again were adjusted as necessary to provide suitable measurement conditions. Here, 7.5 mL of TEOS was mixed with 7.75 mL of ethanol, and 9.5 mL of water was then added along with a few drops of hydrochloric acid to catalyse the reaction. The sample was mixed thoroughly for 4 h, where samples had a gelation time of ~ 80 h.

5.3.2.2 Results & Discussion

To assess the effect of the difference in fluorescence lifetimes (MeADOTA ~ 20 ns, R6G ~ 4 ns) on the apparent particle size as polymerisation proceeds according to Equations 19 and 20, two identical hydrogel compositions were labelled separately with each fluorophore. Figure 5.3[173] shows the typical change in the fluorescence anisotropy decay obtained using MeADOTA for a sol with a gelation time of ~ 50 h.

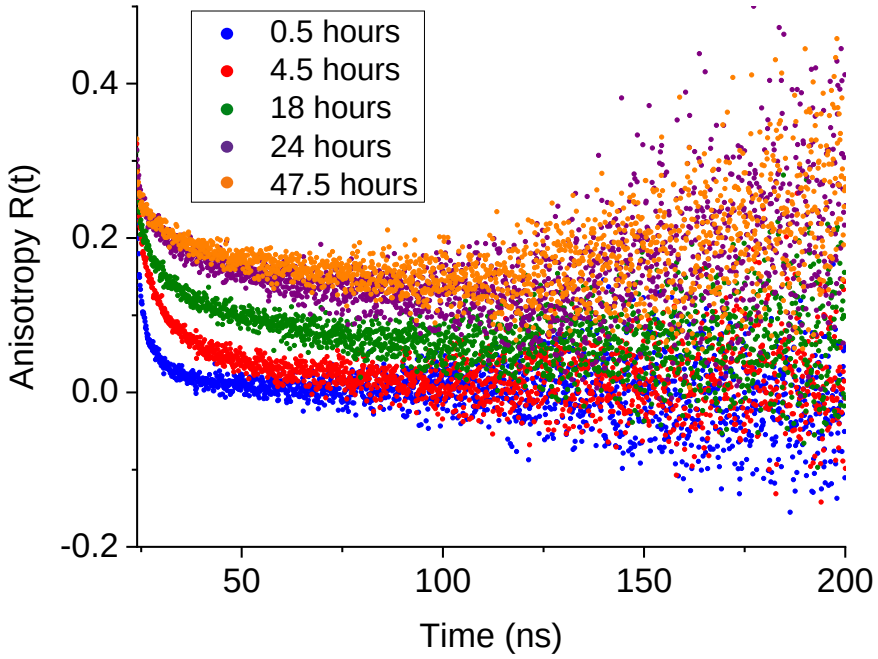

Figure 5.3: Changes in the fluorescence anisotropy for an acidic silica hydrogel with initial pH of 0.94 labelled with MeADOTA as polymerisation proceeds, where the acquisition at each time delay was ~ 20 min.

Figure 5.3 reveals that the initial anisotropy decays fall more rapidly towards 0 due to the smaller size of the particles at these earlier times. As the particles grow and the sol reaches the gelation point, the anisotropy decays do not fall to 0 due to the larger size of the particles, and the decays also become more similar in shape. In acidic hydrogels the silica particles are thought to grow initially by monomer addition and then diffusion controlled cluster-cluster aggregation[165], and would not be expected to grow continuously beyond the gel point as silicate is progressively used up in the hydrolysis and condensation reactions of Equations 19 and 20. Therefore, as the particles reach their finite size no further changes in the anisotropy decays would be observed. A levelling of the particle growth at ~ 25 h can also be seen in a plot of the radii calculated at each time point, as shown in Figure 5.4[173]. This may reflect a total consumption of available silicate; however it is also possible that larger particles are present with the finite fluorescence decay of MeADOTA limiting their detection.

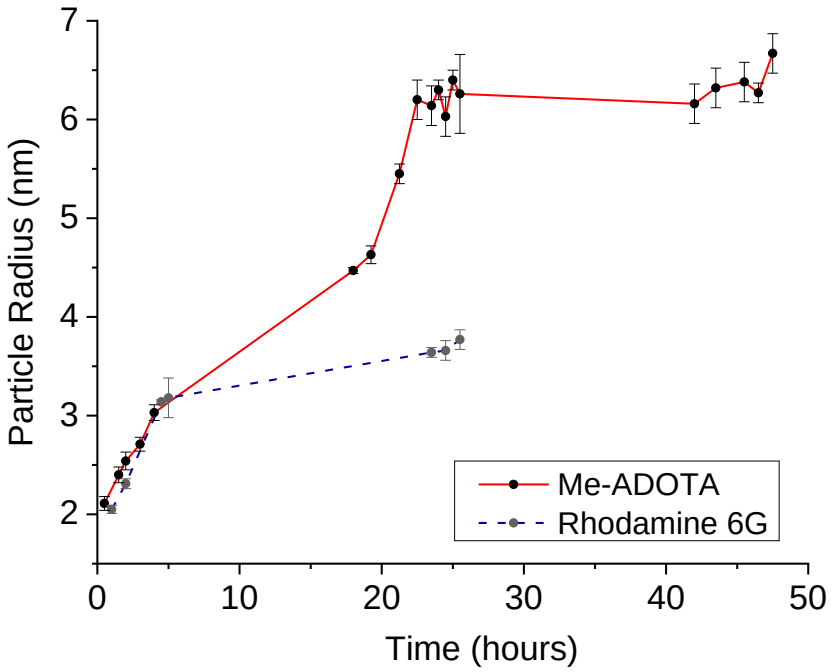

Figure 5.4: Comparison of the apparent change in average particle radius determined using MeADOTA and R6G during the polymerisation. Specific concentrations of the fluorophores were not required for these measurements, as anisotropy is a ratiometric measurement and therefore independent of fluorophore concentration[75]. Note that errors are from fitting and do not include systematic errors.

Figure 5.4 shows that the longer fluorescence lifetime of MeADOTA reveals the presence of larger particles (radius ~ 6.3 nm) compared to those detected by R6G (radius ~ 3.7 nm). The shorter lifetime of R6G is the most likely cause of a smaller maximum particle radius being observed in an identical hydrogel composition, as only a minimal change in depolarisation would occur during its fluorescence lifetime. This may also suggest that larger particles were also present in the previous work that used JA120 as the fluorescent label, where particle radii of up to ~ 4.5 nm were observed[165]. JA120 also has a very short lifetime (~ 1.8 ns), therefore this may have limited the maximum detectable particle size in the previous study.

The change in particle size in a TEOS-based alcogel prepared under acidic conditions was also monitored using MeADOTA. Table 5.3 shows the results of the anisotropy analysis of such measurements.

Time (hr)	τ_{r1} (ns)	B_1 (%)	τ_{r2} (ns)	B_2 (%)	χ^2	r_p (nm)
19.0	0.20 ± 0.19	16.01	3.00 ± 0.70	83.99	1.11	1.42 ± 0.10
21.0	0.34 ± 0.09	18.54	3.14 ± 0.83	81.46	1.02	1.45 ± 0.12
23.0	0.43 ± 0.11	21.51	4.03 ± 1.45	78.49	1.04	1.57 ± 0.17
43.5	0.30 ± 0.12	12.93	4.07 ± 1.14	87.07	1.03	1.58 ± 0.14
46.5	0.32 ± 0.11	14.27	4.50 ± 1.10	85.73	1.04	1.63 ± 0.12
48.5	0.83 ± 0.19	23.40	6.00 ± 2.26	76.60	1.06	1.79 ± 0.20
67.0	0.50 ± 0.14	14.95	6.13 ± 1.59	85.05	0.98	1.81 ± 0.14

Table 5.3: Fluorescence anisotropy decay analysis of MeADOTA in a TEOS sol-gel grown under acidic conditions, analysed using Equation 17 and 18. The τ_{r2} values were again used to calculate the particle radii due to these components having the most significant contribution to the obtained decays. Analysis started from ~ 19 h onwards as the decays obtained before this point were too short to reliably analyse.

Over a 48 h period a monotonically increasing nanoparticle radius of ~ 1.4 nm – 1.8 nm as determined from τ_{r2} is observed. This is consistent with the increased size of TEOS compared to TMOS, where previous studies found the hydrodynamic radius of silica structures derived from TMOS to be ~ 0.8 nm to 1.1 nm[171]. Such measurements provide a stern test of the resolution of the technique, and reveal close to 0.1 nm precision with D_p ~ 3,500 counts acquired in ~ 20 min. The τ_{r1} value is generally consistent with free dye rotation in water. It seems unlikely that changes in microviscosity η could account for the increase in r_p given the $r_p \sim \eta^{-1/3}$ power dependence in Equation 17, and previous work showing η decreasing rather than increasing as the precursors species are consumed[165,171].

5.4 Fluorophore Measurements in Silica Sol-Gels

As the silica sol-gels were to be used as a tissue phantom, measurements of various fluorophores of interest within the sol-gel environment were performed to assess how the more complex and highly scattering environment affected the fluorescence lifetime data obtained. The fluorophores of interest included R6G due to its ease of

detection, NADH as this is the intrinsic fluorophore of interest in this work, and ICG due its favourable properties for measuring its fluorescence in tissue as well as its already widespread use in fluorescence guided surgery. Each of these fluorophores was also measured in a phantom margin environment.

5.4.1 Rhodamine 6G Measurements

Measurements were performed using R6G to initially test the design of a phantom tumour margin. Sample margins were designed so that one half consisted of sol-gel only, and the other half was sol-gel doped with the fluorophore of interest (see Section 5.4.1.1 for more details). Since R6G can be easily observed under normal light when dissolved in solution, it would be seen clearly whether any R6G-doped sol-gel 'leaked' into the half of the sample that was supposed to be sol-gel only. The simple and well-established fluorescence properties of R6G also made it an ideal candidate for the initial assessment of the instrument described in Section 3.3.1 for margin estimation.

5.4.1.1 Sample Preparation

Silica alcogels were utilised in the phantom margin samples using methods similar to those previously described[174], where initially 9 mL of TEOS was mixed with 3 mL of water and 0.2 mL of 0.01 M hydrochloric acid for ~ 2 hours. Meanwhile, a stock solution of R6G was prepared by initially dissolving 1.44 mg of R6G in 30 mL of PBS, which was then further diluted by adding 1.8 mL of this stock to 28.2 mL PBS, producing a final stock of 6 μM concentration. This concentration as well as those used for NADH and ICG measurements in later sections were chosen in order to yield final samples that would have an absorbance of ~ 0.1, which is deemed appropriate for measuring the fluorescence lifetime accurately as previously discussed.

The phantom margin sample was then prepared by first adding 1.2 mL of the TEOS solution and 1.2 mL of PBS only to a cuvette which was mixed and left to gel, where

gelation occurred in ~ 30 min. This created the first 'layer' of gel to represent normal tissue. Once this had gelled, a further 1.2 mL of the TEOS solution and 1.2 mL of the 6 μM R6G stock was added. This was also mixed and left to gel, creating the second layer to represent cancerous tissue. Figure 5.5 illustrates how a final sample would look using a high concentration of R6G.

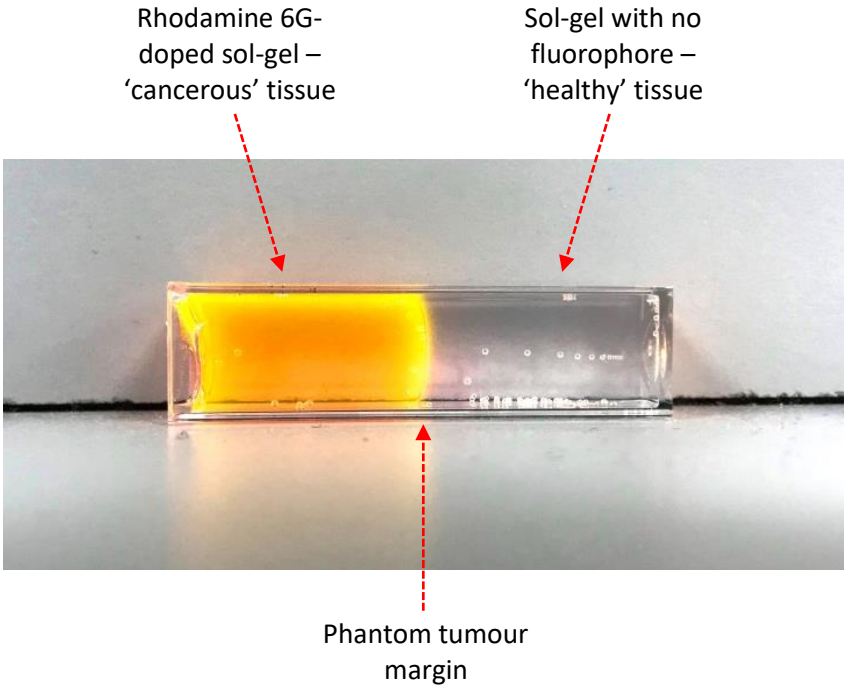

Figure 5.5: Example of how a final phantom margin sample would appear, where highly concentrated R6G was used in this sample to clearly highlight the margin line. The position of the margin line was determined in experimental setups through visual inspection of the line and corresponding light guide position above it.

5.4.1.2 Rhodamine 6G in a Phantom Tumour Margin

Measurements were taken of the R6G phantom margin sample at 1 mm increments until the light guides approached the margin, where measurements were then taken at ½ mm increments to see how the fluorescence decay changed over such small distances as the margin was passed under the light guides. Figure 5.6 shows a selection of the fluorescence decays obtained at various points across the sample, as well as the decay of a sample containing sol-gel only for comparison.

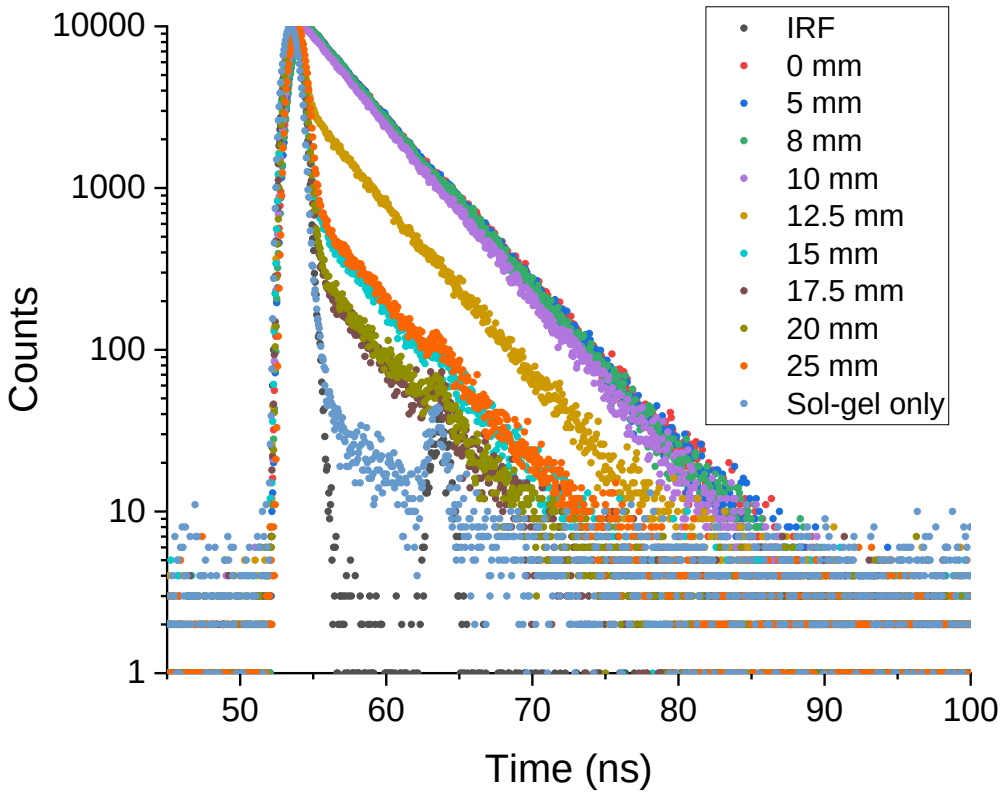

Figure 5.6: Fluorescence decays of the R6G phantom tumour margin sample at various positions, where from 0 mm – 14.5 mm the light guide collecting fluorescence was above the R6G-doped part of the sample, at 15 mm the same light guide was directly above the margin point as determined from visual inspection, and from 15.5 mm – 25 mm both light guides were above the un-doped sol-gel. Measurements were made at a 5 mm height above the sample, giving a beam size of ~ 7.3 mm in diameter based on 72° cone angle. See Figure 5.2 for indication of light guide positions above the sample.

Figure 5.6 shows that at positions far away from the margin when the light guides were above the R6G-doped sol-gel, the fluorescence decay strongly resembled that of R6G alone. This was also reflected in the lifetime parameters obtained, where a monoexponential fit suitably described the decay providing a fluorescence lifetime of ~ 4 ns as expected for R6G. As the light guides approached the margin point, a second exponential was required to fit the data due to the sharper fall at the start of the decay, which resembles that of a sample of only sol-gel. Figure 5.7 shows how the lifetime values and percentage contributions change as the position of the sample was changed, where a 2-exponential fit was used throughout for consistency.

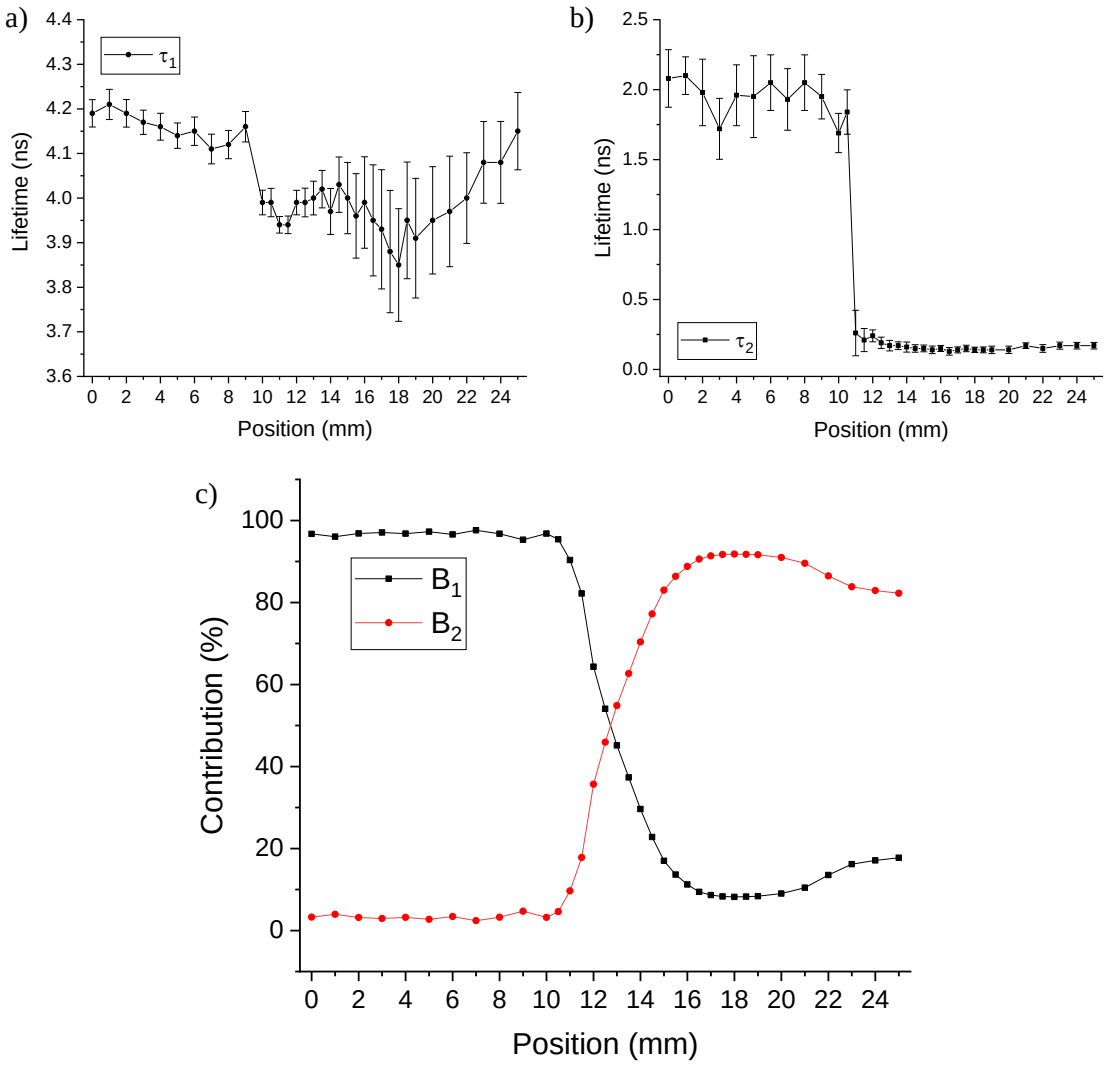

Figure 5.7: The change in a) τ_1, b) τ_2 and c) percentage contribution values to the fluorescence decays measured at each position of the sample, with the margin initially determined to be at the 15 mm position from visual inspection. The contributions to the decays were used for margin determination based on the data to then be compared with what was determined visually, where 16 mm was the closest position to the margin where the obtained values could be confidently attributed to being from the sol-gel only region.

Figure 5.7 a) shows that the value of τ_1 is consistent with that of R6G where no significant changes are seen in its value regardless of position, however the error bars do increase in size towards the later positions where at this point its percentage contribution also decreases to below 20%. Less influence from R6G at these positions would be expected as the light guides are above the un-doped sol-gel region. The biggest changes are seen in the value of τ_2 as well as the percentage contributions as the light guides approach and cross over the margin at 15 mm, the

position of which was determined from visual inspection. The short lifetime value observed is most likely multiple scattering from the sol-gel, where similar values of ~ 0.15 ns are seen for τ_2 in samples of the sol-gel alone. While there is good agreement in the τ_2 values of the phantom margin sample and a sol-gel only sample, the percentage contribution is a better indicator of when the light guides have fully traversed the margin as the τ_2 value is in good agreement with the sol-gel only sample from 13 mm onwards, which is before the margin position at 15 mm. Seeing this significant drop in the τ_2 value would be expected as the light guides approach the margin however, as part of the sol-gel only sample may still be illuminated by the light guide before the margin is reached.

Looking at the percentage contributions in more detail, the 16.0 mm position is the point where a contribution of > 85% from the short sol-gel component is observed, where values remain above the 85% mark from this point onwards in a reasonably consistent manner. The percentage contribution could provide a good figure of merit in this situation, where a contribution of > 85% from the sol-gel component of the sample could be deemed suitable confirmation that the margin has been fully surpassed by the liquid light guides. The ability to determine the sol-gel only region to millimetre accuracy is suitable for the surgical environment, as the smallest values found in literature as being the minimal acceptable clearance distance for surgical margins in certain cancers was 1 mm[175,176]. This figure of merit provided by the percentage contributions will be considered in later sections using NADH and ICG in phantom margins to determine if a similar figure is found for these fluorophores.

Measurements of an R6G phantom were also taken with the liquid light guides at 5 mm, 10 mm and 15 mm heights above the sample at various points across the sample to see how the values were affected, where these heights correspond to areas of illumination with diameters of ~ 7.3 mm, 14.5 mm and 21.8 mm respectively based on a 72° cone angle. Figure 5.8 shows a comparison of the lifetime components and percentage contributions of each component at each height at the different positions measurements were taken at. The surface of the liquid light guide interface used for exciting samples was used as the reference point to measure the height from the sample surface. Figures 5.8 a) and b) show that the values of τ_1 and τ_2 are in

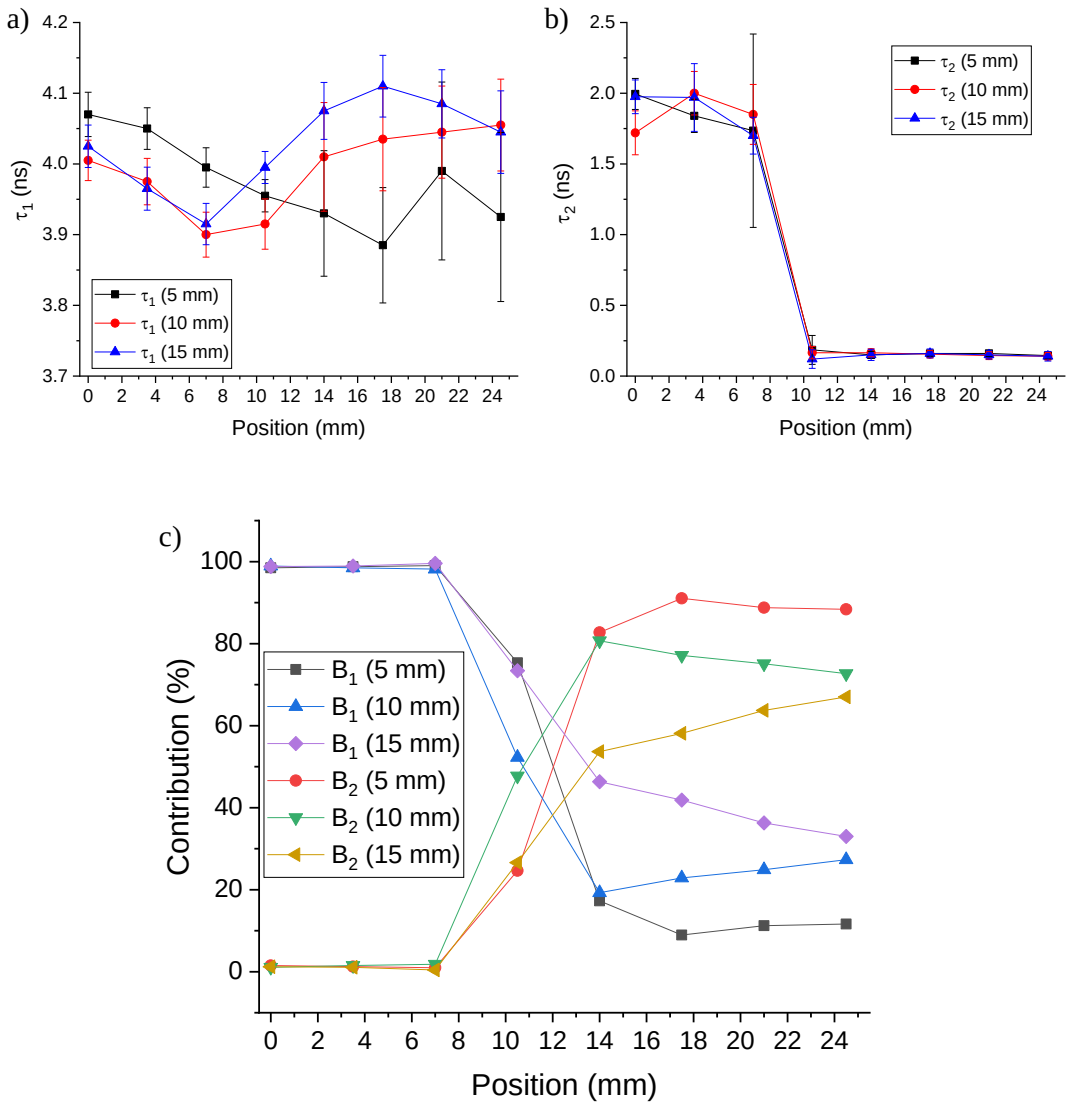

Figure 5.8: Comparison of a) τ_1, b) τ_2 and c) percentage contribution values found at heights of 5 mm, 10 mm, and 15 mm above the sample. The different heights above the sample correspond to different sized areas of illumination, where more of the sample will be illuminated at higher heights. Heights of 5 mm, 10 mm and 15 mm correspond to areas of illumination with diameters of ~ 7.3 mm, 14.5 mm and 21.8 mm respectively.

reasonably good agreement with each other regardless of what height from the samples the measurements are performed at. There are slightly bigger differences observed in the percentage contribution values show in Figure 5.8 c). As the light guides are moved away from the sample surface, the values of B_1 and B_2 become more similar. This would be expected, as the further away from the sample the light guides are, the larger the sample area is that can be excited or fluorescence can be collected from. This would mean that despite both light guides being directly above the sol-gel only region, part of the R6G-doped area may still be excited/fluoresce.

Despite this, the same general trend is followed in these values at each height as the light guides are moved across the sample surface. These results are promising as it demonstrates that the light guides would not need to be a specific height from a sample in order to accurately measure the lifetime or percentage contribution values; however, being closer to the sample may be beneficial to see a bigger difference in the latter values.

5.4.2 NADH Measurements

Studies were also conducted on NADH in the silica sol-gel environment, where in this case both hydrogels and alcogels were used. As the absorbance and emission properties of NADH are closer to that of silica, there was a greater chance of interference from the intrinsic silica fluorescence; therefore these measurements were performed to see how effectively the properties of NADH could be distinguished in this environment as this would be the intrinsic fluorophore of choice for distinguishing cancerous tissue from healthy tissue.

5.4.2.1 Sample Preparation

For measurements of NADH in the silica hydrogel environment, a stock solution of 4.25 mg of β-NADH in 30 mL of water at a 200 μM concentration was first prepared. The hydrogel itself was then prepared from methods derived from previous work as described in Section 5.2.2.1 but was adjusted this time to produce sol-gels with a much shorter gelation time. For this work, 10 mL of sodium silicate (4 v/v %) was mixed for ~ 5 minutes with 1.5 mL of sulphuric acid (2 v/v %). 0.5 mL of the NADH stock solution was then added to a cuvette with 2 ml of hydrogel solution, to produce a 40 μM sample of NADH in hydrogel. The sample was sealed with parafilm and mixed by hand for ~ 1 minute, where gelation occurred within ~ 15 minutes of mixing.

To prepare NADH in silica alcogel samples, stock solutions of 80 μM NADH in PBS were first prepared by dissolving 1.70 mg of β-NADH in 30 mL of PBS. A

TEOS/water/HCl solution was initially prepared in the same way as described in Section 5.4.1.1. Once mixed, 1.5 mL of this solution was added to 1.5 mL of NADH in PBS in a cuvette to produce a 40 μM sample, which was sealed and then mixed for a further minute, where gelation occurred within ~ 30 minutes of mixing.

For measurements of NADH in a phantom margin, a silica alcogel solution and NADH stock solution were prepared as already described. The phantom margin was created as described in Section 5.4.1.1 where the NADH stock was used instead of R6G.

5.4.2.2 NADH Fluorescence in Silica Hydrogel & Alcogel Environments

The fluorescence decay of NADH encapsulated in a silica hydrogel is shown in Figure 5.9. The fluorescence decay of NADH in water is shown as an example of the decay of NADH in a simple solvent environment, and the decay obtained for a sample consisting of hydrogel alone obtained in the same time frame as the NADH measurements is also shown for comparison. Measurements of NADH in the hydrogel were made using the same parameters for the measurements of NADH in the simple solvents. Figure 5.9 shows that the fluorescence decay of NADH in the silica hydrogel up to ~ 16 ns closely resembles the fluorescence decay of NADH in water, where a longer component towards the end of the decay is also observed. The longer component looks to be from the hydrogel itself, as this is a similar shape to that of the decay of the hydrogel alone at the same time. The fluorescence decay of NADH in an alcogel was measured under the same conditions and is shown in Figure 5.10, with similar comparison measurements to those shown in Figure 5.9 also included.

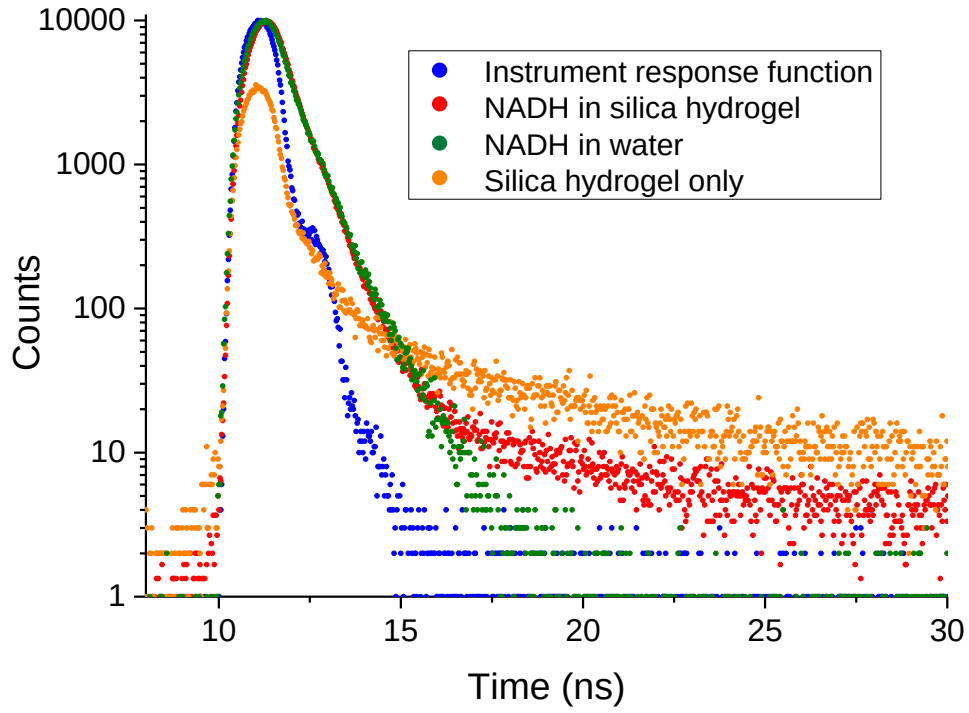

Figure 5.9: Fluorescence decay of NADH in a silica hydrogel, with the decay of NADH in water and of the silica hydrogel alone for comparison. The decay of the silica hydrogel alone was obtained in the same amount of time required to obtain the decay of NADH in the hydrogel to the desired 10,000 counts to give an indication of how much the fluorescence of the hydrogel may affect the NADH measurements in this period of time.

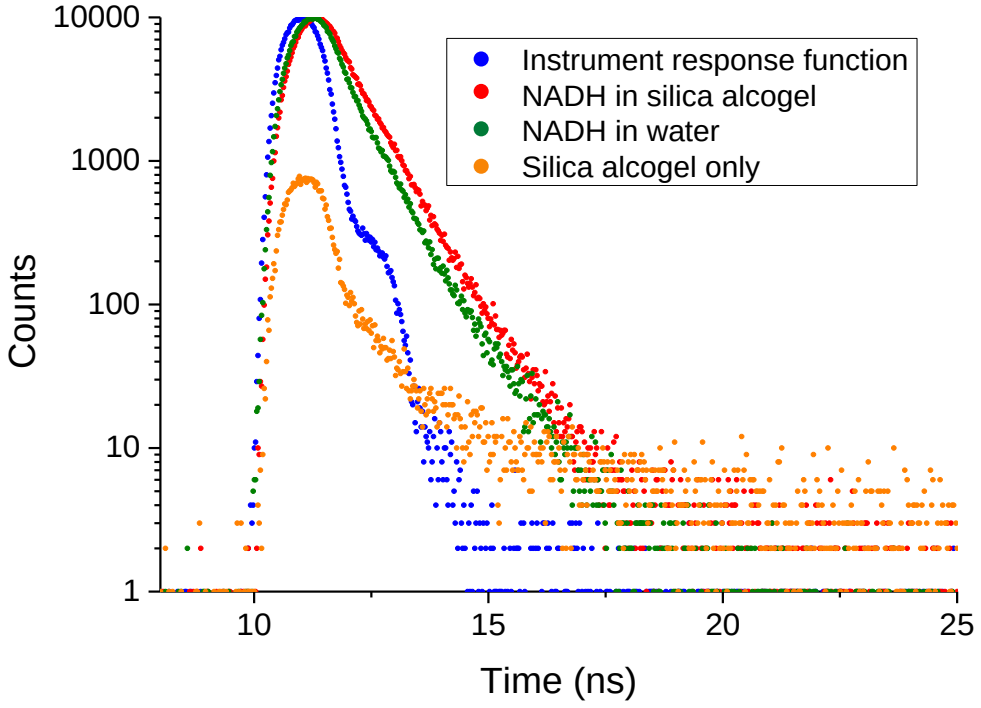

Figure 5.10: Fluorescence decay of NADH in a silica alcogel, with the decay of NADH in water and of the silica alcogel alone for comparison. The decay of the alcogel was again obtained in the same amount of time required for the decay of NADH in the alcogel to reach 10,000 counts. A lower number of counts in the peak were obtained for the alcogel measurements compared to that of the hydrogel, indicating that the alcogel does not fluoresce as strongly under these measurement conditions.

As alcogels have a higher purity compared to hydrogels, the fluorescence decay of NADH in the alcogel seemed to more closely resemble that of water, where there was almost no contribution at longer times from the alcogel. The decay of the alcogel alone also has a smaller number of counts in the peak compared to the decay of the hydrogel when measured for the same length of time, indicating there is less fluorescence from the alcogel under these measurement conditions and therefore should have less influence on the decay of NADH in this environment.

The lifetime parameters obtained for measurements of NADH in both the hydrogel and alcogel are shown in Table 5.4, where the parameters of the hydrogel and alcogels alone are also shown as well as NADH in water for comparison.

NADH Sample	τ_{r1} **(ns)**	B_{r1} **(%)**	τ_{r2} **(ns)**	B_{r2} **(%)**	τ_{r3} **(ns)**	B_{r3} **(%)**	χ^2
In silica hydrogel (full decay fit)	0.62 ± 0.04	47.74	5.35 ± 0.97	1.26	0.27 ± 0.02	51.00	1.20
In silica hydrogel (start of decay fit)	0.35 ± 0.02	78.11	0.88 ± 0.04	21.89	-	-	1.57
Silica hydrogel only	0.78 ± 0.14	11.96	5.01 ± 0.52	8.90	0.07 ± 0.02	79.14	1.01
NADH in silica alcogel	0.42 ± 0.05	64.00	0.95 ± 0.03	36.00	-	-	1.20
Silica alcogel only	0.14 ± 0.03	84.70	2.02 ± 0.33	15.30	-	-	1.27
NADH in water	0.34 ± 0.03	74.64	0.82 ± 0.03	25.36	-	-	1.01

Table 5.4: Corresponding fluorescence lifetime parameters obtained for the silica hydrogel and alcogel measurements shown in Figures 5.9 and 5.10. The lifetime components obtained for the full decay of NADH in the alcogel more closely resembled those observed for NADH in water only compared to those obtained from the full decay of NADH in the hydrogel.

Table 5.4 shows that a 3-exponential fit was required for the measurement of NADH in the silica hydrogel. While τ_2 can be attributed to a contribution from the hydrogel, the components τ_1 and τ_3 of NADH in the hydrogel do not reflect the components found for NADH in water alone. However, when only the first part of the fluorescence decay was used in the fit – the part that closely resembles the decay of NADH in water – a 2-exponential fit provided parameters that were very close to that observed for NADH in water.

In comparison to this, a 2-exponential fit was sufficient for the fit of the full fluorescence decay obtained for NADH in the silica alcogel. The two lifetime components are much closer to the two components obtained for NADH in water compared to what was observed in the hydrogel, where in addition to this no third lifetime component to represent a contribution from the alcogel was required to describe the data. The components obtained were slightly longer than that observed in water suggesting that there might still be some influence from the alcogel on the fluorescence decay of NADH, however the effect is still less significant in comparison to that of the hydrogel.

5.4.2.3 NADH in a Phantom Tumour Margin

Measurements were also made of NADH in a phantom tumour margin similar to that in Section 5.4.1.2, where Figure 5.11 shows a selection of the fluorescence decays obtained at various points across such a sample.

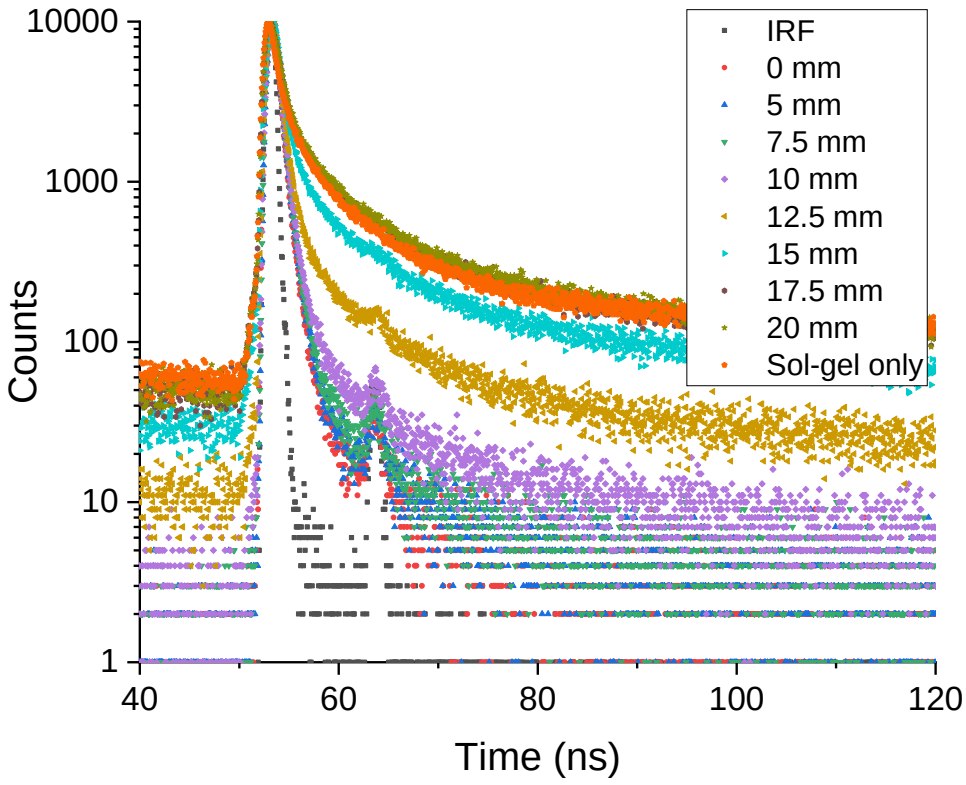

Figure 5.11: Fluorescence decays of the NADH phantom tumour margin sample at various positions, where from 0 mm – 14.5 mm the light guide collecting fluorescence was above the NADH-doped part of the sample, at 15 mm the same light guide was directly above the margin point as determined visually, and from 15.5 mm – 25 mm both light guides were above the un-doped sol-gel.

Looking at the shape of the fluorescence decays shown in Figure 5.11 suggests that the analysis of these decays would not be as straightforward as those observed for the R6G phantom margin sample. As previously discussed in Chapter 3, the shorter fluorescence decay of NADH highlights a secondary peak due to reflection that occurs when using the liquid light guide setup. This caused difficulty in the analysis of the fluorescence decays measured over the NADH-doped region of the sample in particular, where a good fit of the full decay was not obtainable despite reconvolution analysis being utilised. To work around this, measurements taken at positions 0 – 10 mm were analysed by fitting to just before the secondary peak, where the full fluorescence decay was analysed for measurements from 10.5 mm onwards as a good fit was obtainable for these measurements. Figure 5.12 shows how the lifetime values and percentage contributions change as the position of the sample is changed, where in this case a 3-exponential fit was used throughout for

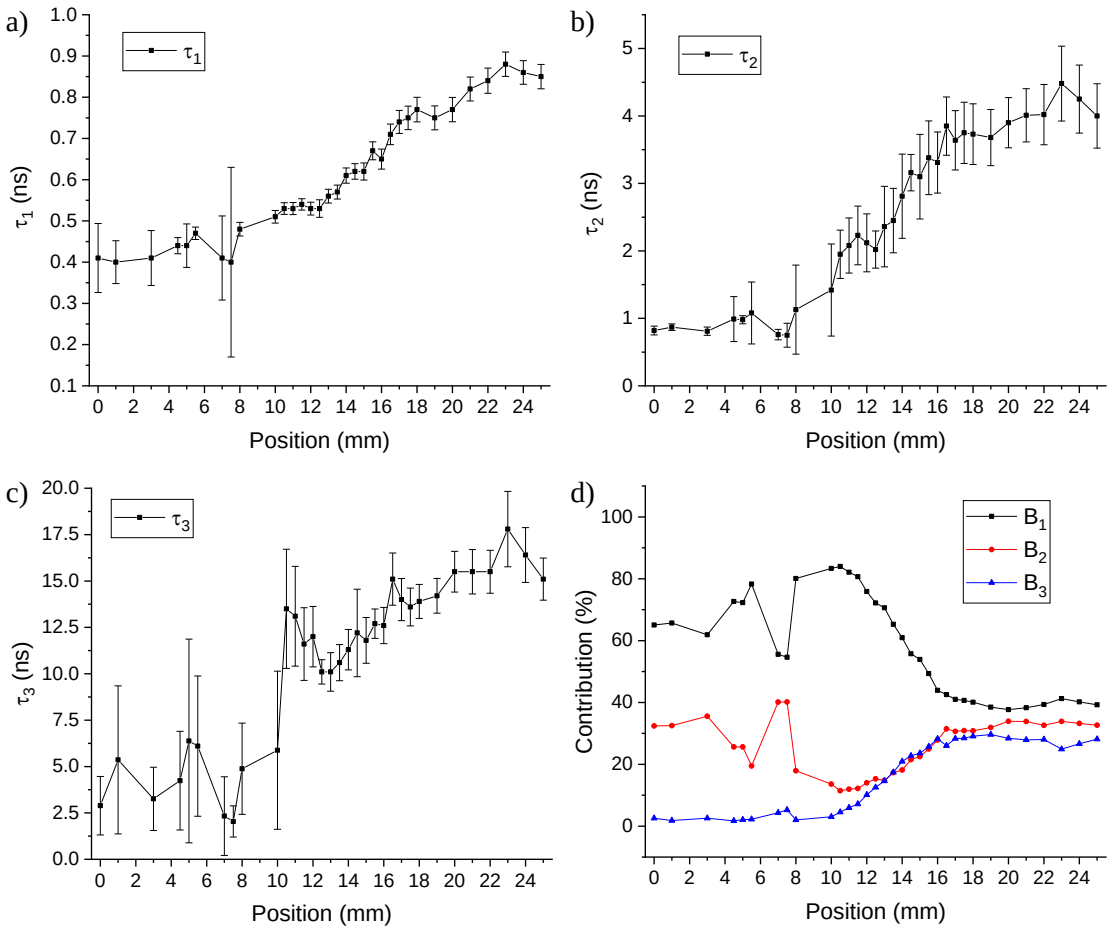

Figure 5.12: The change in a) τ_1, b) τ_2, c) τ_3 and d) percentage contribution values for the fluorescence decays measured at each position of the sample. Based on the percentage contributions again to remain consistent with the R6G-based figure of merit determination it was found that the value of B_3 which confirms the margin has definitely been surpassed by the light guides was 16.0 mm, which is 1 mm after the margin position.

consistency. 3-exponentials were required for the measurements in order to describe the two lifetime components of NADH as well as a component to describe the sol-gel fluorescence.

From Figure 5.12 it can be seen that from 0 mm - ~ 8 mm the τ_1 and τ_2 values obtained are in relatively good agreement with what was observed for NADH measured previously in an alcogel as well as water (see Table 5.4 for comparison). A steady increase in these values as well as in τ_3 is observed up until ~ 20 mm. τ_3 is a much longer component which is most likely a contribution from the alcogel itself. This was confirmed by measuring a sample consisting of alcogel only that was made from the same stock solutions, where analysis of the obtained fluorescence decay showed a much longer component of ~ 12 ns was required to describe the data.

Figure 5.12 also shows how the percentage contribution of τ_3 increases as the light guides approach and are moved over the margin, which would be expected when moving into the sol-gel only region and as previously observed for the R6G phantom margin sample. The contribution of all three lifetime components level out from ~ 16 mm onwards, where for example τ_1 remains at ~ 40% from 17 mm – 25 mm compared to an initial ~ 70%.

In terms of defining a figure of merit for the case of NADH using similar criteria as that used for defining a figure of merit for R6G, we can again look at the contribution from the sol-gel again in particular, which is τ_3 in this case. The percentage contribution from τ_3 increases from 2.55% at the 0 mm position to 28.14% at 25 mm. In comparison, the measurement of the sol-gel only sample had a contribution of 23.30% from the same lifetime component, therefore a contribution from τ_3 of > 24% could be considered as suitable confirmation that the light guides had fully surpassed the margin, which in this case is at 16.0 mm (1 mm after margin position) – the same position as that observed in the R6G measurements.

5.4.3 Indocyanine Green Measurements

ICG has also been investigated in the phantom margin environment. As discussed in Chapter 1, ICG is one of the few FDA approved dyes for use in surgery and has already been used in certain cancer surgeries, and so it was also studied here to assess the suitability of silica sol-gels as a tissue phantom for studies of ICG in the NIR region. Studies of ICG were also initially conducted in simple solvents to gain a better understanding of the fundamental fluorescence properties.

5.4.3.1 Sample Preparation

For measurements of ICG in the simple solvent environment, 2.35 mg of ICG was dissolved in 30 mL of water, dimethyl sulfoxide (DMSO), ethanol and ethylene glycol to produce a 100 µM stock solution of ICG in each solvent. 0.03 mL of each stock was then added to a cuvette with 2.97 mL of the same solvent to produce 1 µM

samples, which was then sealed for measurement. To prepare the stock of ICG for phantom margin measurements, 1.16 mg of ICG was initially dissolved in 30 mL water, which was then further diluted by adding 1.2 mL of this stock to 28.8 mL PBS for a 2 μM stock. ICG was initially dissolved in water as it did not dissolve readily in PBS directly. The alcogel solution and final margin sample were prepared as previously described.

5.4.3.2 ICG Fluorescence Properties

The absorption and emission of ICG in each solvent measured immediately after sample preparation are shown in Figure 5.13. The emission spectra in Figure 5.13 b) in particular indicates the sensitivity of ICG to its environment, where excluding water there is a redshift in peak position with increasing polarity. A similar effect has already been observed in Chapter 4 for the fluorescence emission of NADH, where the peak wavelength was lower in the less polar ethylene glycol compared to the other solvents. In addition to this, the emission intensity in the most polar solvent DMSO (again excluding water) is the highest. ICG has previously been reported as being sensitive to the polarity of its environment, where the fluorescence intensity was also observed to increase in the solvents of higher polarity[177,178]. Despite water being of higher polarity than DMSO, it is well-known that ICG is extremely unstable in aqueous solution and prone to aggregation[74,179,180], where the consequent increase in radiationless transitions may explain why the typical polarity effects are not observed for ICG in water. This aggregation is apparent when the fluorescence emission of ICG is compared in water and ethanol for example over time as shown in Figure 5.14, where the emission intensity begins to drop in water even just one hour after sample preparation.

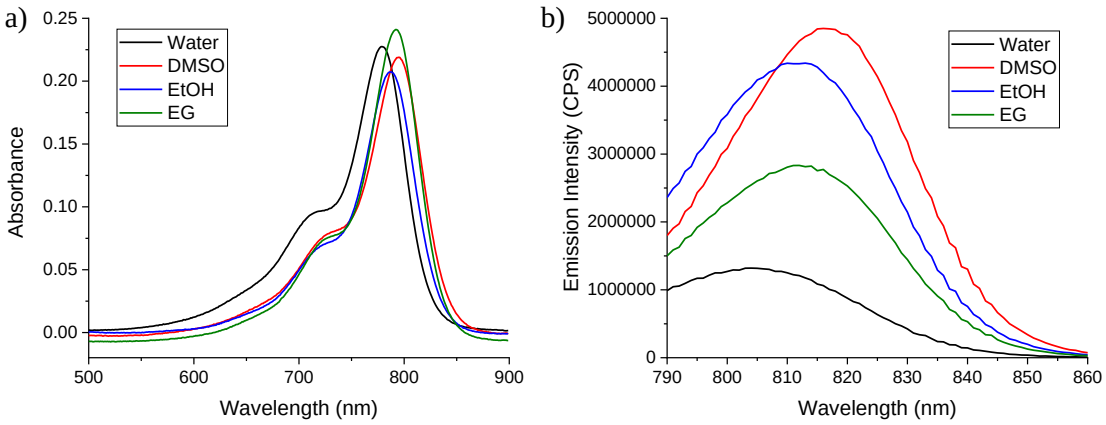

Figure 5.13: a) Absorption and b) emission spectra of ICG in water, dimethyl sulfoxide (DMSO), ethanol (EtOH) and ethylene glycol (EG). The emission spectra were collected at λ_{ex} = 780 nm. With the exception of water, an increasing solvent polarity increased the fluorescence emission intensity.

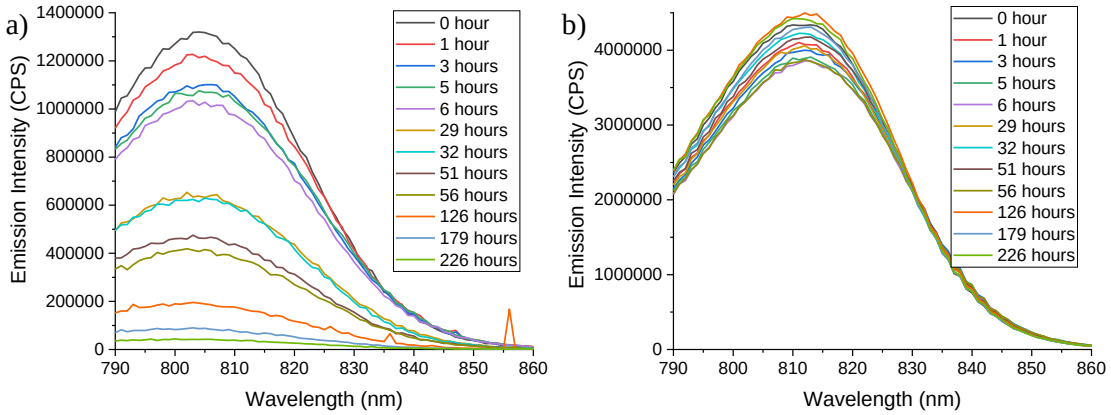

Figure 5.14: Change in emission intensity of ICG in a) water and b) ethanol from immediately after sample preparation to 226 hours after sample preparation, showing the vulnerability of ICG to aggregation in water.

The fluorescence decay of ICG in each solvent was also measured, where each decay is shown in Figure 5.15. The corresponding lifetime parameters are also shown in Table 5.5. The fluorescence decays and corresponding components of ICG in the various solvents again indicate the sensitivity of ICG to its environment. The fluorescence decay was found to be shortest in water and in agreement with previous studies[181,182], and the fluorescence decay was longest in DMSO which is also in agreement with previous work[182], where these results again indicate a correlation between the solvent polarity and fluorescence lifetime of ICG. DMSO was the only solvent where a monoexponential fit suitably described the data, however a major

contributing component of > 87% contribution was found in each of the 2-exponential fits of ICG in the other solvents.

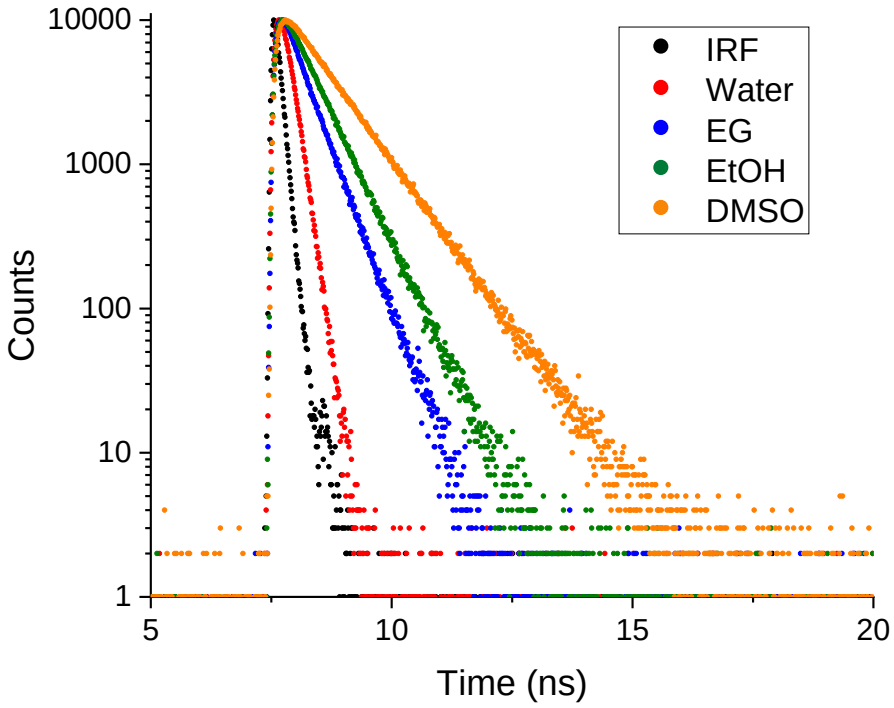

Figure 5.15: Fluorescence decays obtained for ICG in water, ethylene glycol (EG), ethanol (EtOH) and dimethyl sulfoxide (DMSO). Samples were excited using a 785 nm DeltaDiode instead of the 775 nm DeltaDiode used for the results shown in Section 5.4.3.3, and λ_{em} = 800 nm.

ICG Sample	τ_1 (ns)	B_1 (%)	α_1 (ns)	τ_2 (ns)	B_2 (%)	α_2 (ns)	τ_{avg} (ns)	χ^2
Water	0.17 ± 0.01	90.29	0.93	0.26 ± 0.04	9.71	0.07	0.18	1.07
EG	0.13 ± 0.02	12.53	0.35	0.47 ± 0.01	87.47	0.65	0.40	1.15
EtOH	0.30 ± 0.02	5.14	0.10	0.60 ± 0.01	94.86	0.90	0.57	1.23
DMSO	0.92 ± 0.01	100.00	1.00	-	-	-	0.92	0.96

Table 5.5: Corresponding lifetime components found for the decays shown in Figure 5.14, where the increase in fluorescence lifetime with increasing polarity further indicates the sensitivity of ICG to its environment.

5.4.3.3 ICG in a Phantom Tumour Margin

ICG was also studied using a phantom tumour margin as described previously for R6G and NADH. Measurements were initially made on the translational stage setup, where a selection of the fluorescence decays obtained at different positions is shown in Figure 5.16:

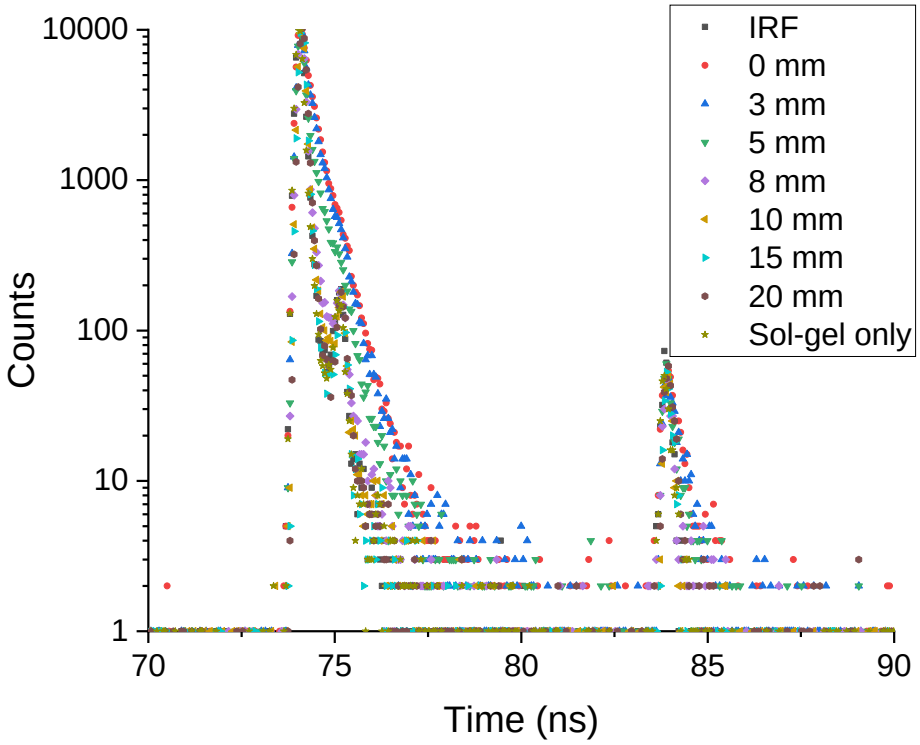

Figure 5.16: Fluorescence decays of the ICG phantom tumour margin sample at various positions, where from 0 mm – 14.5 mm the light guide collecting fluorescence was above the ICG-doped part of the sample, at 15 mm the same light guide was directly above the margin point, and from 15.5 mm – 20 mm both light guides were above the un-doped sol-gel.

The decays shown in Figure 5.16 highlight just how fast the fluorescence lifetime of ICG is, where lifetime values of 0.08 ± 0.02 ns and 0.35 ± 0.01 ns were found for the decay obtained at the 0 mm position. The data for such a short lifetime was indeed extremely difficult to analyse as the decays were not much longer than the IRF, which is the shortest possible decay that can be obtained from the system. The decays obtained also resembled the IRF from ~ 8 mm onwards when the light guides were still above the ICG-doped region and well before the margin at 15 mm. These results may indicate that the time resolution for the system is not precise enough for measuring the decay of such short-lived species such as ICG.

FLIM measurements were also made of ICG in a phantom margin using the prototype HORIBA Lifetime Camera system described in Section 2.2.5 to assess whether this system would be more suitable for determining the margin position using ICG. The field of view for this system is significantly smaller than what can be achieved with the light guide system, Images with an area of 42.98 µm x 69.40 µm can be obtained, therefore better resolution than the light guide setup would be expected. Figure 5.17 shows the FLIM images obtained before, on, and after the margin along with the corresponding fluorescence decays for each image. The images before and after the margin are at the positions closest to the margin where the image and decays entirely resembled the ICG-doped region and sol-gel only region respectively.

A 2-exponential fit of the decay of ICG 1 mm before the margin as shown Figure 5.17 was used, where an average lifetime of 0.44 ns was determined. This appears to be in good agreement with the corresponding FLIM image when compared to the scale. Noise reduction has been applied to the images and decays shown in both sets of data shown in Figure 5.17, however Figure 5.17 c) has had additional noise reduction applied by changing the intensity threshold from 0 – 500 counts to 30 – 500 counts. Increasing the lower limit removes pixels with a low number of photons, which can therefore influence the obtained FLIM image and not accurately represent the sample. In addition to this, changing this intensity threshold also limits the influence of the secondary ‘peak’ that can be seen in the images in Figure 5.17 b) at ~ 4 ns. This is thought to be due to reflections of the ‘stop’ signals on the SPAD array, which can occasionally trigger a time offset at high repetition rates such as at 80 MHz used here.

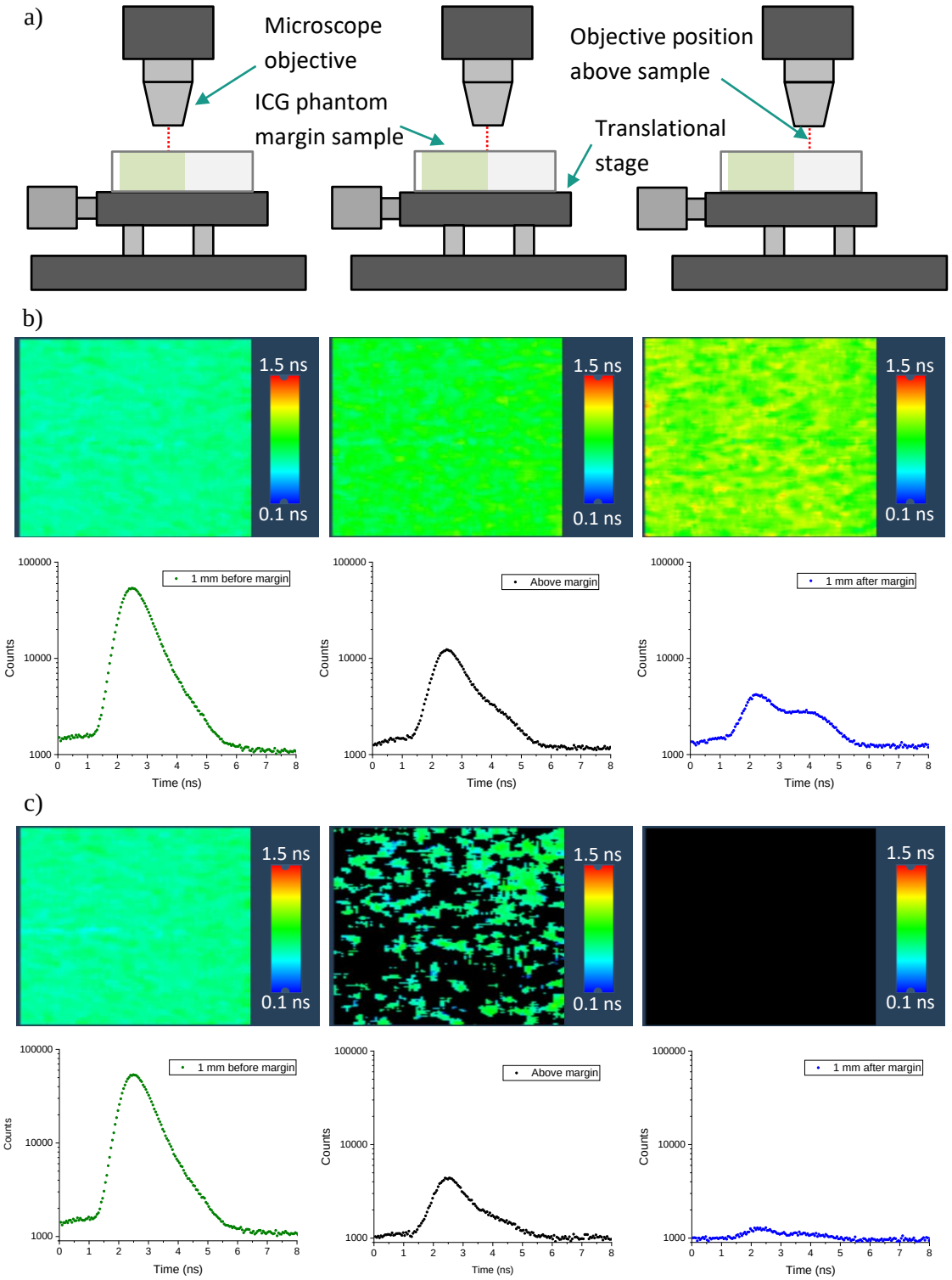

Figure 5.17: a) Experimental setup for obtaining FLIM images and the corresponding fluorescence decays shown in b) and c) of the ICG phantom margin sample, where the microscope objective was 1 mm before the margin (left), above the margin (middle) and 1 mm after the margin (right). Distances before and after the margin in the schematic have been exaggerated for clarity. A 775 nm DeltaDiode was used for sample excitation, an 801 nm dichroic mirror and 800 nm longpass filter were utilised to carry excitation light toward the sample and collect fluorescence. Noise reduction has been applied to the images, where b) shows the images and decays obtained when the intensity threshold was set to 0 – 500 photons, and c) 30 – 500 photons to further remove noise. Image areas are 42.98 x 69.40 µm in size. A video of the changing FLIM image as the objective is moved across the margin over a 4 mm distance can be found here.

Figure 5.17 also shows that when the objective is directly above the margin ICG fluorescence is still detected but is significantly reduced in comparison to what is observed 1 mm before the margin. Similarly, just 1 mm after the margin there is minimal fluorescence detected from ICG, where the image and decay mainly correspond to noise and instrumental artefacts. These results demonstrate the improved resolution of the FLIM system due to its small field of view in comparison to the liquid light guide system setup for measuring the change in the fluorescence decay of ICG in the phantom margin environment, as ICG was the dominant component in the FLIM measurements right up to the margin position whereas the sol-gel component was dominant in the liquid light guide measurements 7 mm before the margin was even reached.

5.5 Conclusions

Silica sol-gels offer a number of benefits for their use as a tissue phantom such as tuneable scattering properties through control of the particle sizes within the sol-gel network by changing the precursors, a relatively simple and reproducible process for creating the sol-gels as well as an intrinsic fluorescence that is stronger in the UV region much like human tissue. The fluorescent dye MeADOTA has been successfully utilised in this chapter for measuring the size of silica nanoparticles of both a stable size and growing size within a sol-gel network, demonstrating the capabilities of this long lived dye in combination with fluorescence anisotropy for precise measurements of nanoparticles with radii ranging from ~ 1.4 – 11 nm.

Silica alcogels were then utilised for creating phantom tumour margin samples, where one half on the phantom consisted of sol-gel doped with a fluorophore of interest, and the other half sol-gel only to represent clear human tissue. R6G was first used to test the sample design with the translational stage/liquid light guide-based fluorescence lifetime system described in Chapter 3. It was found using both R6G and NADH as the fluorophores in the doped sol-gel region that the fluorescence decays obtained 1 mm after the margin resembled that of sol-gel only, indicating that no fluorescence from that position onwards was collected from the fluorophore-

doped region. While acceptable surgical margins can vary depending on factors such as the type of cancer and even the country where the surgery takes place, values as small as 1 mm have reported as the minimal acceptable clearance distance for certain cancers[175,176]. Having methods that can rapidly determine surgical margins to millimetre precision would be extremely beneficial in cancer surgery, where fluorescence lifetime spectroscopy has been shown here to be capable of such precision from measurements that take < 2 minutes to conduct. This setup could be potentially utilised for determining surgical margins or for the calibration of future surgical instruments based on fluorescence lifetimes but would benefit from further work such as studies in more complex tissue phantom environments and real tissue samples.

In addition to R6G and NADH, ICG was also studied in the same tissue phantom environment. It was found that the translational stage/liquid light guide setup was not suitable for determining the margin position as precisely with ICG compared to the previously used fluorophores, as the system was only able to detect scatter from the sol-gel from 7 mm before the margin. This may be due to the fluorescence lifetime of ICG being so short and therefore having a very short decay, as the obtained decays were pushing the resolution limits of the system. Improved and updated timing electronics and system components may be required for better measurements using the translational stage-based system. FLIM measurements provided a much better estimation of the margin position for ICG. The FLIM system has a small field of view where images with dimensions of 42.98 µm x 69.40 µm were obtained, and therefore the image and corresponding fluorescence decays obtained just 1 mm after the margin clearly represented the sol-gel region only, demonstrating the improved resolution of measurements obtained with this system. These measurements therefore demonstrate the potential capabilities of such a system in margin estimation, where an ability to obtain images in almost real-time that show clear differences between a cancerous tissue region and healthy tissue region to 1 mm precision could provide an easy-to-use method for determining surgical margins intraoperatively.

When moving forward with further instrumentation development, it would be beneficial to weigh up the advantages and disadvantages of each system for the

desired application. The FLIM system provides almost real-time images, where the improved spatial resolution compared to the light guide-based system demonstrated from the measurements of ICG show the potential capabilities in precisely estimating the margin positions. While the spatial resolution of the liquid light guide-based system (in the case of ICG at least) is not as good and analysis of the individual decays is required as opposed to looking at an obtained image, it does offer its own advantages. This system would be of much lower cost than a FLIM based system and due to the small size and flexibility of the light guides, it would likely be a more ideal solution in a practical sense as the light guides can be moved with ease to any point of interest above a sample. Further comparisons with the other fluorophores as well as with more complex samples such as cells and tissue may be beneficial to help determine which system would be better to bring forward for further developments.

6. NAD(P)H Fluorescence in the Cell Environment

6.1 Introduction

After characterisation of NADH in various solvents and a sol-gel phantom, the next step was to try and observe the fluorescence lifetime in the more complex cellular environment. While measuring NADH in the sol-gel provided a scattering element similar to tissue, measuring in cells provides a more realistic medium. Complications include the presence of other endogenous fluorophores, some of which may absorb and fluoresce at wavelengths similar to that of NAD(P)H as discussed in Chapter 1. Figure 6.1[183] shows the absorption and emission spectra of some typical endogenous fluorophores.

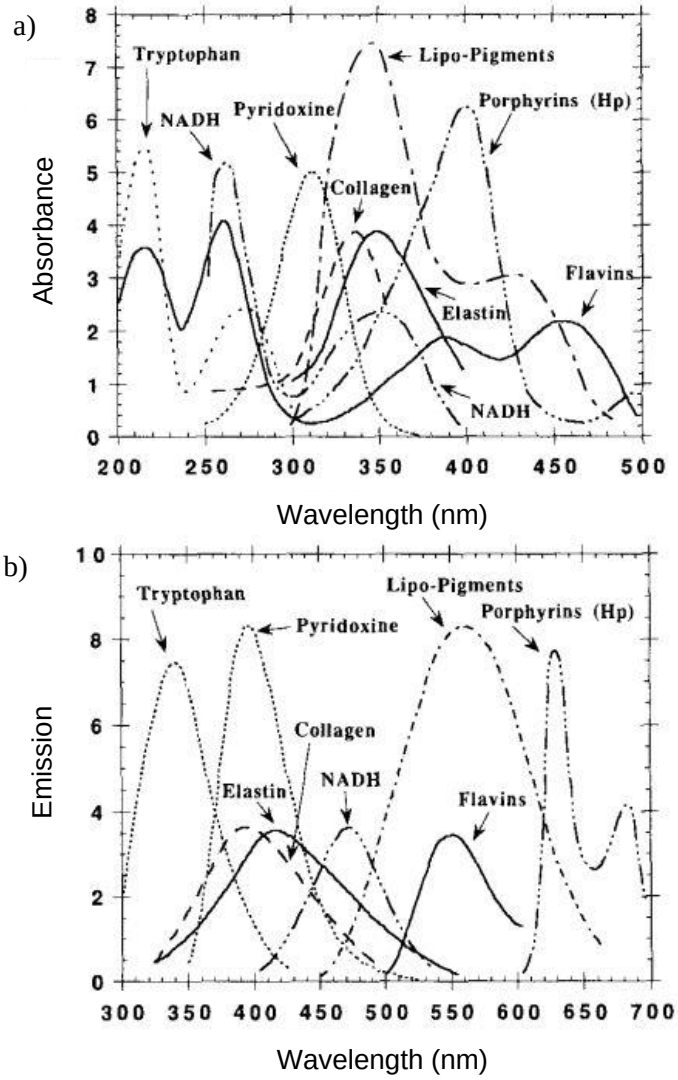

Figure 6.1: a) Absorption and b) fluorescence emission of various endogenous fluorophores present in cells and tissue, demonstrating the potential issue of distinguishing NAD(P)H fluorescence from other endogenous fluorophores.

Figure 6.1 shows that there is a significant amount of overlap in both the absorption and emission of NADH with other endogenous fluorophores, where collagen and elastin in particular appear to have both absorbance and emission profiles very similar to that of NADH. As collagen and elastin are found within the extracellular matrix between cells rather than in the cells themselves, they are extremely unlikely to influence the fluorescence decay of cells suspended in PBS as they are measured in this work. The fluorescence emission from these fluorophores would be more likely to interfere in fluorescence lifetime measurements of NAD(P)H in tissue samples, as tissue will contain collagen and elastin as well as a greater amount of other fluorophores of varying concentrations and distributions within the tissue[183].

An example of an endogenous fluorophore that may influence the fluorescence decay of NAD(P)H in suspended cells is pyridoxine. Pyridoxine – also known as vitamin B_6 – is a co-factor used in several biochemical reactions within the cell and has absorption and emission spectra that overlap the lower wavelengths of the NADH spectra as shown in Figure 6.1. Exciting and collecting the emission of fluorophores such as pyridoxine while trying to monitor NAD(P)H may lead to the fluorescence decays obtained being distorted and not truly representing NAD(P)H behaviour. Determining the best excitation and emission conditions for monitoring NAD(P)H specifically and combining this with known information on the fluorescence lifetime properties of NAD(P)H is crucial for studying NAD(P)H behaviour in cells, as investigated in this chapter.

6.2 Experimental Setup

Fluorescence lifetime measurements in this chapter were acquired using a HORIBA TemPro system using the TCSPC technique described previously. Excitation of the samples was achieved using a NanoLED excitation source at 339 nm and emission wavelengths were selected using longpass filters, where measurements in Section 6.4 onwards used a 450 nm longpass filter only for the emission wavelength. A TAC range of 200 ns was used in all measurements. Data analysis to determine the fluorescence lifetimes and corresponding parameters for all measurements was

performed using the DAS6 package using NLLS reconvolution analysis as previously described.

6.3 Changing Emission Wavelength

In order to establish which emission wavelength, if any, gave the largest difference in the fluorescence lifetime values of NAD(P)H between healthy (PNT2) and cancerous (PC3) cell lines, the fluorescence decay of each cell line was measured at different emission wavelengths between 400 nm and 530 nm.

6.3.1 Sample Preparation

To prepare cell samples for fluorescence lifetime measurements, one T25 flask of PNT2 cells (normal prostate epithelium, human) was cultured in Roswell Park Memorial Institute (RPMI) medium (Gibco, Thermo Fisher Scientific). 1 mL of cells was added to 4 mL of cell media in the flask, which was then placed in the incubator at 37°C with 5% CO_2 for 2-3 days. One flask of PC3 cells (cancer prostate epithelium, human) was also cultured using the same protocol, where these were instead cultured in Dulbecco's Modified Eagle Medium (DMEM) (Gibco, Thermo Fisher Scientific). After the incubation period the media was removed, and the cells were washed with PBS and then trypsinized to lift the cells off the flask surface. The volume of cells required to give a concentration of ~ 1 x 10^6 cells/mL in 2 mL of solvent was calculated, which was then added to a sterile tube and topped up with media to a 2 mL volume. This was centrifuged for 7 minutes at 1000 rpm to pellet the cells at the bottom of the tube. The media was tipped out and PBS was added to the 2 mL mark, where the cells were centrifuged again under the same conditions. Once the cells had pelleted again, the solution was tipped out for a second time to ensure as much cell media as possible had been removed from the final sample. 2 mL of fresh PBS was then added, where this final solution was added to a cuvette and sealed with parafilm prior to the fluorescence lifetime measurements.

6.3.2 Results & Discussion

The fluorescence decay of NAD(P)H in the cellular environment required a 3-exponential fit to model the data. Figure 6.2 shows a comparison of the three lifetime components obtained for each cell sample and at each emission wavelength the fluorescence lifetime was measured at.

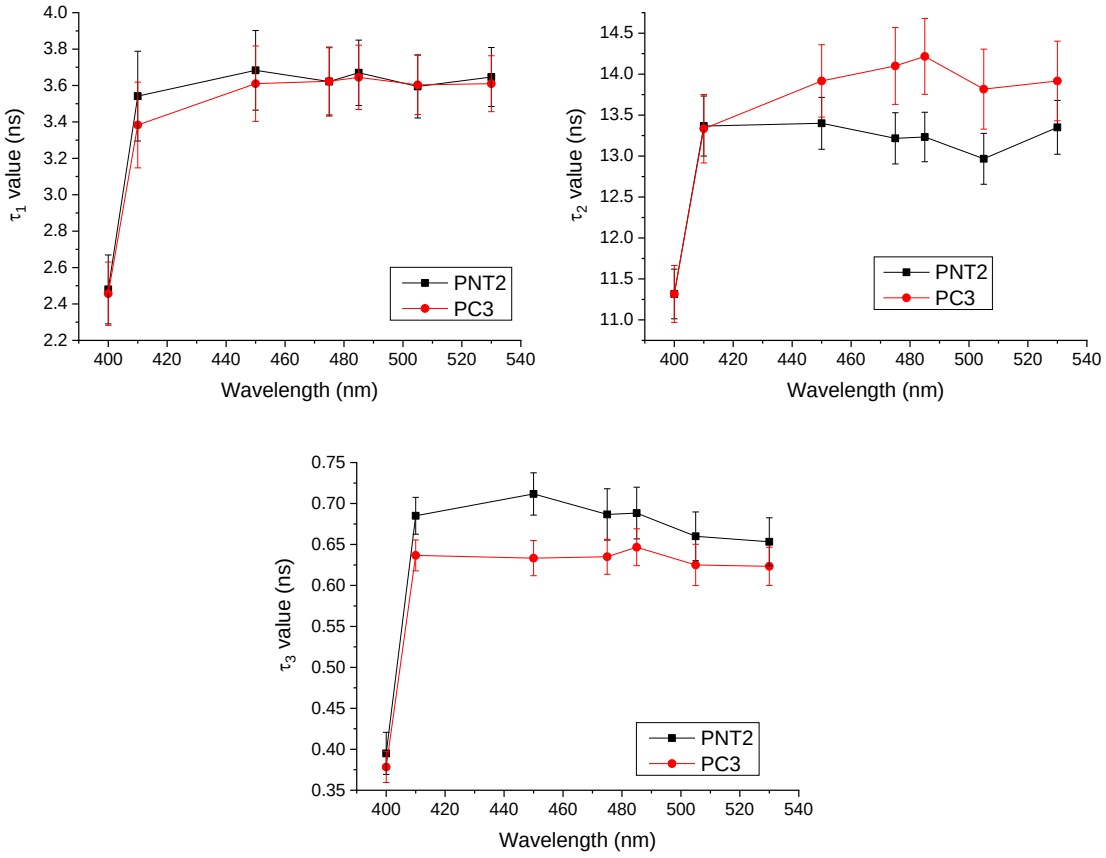

Figure 6.2: Comparison of the three lifetime components obtained for the fluorescence decay of NAD(P)H in PNT2 and PC3 cell samples for λ_{em} ranging from 400 nm – 530 nm. The biggest difference in values was observed at λ_{em} = 450 nm for τ_3, corresponding to unbound NAD(P)H.

Figure 6.2 shows that the lifetime values obtained at λ_{em} = 400 nm are much shorter compared to the longer emission wavelengths, where from λ_{em} = 410 nm upwards the values remained reasonably consistent. The difference in values at λ_{em} = 400 nm could be due to other intrinsic fluorophores fluorescing under these conditions such as pyridoxine as previously discussed, as this has an absorption maximum of ~ 315 nm and an emission maximum of ~ 400 nm[183]. In addition to this, the average

fluorescence lifetime of pyridoxine is reported to be ~ 0.78 ns in water[184] which is shorter than the average lifetime of NAD(P)H in cells; this could therefore be having a greater influence on the obtained fluorescence decay at this emission wavelength.

Based on these results an emission wavelength of 450 nm was chosen for future cell comparison measurements, as the most significant difference in lifetime values is observed at this wavelength for τ_3. While there are also statistically significant differences observed in the value of τ_2 at λ_{em} = 475 nm and λ_{em} = 485 nm, the peak emission wavelength of NAD(P)H is known to be ~ 450 nm (see Figure 6.1), and so choosing an emission wavelength closer to this for fluorescence lifetime measurements means that the collected fluorescence decay can more likely be attributed to NAD(P)H. This difference in τ_3 between the two cell lines can therefore be potentially monitored in other cell work to determine if environmental changes enhance or decrease this difference. The lifetime values obtained at λ_{em} = 450 nm for each cell sample are shown in Table 6.1 in more detail.

	τ_1 (ns)	B_1 (%)	α_1	τ_2 (ns)	B_2 (%)	α_2	τ_3 (ns)	B_3 (%)	α_3	τ_{avg} (ns)	χ^2
PNT2	3.68 ± 0.22	41.43	0.19	13.4 ± 0.3	26.42	0.03	0.71 ± 0.03	32.15	0.78	1.70	1.21
PC3	3.61 ± 0.21	41.39	0.16	13.9 ± 0.4	19.93	0.02	0.63 ± 0.02	38.68	0.82	1.35	1.22

Table 6.1: Fluorescence lifetime components obtained for NAD(P)H in PNT2 and PC3 cell samples for λ_{em} = 450 nm, along with the normalised pre-exponentials and corresponding contribution of each component to the fluorescence decay. A decrease in the average lifetime as well as an increase in the ratio of unbound/bound NAD(P)H based on the normalised pre-exponentials is observed in the PC3 cells in comparison to the PNT2 cells.

Previous studies on the fluorescence lifetime of NAD(P)H in the cell environment often describe the fluorescence decay using a 2-exponential model, where each lifetime component corresponds to NAD(P)H in either free or bound form[127,185]. However from the measurements obtained in this work, it was found that a 3-exponential model best described the data, as a 2-exponential model resulted in both

a large χ^2 value and sinusoidal weighted residuals, and a 4-exponential model did not improve the χ^2 value any further. This has also been reported in the literature in the measurement of fibroblast and adipocytes as well as in the measurement of stem cells[186,187]. A 4-exponential model has even been used to describe the fluorescence decay of NAD(P)H, where this has been used for measurements in isolated rat mitochondria[188]. Differences in the number of components used could be due to various factors. One such factor could be the measurement technique being used and the precision of the corresponding data analysis, as well as the goodness of fit that was required of the data in each of the previous studies for their applications. Another factor could be the types of cell lines used in the measurement of NAD(P)H fluorescence, as the binding of NAD(P)H is likely to vary depending on which cell type it is in. The preparation of the samples for measurement e.g. whether the cells are fixed or in suspension or whether certain cell components have been isolated for measurement could be another contributing factor. Despite the discrepancies it is still generally accepted that the shorter values in each of the models represent the NAD(P)H in free form, and the longer values are that of NAD(P)H bound to enzymes or proteins[189].

Looking at the obtained fluorescence lifetime values in more detail provides insight into what each component can most likely be attributed to in these cell environments. The first lifetime component τ_1 is most likely from NAD(P)H bound to enzymes, as this has been widely reported to have values between 1 – 6.5 ns depending on the target NAD(P)H is binding to[127]. The second lifetime component τ_2 is also likely to be NAD(P)H in its bound form, but perhaps to a larger enzyme or protein than what is represented in τ_1, where longer lifetimes of ~ 9 – 10 ns have also been previously reported[186,190]. The α value for this component is very small (α_2 = 0.02), which indicates there is a very low amount of NAD(P)H bound to the larger enzymes in comparison to unbound NAD(P)H and that bound to smaller enzymes. The third component τ_3 can most likely be attributed to unbound NAD(P)H, as this component is much shorter and is also in good agreement with the average lifetime of NADH free in solution measured in the work in Chapter 4.

Comparing the fluorescence lifetimes obtained from both cells, the biggest difference observed from the results in Table 6.1 is in the average lifetime value, where there is a decrease in this value in the cancerous cells compared to the healthy cells. This difference will be due to the combination of the decrease in value of τ_3 as well as the increase in the contribution to the decay of τ_3 for the PC3 cells. It will also be interesting to observe changes, if any, in the individual lifetime components in future measurements, as these can provide more detailed information on the behaviour of the different conformations of NAD(P)H within the cells.

The ratio of the normalised pre-exponentials represents the concentration ratio of unbound/bound NAD(P)H (in this case, $\alpha_3/(\alpha_1 + \alpha_2)$). It is known that a change in this ratio indicates a change in metabolism in the cells, where in this case a shift towards a higher ratio of $\alpha_3/(\alpha_1 + \alpha_2)$ indicates a shift to glycolysis and therefore cancerous behaviour[191]. The ratios of unbound/bound NAD(P)H for the PNT2 and PC3 samples measured are 3.55 and 4.56 respectively calculated from Table 6.1, therefore an increase in the ratio is observed from the healthy to cancerous cells as expected.

6.4 Incubation with Rotenone

To fully ensure the fluorescence decays obtained were due to NAD(P)H fluorescence rather than other fluorescent components within the samples, cells were incubated with rotenone. Rotenone is a known inhibitor of complex I in the mitochondrial respiratory chain, which in turn halts NADH oxidation and increases the concentration of free NADH in the mitochondria[186]. Decreases in all fluorescence lifetime components have been reported in the literature following rotenone incubation[127,186,192]; therefore the fluorescence decay was measured for PNT2 cell samples both with and without rotenone incubation to determine if a decrease in these lifetime values was observed in our own measurements.

6.4.1 Sample Preparation

A stock solution of rotenone was first prepared, where 1.18 mg of rotenone (Sigma Aldrich) was added to 30 mL of DMSO to obtain a 100 μM solution. This was further diluted down to a 50 μM solution by adding 15 mL of the original stock to 15 mL of PBS, where the 50 μM solution was used for incubation with the cells.

Two T25 flasks of PNT2 cells were cultured in RPMI medium under the same conditions as previously described. After the incubation period, 1.5 mL of the rotenone solution was added to one flask and placed back in the incubator for a further 5 minutes. After this time the media and rotenone solution were removed, where again the same protocol as described in Section 6.3.1 to prepare the samples for fluorescence lifetime measurements was followed. The second flask of cells was prepared in the same way, excluding the incubation with rotenone as this sample was to be used as the control.

6.4.2 Results & Discussion

Figure 6.3 shows the fluorescence decays obtained for the PNT2 cell samples prepared with and without rotenone incubation. Table 6.2 shows the corresponding lifetime components. Looking at the fluorescence decays in Figure 6.3 alone shows a visible decrease in the decay in the cell sample that was incubated with rotenone. This is further confirmed by the decrease in all lifetime values observed after incubation observed in the results in Table 6.2. In addition to this, an increase in the normalised pre-exponential of τ_3 is also observed, corresponding to an increase in the concentration of free NAD(P)H. This indicates that the rotenone has successfully inhibited the oxidation of the NADH back to NAD+, further confirming that the fluorescence decay obtained was that of NAD(P)H.

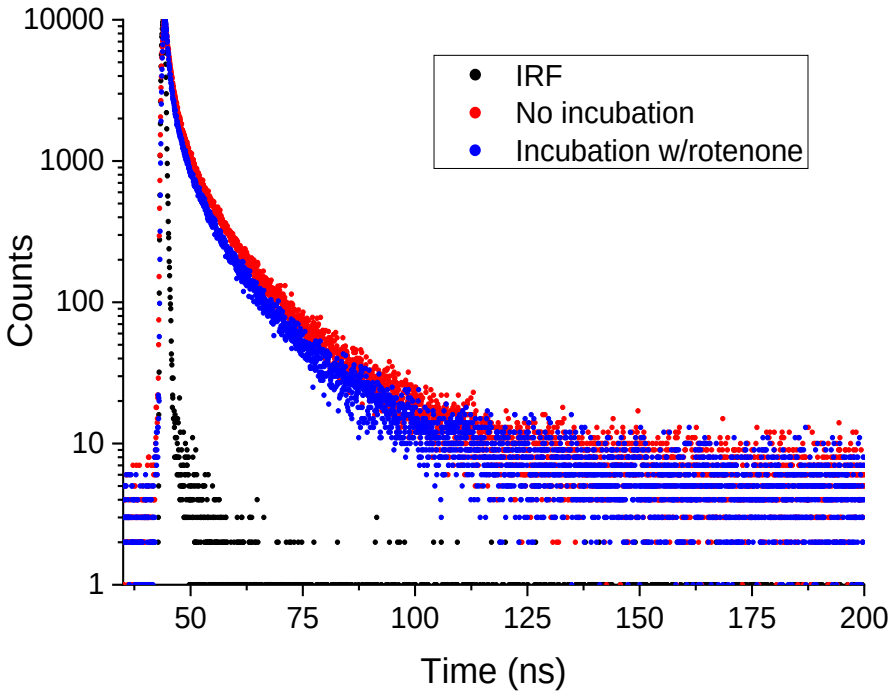

Figure 6.3: Fluorescence decays of PNT2 cells suspended in PBS following no incubation (•) and 5 minutes incubation (•) with rotenone, where a visible shortening of the decay is observed after rotenone incubation.

	τ_1 (ns)	α_1	τ_2 (ns)	α_2	τ_3 (ns)	α_3	τ_{avg} (ns)	χ^2
No rotenone incubation	3.80 ± 0.22	0.20	13.4 ± 0.3	0.04	0.72 ± 0.03	0.76	1.84	1.20
5 min rotenone incubation	3.26 ± 0.21	0.15	12.6 ± 0.4	0.02	0.58 ± 0.02	0.83	1.25	1.25

Table 6.2: Fluorescence lifetime components along with the normalised pre-exponentials obtained from measurements of PNT2 cells with and without rotenone incubation, where there is a decrease in all lifetime values following incubation as previously reported in literature.

6.5 Cell Measurements Using the Liquid Light Guide-Based Systems

Measurements of the PNT2 and PC3 cells were also performed on both liquid light guide-based instrument setups described in Sections 3.2 and 3.3 to see how the setups performed when measuring NAD(P)H in the complex cell environment. Results are shown for PNT2 only, as the PC3 measurements yielded similar results. The results for PC3 measurements are shown in Appendix C.

6.5.1 Sample Preparation

PNT2 and PC3 cells were cultured as previously described in Section 6.3.1. The volume of cells required to give a concentration of ~ 1 x 10^6 cells/mL in 4.8 mL of solvent was calculated instead of 2 mL as previously calculated. This was to ensure that the cuvette would be almost completely full and therefore no air bubbles would appear when lying on its side for measurements on the translational stage.

6.5.2 Results & Discussion

A comparison of the PNT2 decays obtained on each light guide-based system with that obtained on the conventional filter-based setup used in Section 6.3 is shown in Figure 6.4.

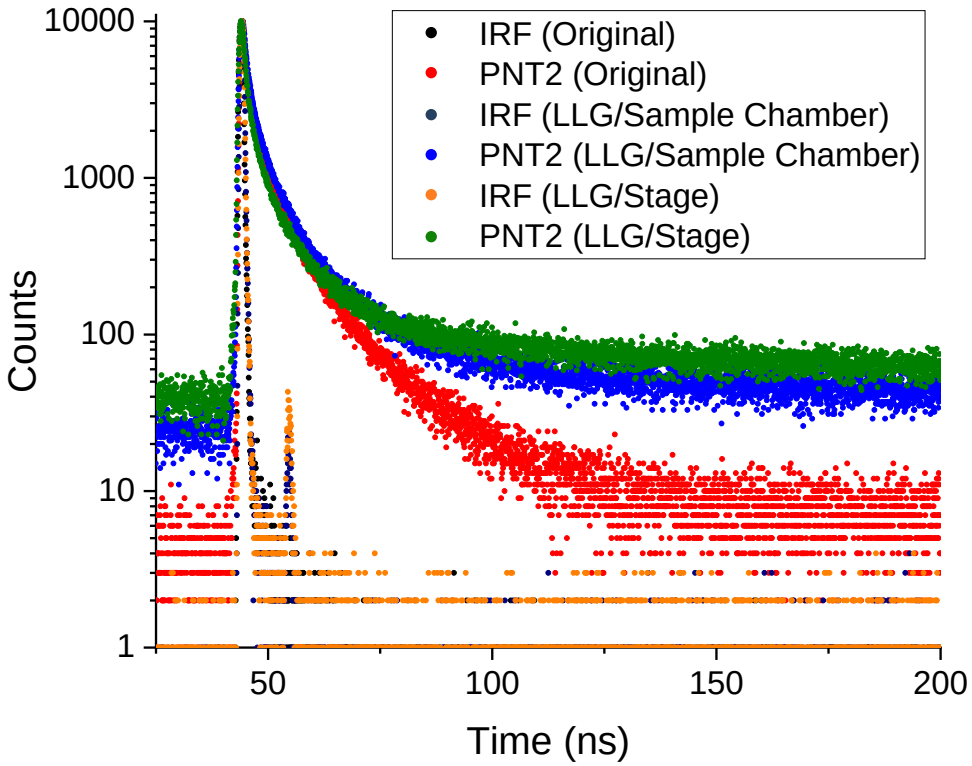

Figure 6.4: Comparison of the fluorescence decays of PNT2 cells obtained on the conventional TemPro setup (Original), and the setups where the light guides are used with the sample chamber (LLG/Sample Chamber) and the translational stage (LLG/Stage) described in Chapter 3. Comparison measurements of PC3 cells on each system are shown in Appendix C.

The IRF measurements on both liquid light guide setups shown in Figure 6.4 show the secondary reflection peak previously discussed in Chapter 3, however as predicted this peak does not influence the fluorescence decays obtained as these decays are much longer than that of NADH free in solution. Figure 6.4 also highlights the high level of background noise in the measurements using the liquid light guides. The photon detection rate was lower in both light guide system setups, leading to a significantly longer acquisition time in each case (1316 s and 401 s in the sample chamber and translational stage light guide setups respectively compared to 52 s in the conventional setup). The lower detection rate is most likely due to the smaller acceptance cone of the liquid light guide windows for delivering and collecting light compared to the optics in the conventional setup. The liquid light guide system setups are also not entirely light tight – replicating the surgical environment – and so the combination of this with the long acquisition time allows for a larger background noise in the measurements. A comparison of the fluorescence lifetime parameters obtained for these measurements are shown in Table 6.3.

System	τ_1 (ns)	B_1 (%)	α_1	τ_2 (ns)	B_2 (%)	α_2	τ_3 (ns)	B_3 (%)	α_3	τ_{avg} (ns)	χ^2
Original	3.68 ± 0.22	41.43	0.19	13.4 ± 0.3	26.42	0.03	0.71 ± 0.03	32.15	0.78	1.70	1.21
LLG/ Sample Chamber	3.67 ± 0.25	42.09	0.22	13.8 ± 0.5	29.45	0.03	0.72 ± 0.03	28.46	0.75	1.87	1.10
LLG/ Stage	3.36 ± 0.29	34.44	0.26	14.1 ± 0.8	25.14	0.02	0.67 ± 0.03	40.42	0.72	1.39	1.07

Table 6.3: Fluorescence lifetime components and corresponding parameters from the PNT2 fluorescence decays shown in Figure 6.4, showing good agreement across all three lifetime components on each system. The corresponding PC3 data is provided in Appendix C.

The results in Table 6.3 indicate that while there is some variation in the percentage contributions of each component to the decay leading to a difference in average lifetimes, the individual lifetime components obtained in the liquid light guide

measurements are in good agreement with those obtained from the measurement on the original setup despite the high background noise. These measurements are a good indicator that the liquid light guide-based setups of the fluorescence lifetime system can produce results similar to those obtained on conventional systems of the complex cell environment.

6.6 Incubation with High Glucose Media

Following confirmation of the monitoring of the NAD(P)H fluorescence decay using rotenone incubation, another factor that was considered was how incubation in cell media with a higher glucose concentration might affect the fluorescence decay of NAD(P)H in both the PNT2 and PC3 cell samples, as cancer cells are known to have a higher rate of glucose consumption compared to healthy cells[49].

6.6.1 Sample Preparation

Two flasks of PNT2 cells were cultured as described in Section 6.3.1, where one flask was cultured using DMEM media with a low glucose concentration of 1 g/L, and the other using DMEM media with a high glucose concentration of 4.5 g/L. While PNT2 cells are most commonly cultured in RPMI media, the cells still appeared to grow well in both the low and high glucose DMEM. DMEM was therefore used here instead for both the low and high glucose PNT2 samples for a more accurate comparison, as this was readily accessible whereas ‘low’ and ‘high’ glucose RPMI cell media was not available. In addition to this, two flasks of PC3 cells were also cultured as described in Section 6.3.1, where one was grown in the low glucose DMEM and the other using the high glucose DMEM. Each of these cell samples were prepared for fluorescence lifetime measurements in the same way as previously described, where they were prepared at a concentration of 1 x 10^6 cells/mL and suspended in PBS.

6.6.2 Results & Discussion

The fluorescence decays of both PNT2 and PC3 cell samples with both low and high glucose concentrations are shown in Figure 6.5 and Figure 6.6.

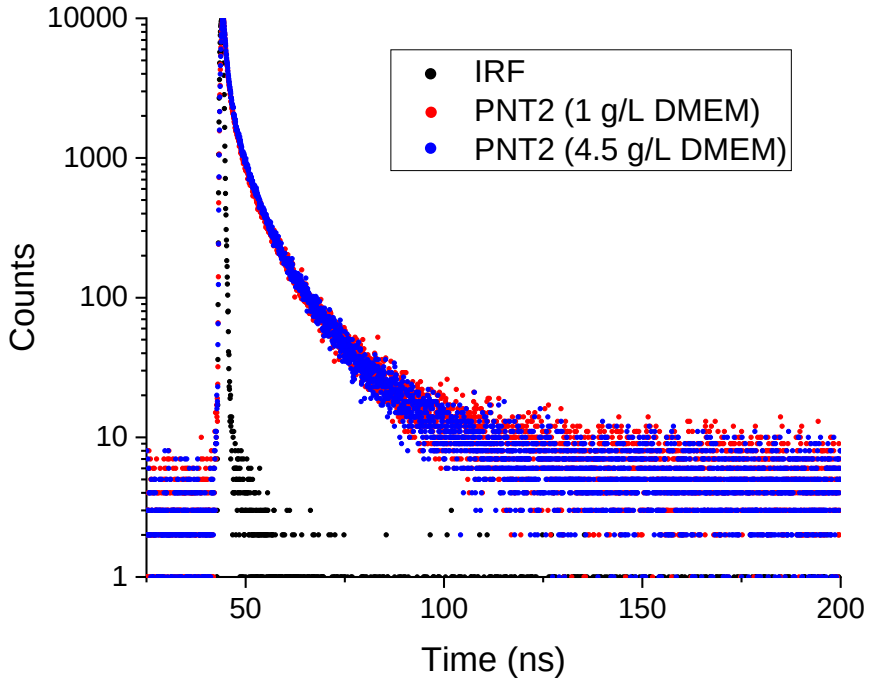

Figure 6.5: Fluorescence decays of PNT2 cells suspended in PBS after incubation in both low (•) and high (•) glucose media where no change in the decay was observed.

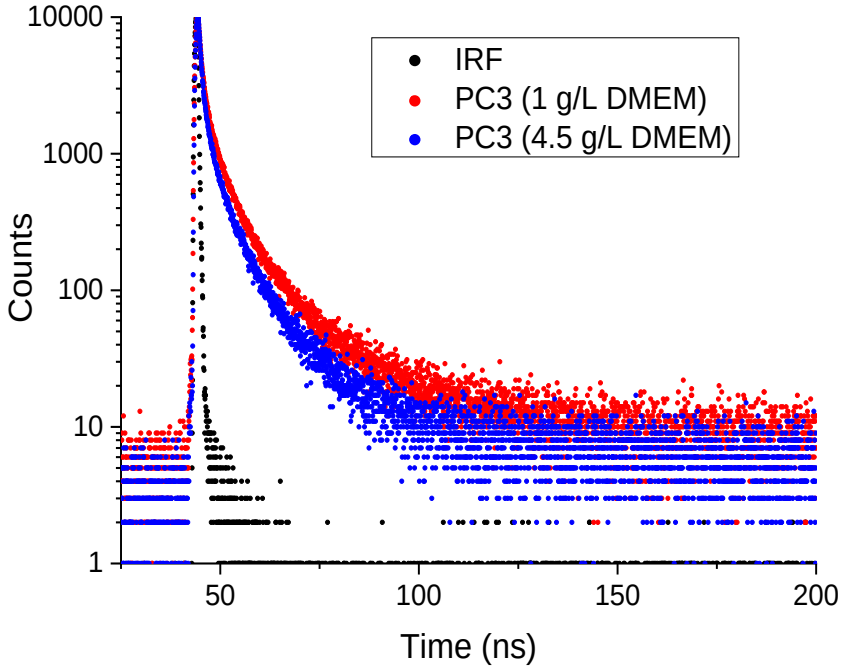

Figure 6.6: Fluorescence decays of PC3 cells suspended in PBS after incubation in both low (•) and high (•) glucose media, where a visible shortening of the decay occurs following incubation in high glucose media.

A visual comparison of the fluorescence decays of the PNT2 cells grown in the 1 g/L and 4.5 g/L cell media in Figure 6.5 shows very little difference between the two decays, indicating that the higher concentration of glucose has not affected NAD(P)H production within these cells. In comparison, a clear difference is seen in the fluorescence decays of the PC3 cells in each media in Figure 6.6, where a shortening of the decay is observed for the PC3 cells grown in the high glucose DMEM. This is also reflected in the individual components for each fluorescence decay shown in Table 6.4.

Cell (glucose conc.)	τ_1 **(ns)**	α_1	τ_2 **(ns)**	α_2	τ_3 **(ns)**	α_3	τ_{avg} **(ns)**	χ^2
PNT2 (low)	3.36 ± 0.23	0.16	12.0 ± 0.3	0.03	0.64 ± 0.02	0.81	1.41	1.24
PNT2 (high)	3.40 ± 0.22	0.15	12.1 ± 0.4	0.02	0.62 ± 0.02	0.83	1.29	1.18
PC3 (low)	3.54 ± 0.22	0.15	13.2 ± 0.4	0.02	0.67 ± 0.02	0.83	1.35	1.22
PC3 (high)	3.02 ± 0.21	0.14	11.1 ± 0.4	0.02	0.57 ± 0.02	0.84	1.08	1.21

Table 6.4: Corresponding fluorescence lifetime components and normalised pre-exponentials obtained from the measurements shown in Figures 6.5 and 6.6, indicating the high glucose media did not have a significant effect on the individual lifetime components obtained from PNT2 measurements compared to those obtained for PC3 measurements following high glucose incubation, where a decrease in all values is observed.

Table 6.Table 6.4 shows that there are no significant changes seen in the individual lifetime components determined for the PNT2 measurements in both low and high glucose media, whereas a decrease in each lifetime component is observed in the PC3 samples. Glucose has been previously reported to shorten the fluorescence decay of NAD(P)H in adipocyte cells[186], where suggested reasons for this have included the distribution and nature of the microenvironment changing with glucose metabolism, as well as an increase in free NAD(P)H also decreasing the average lifetime. It is interesting however to observe here that the glucose concentration has only had a significant effect on the fluorescence decay of NAD(P)H in the cancerous cells and not the healthy cells. As glycolysis is the predominant pathway used by

cancer cells for energy production, a larger amount of glucose available to these cells for consumption could therefore lead to an even higher rate of glycolysis. A preferential use of glycolysis has been previously linked to a decrease in fluorescence lifetime of certain cancerous and pre-cancerous cell lines[55,56], and so this may explain what is happening here. Since the healthy PNT2 cells will not rely on glycolysis as heavily as the cancerous cells, this pathway may not be as influenced by the higher glucose concentration. In addition to this, looking at the ratios of unbound/bound NAD(P)H as explored previously, it is found that this ratio increases from 4.88 to 5.25 in the PC3 cells which is higher than that observed in the PNT2 cells, indicating more of a shift to glycolysis. These results further support a decrease in the fluorescence lifetime being due to the preferential use of glycolysis in certain cancer cell lines.

6.7 Conclusions

In Section 6.3, measuring the fluorescence decay of NAD(P)H at various emission wavelengths determined that an emission wavelength of 450 nm provided a good balance of monitoring the samples close to the emission wavelength maximum of NAD(P)H, a high enough α value to provide an acquisition time of less than 3 minutes, as well as a bigger difference in the lifetime being observed for τ_3 between the healthy and cancerous cells. In addition to this a comparison of the ratios of the unbound/bound NAD(P)H from these measurements indicated a shift towards glycolysis in the cancerous cells as would be expected, demonstrating how these ratios determined from the fluorescence lifetime measurements could be used to distinguish between healthy and cancerous cells. This work also provided initial evidence that the experimental protocol was correct for monitoring NAD(P)H fluorescence lifetimes in the cell environment, as the lifetime values found were in good agreement with values quoted in literature. Incubation with rotenone further established that it was the fluorescence lifetime of NAD(P)H was being observed in the cells. The decrease in the fluorescence lifetime components in combination with an increase in free NAD(P)H after incubation with rotenone confirmed that exciting the cell samples at 339 nm in combination with fluorescence emission being

collected at 450 nm is sufficient for measuring the fluorescence lifetime of NAD(P)H in the complex cell environment.

The effect of glucose concentration in the cell media was also investigated for both cell lines, where a decrease in the fluorescence decay of NAD(P)H was observed in the cancer cells but not the healthy cells. If this decrease in the fluorescence decay in the cancer cells is indeed due to a higher consumption of glucose, this could indicate another potential way in discriminating between the two types of cells in a surgical environment along with the unbound/bound NAD(P)H ratio. Measuring the fluorescence decay of NAD(P)H in other cancer cell lines grown in low/high glucose media may be beneficial to determine if this trend is also observed in other types of cancer cells. In addition to this further confirmation of a change in the relative concentrations of unbound/bound NAD(P)H based on the pre-exponential factors via comparison measurements using a different technique such as mass spectrometry may also be beneficial.

7. Final Conclusions & Future Work

The work carried out in this thesis investigates a number of aspects relevant to tumour margin estimation by utilising fluorescence-based techniques. These aspects have included instrumentation development, intrinsic fluorophore studies, phantom tumour margin design and measurements of the cellular environment – all of which have provided information that could prove useful in future studies involving the application of fluorescence techniques in determining tumour margins.

A liquid light guide-based fluorescence lifetime system was developed, where the light guides were initially incorporated into an existing HORIBA TemPro lifetime system. The liquid light guides offered advantages such as transmitting more light and being more robust in comparison to traditional silica fibre bundles used in the clinical setting, as well as reducing the size and cost and increasing the portability of a fluorescence lifetime system through their incorporation. Initial measurements after the incorporation of the liquid light guides demonstrated that such a setup was capable of producing fluorescence decays and corresponding lifetime components that were in excellent agreement with measurements made on a typical HORIBA DeltaFlex system, as shown in Table 3.1 for the fluorophores CG436, Rhodamine 6G, MeADOTA and JA120. The system was further developed to incorporate a translational sample stage to replace the existing sample chamber, where again this particular setup was shown to provide results as good as those obtained on the original system setup for the fluorophores covering a range of excitation and emission wavelengths as demonstrated in Table 3.2. Measurements of NADH in a simple solvent environment on the liquid light guide-based setup revealed the presence of reflected photons in the obtained decays due to reflections occurring at windows of the light guides. This was found to not be of issue in later measurements of NAD(P)H in the cellular environment on these systems, which holds a stronger resemblance to the environment NAD(P)H would be measured in during surgery. Such a setup is not currently available commercially, but with further improvements may find use in certain applications outside the laboratory. Future improvements could include better coupling between the light guides and the sample/detector to minimise reflections and reduce background photons being collected, however for a

real-life application such as the surgical environment these are challenges that would likely arise in such a setting. These are not of immediate concern when the obtained data is still in excellent agreement with that obtained on a conventional setup.

Further characterisation measurements of NADH in various solvents were conducted to obtain a better understanding of how different environmental factors affected its fluorescence properties, where in-depth characterisation of the fundamental properties of NADH fluorescence is not well documented in current literature. Solvent properties such as polarity and viscosity influenced its properties, where increased polarity caused a redshift in the peak emission wavelength of ~ 10 nm for NADH in the solvents water, PBS and Trizma in comparison to NADH in ethylene glycol, and increased viscosity caused an increase in both the emission intensity and fluorescence lifetime. The increased viscosity of ethylene glycol had the most significant influence, where the obtained lifetime parameters were approximately double those found for NADH in the other solvents. Other factors were also found to influence the fluorescence lifetime of NADH, where oxygen quenched the fluorescence more significantly in certain solvents and measurements at body temperature reduced the fluorescence lifetime in every solvent. Oxygen removal had the most significant effect on the decays obtained for NADH in water and ethylene glycol in particular, where there is a clear increase in the observed decays as shown in Figure 4.8. This is further reflected in Table 4.3, where an increase in both lifetime components as well as the average lifetimes from 0.40 ns to 0.45 ns and 0.76 ns to 0.94 ns observed for NADH in water and ethylene glycol respectively. As argon gas was only bubbled through the samples for ~ 5 minutes to remove the oxygen, it may be useful to increase the time of oxygen removal in future measurements to see the effect on the lifetime after prolonged oxygen deprivation to more accurately resemble the tumour environment. Nevertheless, these measurements indicated how environmental factors that are relevant to cancer studies have an influence on the lifetime properties of NAD(P)H, which need to be considered in more complex environments.

In addition to this, fluorescence anisotropy measurements of NADH in ethylene glycol were also performed and revealed two rotational correlation times of 0.43 ±

0.24 ns and 5.49 ± 0.04 ns. Based on these rotational times and Equation 17, estimates of the particle sizes were calculated and found to be ~ 0.6 nm and 1.4 nm. This is thought to be most likely due to the folded and unfolded conformations of NADH that would be present in the sample rather than the different conformations of amide group in the nicotinamide ring in NADH, as the reasonably large difference in size of ~ 0.8 nm between the two species would be unlikely to have resulted from a rotation of this amide group. These results demonstrate the ability of fluorescence anisotropy to potentially discriminate between the unfolded and folded conformations of NADH free in solution.

Silica sol-gels have also been investigated in this work for their use in mimicking tissue scatter in a phantom tissue environment. Characterisation of silica nanoparticles was initially conducted on stable LUDOX nanoparticles using the long-lived fluorophore MeADOTA and fluorescence anisotropy measurements. Measurements of the LUDOX silica nanoparticles highlighted the capability of MeADOTA for measuring such particles ranging in radii of 3.5 – 11 nm, where the results shown in Table 5.1 demonstrate the accuracy of the measurements in comparison to the quoted manufacturer values. The improved precision of the measurements made with MeADOTA was further demonstrated when compared to measurements in previous work utilising the fluorophore 6-MQ, as ~ 100 x more counts and therefore a longer measurement time were required in these previous measurements to obtain comparable data. In addition to this MeADOTA was used in fluorescence anisotropy measurements to characterise the growth of silica nanoparticles in both silica hydrogel and alcogel environments. Measurements of silica hydrogel samples over ~ 50 hours using MeADOTA revealed the presence of larger particles of radius ~ 6.3 nm compared to the ~ 3.7 nm radius found using Rhodamine 6G due to the ability of MeADOTA in tracking larger changes in depolarisation because of its longer fluorescence lifetime. Silica alcogel measurements also highlighted the resolution of fluorescence anisotropy for measurements small changes in size, where these measurements could be utilised to observe a change of ~ 0.4 nm over a ~ 48-hour period.

Silica alcogels were then utilised for creating phantom tumour margin samples, where various fluorophores were investigated in this environment using the liquid light guide and translational stage-based fluorescence lifetime system described in Chapter 3. Measurements of the phantom margin with Rhodamine 6G and NADH in the doped sol-gel region demonstrated that the sol-gel only region could be clearly identified 1 mm after the margin position based on the fluorescence decays obtained. Measurements of the phantom margin with ICG as the fluorophore in the doped sol-gel region using this setup could not identify the margin position as clearly as only scatter from the sol-gel could be detected from 7 mm before the margin was reached. However FLIM measurements of the same sample provided a much better estimation where images representing purely the sol-gel region were obtained 1 mm after the margin position, demonstrating the improved spatial resolution of the HORIBA Lifetime Imaging system for measuring short-lived samples such as ICG. Obtaining images of a margin position in almost real-time could be extremely beneficial for determining surgical margins intraoperatively, where the measurements conducted here demonstrate the potential of this system for such an application. The silica sol-gel phantoms were relatively simple to prepare with good reproducibility to a suitable degree for this work. Further development of sol-gel based phantoms could be considered in the future, where more in-depth studies on the scattering properties produced by sol-gels depending on their precursors may be beneficial in order to determine what will produce the desired scattering properties, which will depend on the tissue type of interest. While silica sol-gels have intrinsic fluorescence in the UV region, it may also be beneficial to add fluorophores to the design to more accurately represent tissue autofluorescence, as well as add an absorber such as ink to also mimic typical tissue absorption.

The fluorescence lifetime of NAD(P)H in the cellular environment has also been studied in this work. The optimal emission wavelength for measuring NAD(P)H in this environment was first determined. Based on the fluorescence lifetime components obtained from measurements over a range of wavelengths as well as the known peak emission of NAD(P)H, an emission wavelength of 450 nm was chosen to be the most suitable emission wavelength to be used in future measurements to ensure data being collected could most likely be attributed to NAD(P)H. Further

confirmation that NAD(P)H was responsible for the fluorescence signal was found through incubation of PNT2 cells with rotenone, where a decrease in all fluorescence lifetime components as well as an increased contribution of unbound NAD(P)H confirmed NAD(P)H was the source of the fluorescence signal.

A comparison of the fluorescence decay in PNT2 and cancerous prostate cells (PC3) found a higher ratio of unbound/bound NAD(P)H in the cancer cells, indicating a shift towards glycolysis and therefore cancerous behaviour. This demonstrated one method for distinguishing between healthy and cancerous cells. To provide further validation of a change in the normalised pre-exponential factors and therefore the relative concentrations of unbound/bound NAD(P)H in the two cell lines, comparison measurements using a different technique such as mass spectrometry may be beneficial to assist in validating these results. In addition to this, each cell type was incubated with cell media of a higher glucose concentration to see how this affected the fluorescence decay. While no change was observed for the fluorescence decay of NAD(P)H in the PNT2 cells, a decrease in the decay and corresponding lifetime components was observed for NAD(P)H in the PC3 cells when incubated in media with higher glucose levels. This decrease is most likely due to the preferential use of glycolysis in the cancerous cells, therefore when more glucose is available the glycolysis pathway is further upregulated. This has also been previously linked to a decrease in fluorescence lifetime in other cancerous cell lines, and therefore indicates a second potential mechanism that can be utilised for distinguishing between healthy and cancerous cells using NAD(P)H fluorescence. Further comparison measurements of other healthy and cancerous cells grown in high and low glucose media could provide more evidence of this trend and whether or not it is consistent across the majority of cell types.

In summary, the aspects explored in this work demonstrate the many advantages of using time-resolved fluorescence techniques for estimating tumour margins from both an instrumentation and probe perspective. The implementation of liquid light guides for fluorescence lifetime measurements proved successful, where further improvements to the measurement of phantom tumour margins were made using a real-time FLIM system, which could be extremely beneficial in the surgical

environment due to the ability to capture detailed FLIM images in real-time. Measurable differences in the fluorescence lifetime of the intrinsic fluorophore NAD(P)H have also been established in the cellular environment, demonstrating how such a probe could be used in combination with the instrumentation studied as part of this thesis. Fluorescence-based surgical applications area already of widespread interest, but the majority are still in pre-clinical stages in terms of their common use for determining tumour margins; however the potential they have so far demonstrated both in this work and out with could have an extremely positive impact on cancer surgery in the years to come.

8. Appendix

8.1 Appendix A

The additional comparison measurements of JA120 and MeADOTA taken on the monochromator- and liquid light guide-based system are shown in Figure 8.1, further demonstrating the ability of the liquid light guide-based system in measuring over a range of excitation wavelengths, emission wavelengths, and fluorescence lifetimes.

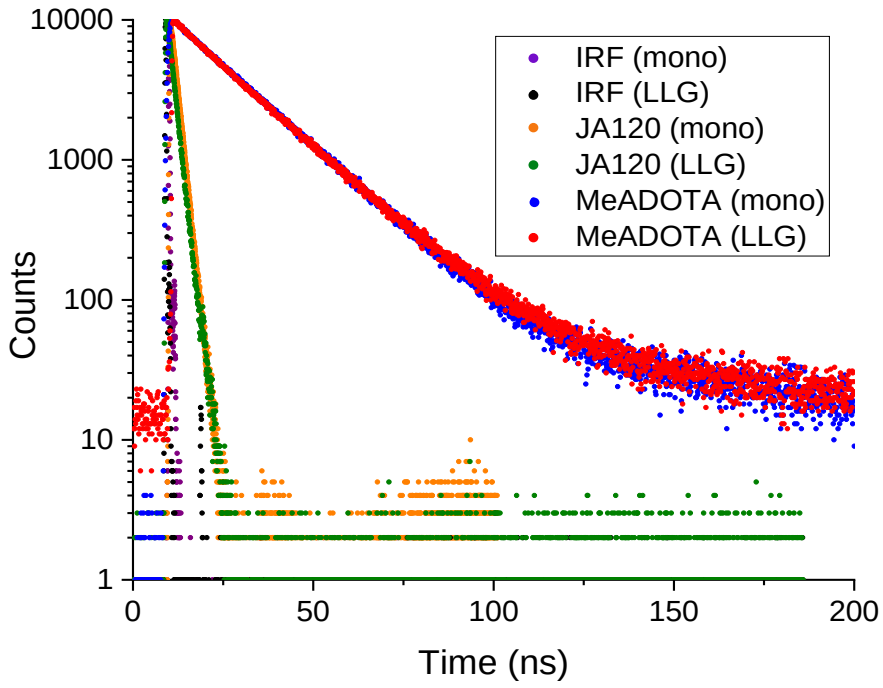

Figure 8.1: Comparison of the fluorescence decays obtained for MeADOTA and JA120 in water on the liquid light guide (LLG) and monochromator (mono.)-based systems. Excitation wavelengths of 494 nm and 638 nm, and emission wavelengths of 570 nm and 685 nm were used for MeADOTA and JA120 respectively. The fluorescence lifetime parameters obtained for these measurements are detailed in Table 3.1.

8.2 Appendix B

The fluorescence decays of NADH in Trizma and PBS after oxygen removal are shown in Figure 8.2. Little difference in the shape of the decays was observed after oxygen removal in these solvents compared to that observed in water and ethylene glycol as shown in Figure 4.8.

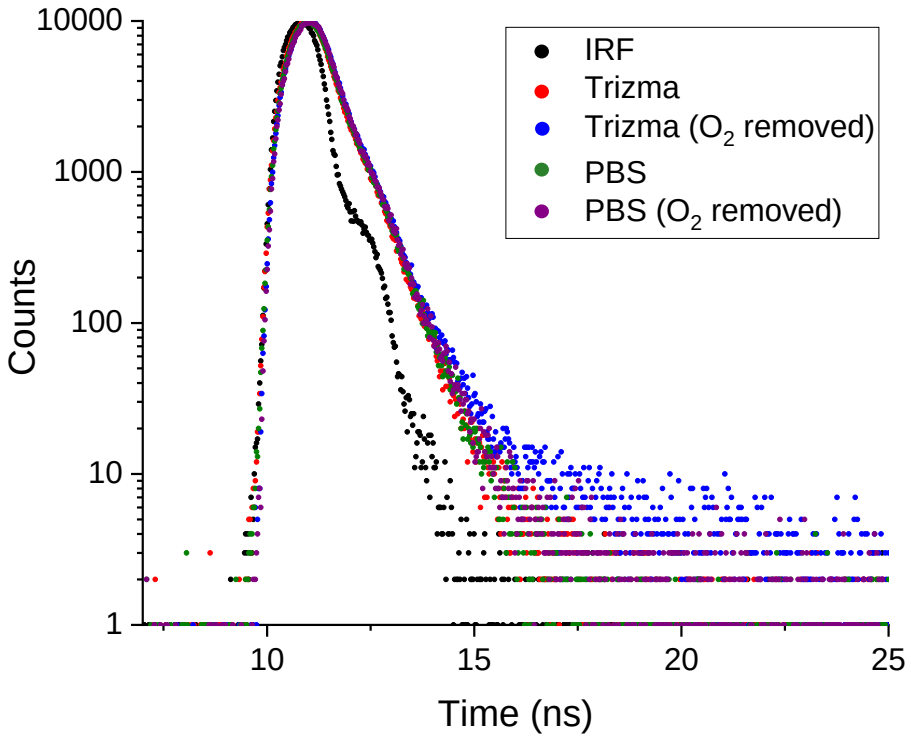

Figure 8.2: Fluorescence decays of NADH in Trizma and PBS at a 40 µM concentration, measured before and after oxygen was removed from the samples. The difference in the shape of the decays shown here was not as significant as that for measurements of NADH in water and ethylene glycol. The fluorescence lifetime parameters obtained for these measurements are detailed in Table 4.3.

8.3 Appendix C

Comparison measurements were also obtained for PC3 cell samples on both the conventional Horiba TemPro setup, the liquid light guide and sample chamber-based system as well as the liquid light guide and translational stage-based system, where the fluorescence decays and corresponding parameters are shown in Figure 8.3 and Table 8.1 respectively.

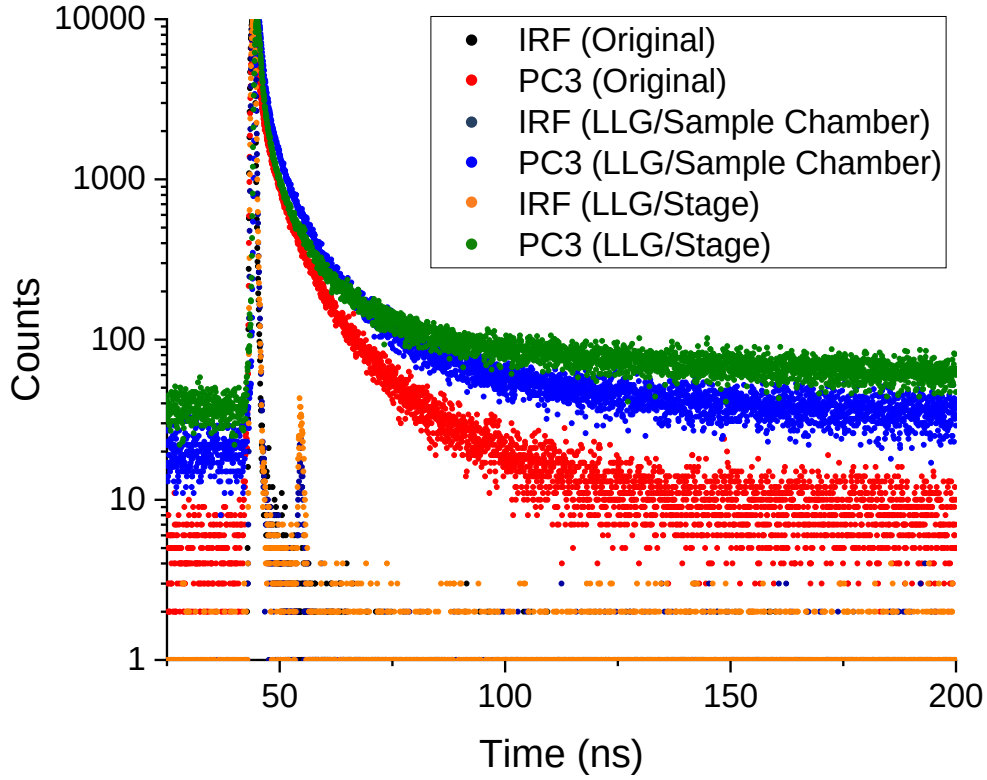

Figure 8.3: Comparison of the fluorescence decays of PC3 cells obtained on the conventional TemPro setup (Original), and the setups where the light guides are used with the sample chamber (LLG/Sample Chamber) and the translational stage (LLG/Stage) described in Chapter 3.

System	τ_1 (ns)	B_1 (%)	α_1	τ_2 (ns)	B_2 (%)	α_2	τ_3 (ns)	B_3 (%)	α_3	τ_{avg} (ns)	χ^2
Original	3.61 ± 0.21	41.39	0.16	13.9 ± 0.4	19.93	0.02	0.63 ± 0.02	38.68	0.82	1.35	1.22
LLG/ Sample Chamber	3.70 ± 0.29	40.82	0.20	13.8 ± 0.6	28.19	0.04	0.75 ± 0.03	30.99	0.76	1.83	1.12
LLG/ Stage	3.45 ± 0.40	32.59	0.13	14.7 ± 0.9	24.12	0.02	0.70 ± 0.03	43.28	0.85	1.39	1.07

Table 8.1: Fluorescence lifetime components and corresponding parameters from the PC3 fluorescence decays shown in Figure 8.3, showing good agreement across all three lifetime components on each system. A bigger difference is seen in the average lifetime of the LLG/sample chamber setup data due to the larger contribution from τ_2 to the decay.

9. References

1 Global Cancer Observatory, Cancer Tomorrow: A tool that predicts the future cancer incidence and mortality burden worldwide from the current estimates in 2018 up until 2040., http://gco.iarc.fr/tomorrow/home, (accessed 23 September 2019).

2 Cancer Research UK, Other treatments, https://www.cancerresearchuk.org/about-cancer/cancer-in-general/treatment/other, (accessed 23 September 2019).

3 M. Abbott and Y. Ustoyev, *Semin. Oncol. Nurs.*, 2019, **In Press**, DOI:10.1016/j.soncn.2019.08.002.

4 M. H. Amer, *Mol. Cell. Ther.*, 2014, **2**, 27.

5 Cancer Research UK, Treat: develop new cancer treatments, https://www.cancerresearchuk.org/funding-for-researchers/our-research-strategy/treat-develop-new-cancer-treatments, (accessed 23 September 2019).

6 M. Andolfi, R. Potenza, R. Capozzi, V. Liparulo, F. Puma and K. Yasufuku, *J. Thorac. Dis.*, 2016, **8**, 3329–3337.

7 P. E. Young and C. M. Womeldorph, *J. Cancer*, 2013, **4**, 217–226.

8 M. A. Simon, V. B. Lokeshwar and M. S. Soloway, *Crit. Rev. Oncol. Hematol.*, 2003, **47**, 91–107.

9 T. G. John, J. D. Greig, J. L. Crosbie, W. F. A. Miles and O. J. Garden, *Ann. Surg.*, 1994, **220**, 711–719.

10 E. Angst, J. R. Hiatt, B. Gloor, H. A. Reber and O. J. Hines, *J. Am. Coll. Surg.*, 2011, **211**, 412–423.

11 E. Schena, P. Saccomandi and Y. Fong, *J. Funct. Biomater.*, 2017, **8**, 1–15.

12 D. Theodorescu, *Rev. Urol.*, 2004, **6**, 9–19.

13 A. B. Blechman, J. W. Patterson and M. A. Russell, *J. Am. Acad. Dermatol.*, 2014, **71**, 29–35.

14 L. van Manen, H. J. M. Handgraaf, M. Diana, J. Dijkstra, T. Ishizawa, A. L. Vahrmeijer and J. S. D. Mieog, *J. Surg. Oncol.*, 2018, **118**, 283–300.

15 J. Eden and J. V Simone, *Assessing the Quality of Cancer Care: An Approach to Measurement in Georgia*, The National Academic Press, Washington DC, 2005.

16 S. Harmsen, N. Teraphongphom, M. F. Tweedle, J. P. Basilion and E. L. Rosenthal, *Mol. Imaging Biol.*, 2017, **19**, 357–362.

17 Y. Chen, W. Xie, A. K. Glaser, N. P. Reder, C. Mao, S. M. Dintzis, J. C. Vaughan and J. T. C. Liu, *Biomed. Opt. Express*, 2019, **10**, 1257.

18 S. B. Mondal, S. Gao, N. Zhu, R. Liang, V. Gruev and S. Achilefu, *Adv. Cancer Res.*, 2014, **124**, 171–211.

19 H. Eggemann, T. Ignatov, A. Beni, S. D. Costa, O. Ortmann and A. Ignatov, *Geburtshilfe Frauenheilkd.*, 2013, **73**, 1028–1034.

20 F. T. Nguyen, A. M. Zysk, E. J. Chaney, J. G. Kotynek, U. J. Oliphant, F. J. Bellafiore, K. M. Rowland, P. A. Johnson and S. A. Boppart, *Cancer Res.*, 2009, **69**, 8790–8796.

21 D. Dumitru, M. Douek and J. R. Benson, *E-cancer Med. Sci.*, 2018, **12**, 1–8.

22 Dune Medical Devices, MarginProbe® Overview, https://www.dunemedical.com/, (accessed 5 October 2019).

23 J. M. Dixon, L. Renshaw, O. Young, D. Kulkarni, T. Saleem, M. Sarfaty, R. Sreenivasan, C. Kusnick, J. Thomas and L. J. Williams, *Eur. J. Surg. Oncol.*,

2016, **42**, 1834–1840.

24 LsBioPath, Solution: ClearEdge, http://lsbiopath.com/solution/, (accessed 5 October 2019).

25 G. E. Moore, W. T. Peyton, L. A. French and W. W. Walker, *J. Neurosurg.*, 1948, **5**, 392–398.

26 T. G. Barnes, R. Hompes, J. Birks, N. J. Mortensen, O. Jones, I. Lindsey, R. Guy, B. George, C. Cunningham and T. M. Yeung, *Surg. Endosc.*, 2018, **32**, 4036–4043.

27 S. L. Hillary, S. Guillermet, N. J. Brown and S. P. Balasubramanian, *Langenbeck's Arch. Surg.*, 2018, **403**, 111–118.

28 J. DeLong, R. M. Hoffman and M. Bouvet, *Expert Rev. Anticancer Ther.*, 2016, **16**, 71–81.

29 B. W. Pogue, E. L. Rosenthal, S. Achilefu and G. M. van Dam, *J. Biomed. Opt.*, 2018, **23**, 100601-1–100601-9.

30 P. S. Low, S. Singhal and M. Srinivasarao, *Curr. Opin. Chem. Biol.*, 2018, **45**, 64–72.

31 Y. Zheng, H. Yang, H. Wang, K. Kang, W. Zhang, G. Ma and S. Du, *Ann. Transl. Med.*, 2019, **7**, 4–7.

32 T. Nagaya, Y. A. Nakamura, P. L. Choyke and H. Kobayashi, *Front. Oncol.*, 2017, **7**, 1–16.

33 A. V Dsouza, H. Lin, E. R. Henderson, K. S. Samkoe and B. W. Pogue, *J. Biomed. Opt.*, 2016, **21**, 080901.

34 R. Ting, T. A. Aguilera, J. L. Crisp, D. J. Hall, W. C. Eckelman, D. R. Vera and R. Y. Tsien, *Bioconjug. Chem.*, 2010, **21**, 1811–1819.

35 M. Wang, F. Tang, X. Pan, L. Yao, X. Wang, Y. Jing, J. Ma, G. Wang and L. Mi, *BBA Clin.*, 2017, **8**, 7–13.

36 H. Wallrabe, Z. Svindrych, S. R. Alam, K. H. Siller, T. Wang, D. Kashatus, S. Hu and A. Periasamy, *Sci. Rep.*, 2018, **8**, 1–11.

37 J. V. Chacko and K. W. Eliceiri, *Methods Appl. Fluoresc.*, 2019, **In Press**, https://doi.org/10.1088/2050-6120/ab47e5Manuscript.

38 R. W. Gao, N. T. Teraphongphom, N. S. van den Ber, B. A. Martin, N. J. Oberhelman, V. Divi, M. J. Kaplan, S. S. Hong, G. Lu, R. Ertsey, W. Tummers, A. J. Gomez, C. Holsinger, C. S. Kong, A. D. Colevas, J. M. Warram and E. L. Rosenthal, *Cancer Res.*, 2018, **78**, 5144–5154.

39 C. Bruschini, H. Homulle, I. M. Antolovic, S. Burri and E. Charbon, *Light Sci. Appl.*, 2019, **8**, 1–28.

40 A. G. T. Van Terwisscha Scheltinga, G. M. Van Dam, W. B. Nagengast, V. Ntziachristos, H. Hollema, J. L. Herek, C. P. Schröder, J. G. W. Kosterink, M. N. Lub-de Hoog and E. G. E. De Vries, *J. Nucl. Med.*, 2011, **52**, 1778–1785.

41 PerkinElmer, IVIS Spectrum In Vivo Imaging System, https://www.perkinelmer.com/uk/product/ivis-instrument-spectrum-120v-andor-c-124262, (accessed 5 October 2019).

42 Quest Medical Imaging, Quest Spectrum, https://www.quest-mi.com/products.html, (accessed 5 October 2019).

43 Fluoptics, Fluobeam, https://fluoptics.com/en/fluobeam/, (accessed 5 October 2019).

44 E. Mery, M. Golzio, S. Guillermet, D. Lanore, A. Le Naour, B. Thibault, A. F. Tilkin-Mariamé, E. Bellard, J. P. Delord, D. Querleu, G. Ferron and B. Couderc, *Oncotarget*, 2017, **8**, 109559–109574.

45 K. Vishwanath and N. Ramanujam, in *Encyclopedia of Analytical Chemistry*, ed. R. A. Meyers, John Wiley & Sons, Chichester, First Edit., 2011, pp. 20–56.

46 M.-A. Mycek and P. Urayama, in *Handbook of Biomedical Fluorescence*, eds. M.-A. Mycek and B. W. Pogue, Marcel Dekker, New York, 2003, pp. 211–237.

47 Khan Academy, Introduction to cellular respiration and redox, https://www.khanacademy.org/science/biology/cellular-respiration-and-fermentation/intro-to-cellular-respiration/a/intro-to-cellular-respiration-and-redox, (accessed 30 September 2019).

48 R. A. Cairns, I. S. Harris and T. W. Mak, *Nat. Rev. Cancer*, 2011, **11**, 85–95.

49 M. G. Vander Heiden, L. C. Cantley and C. B. Thompson, *Science*, 2009, **324**, 1029–1033.

50 O. Warburg, K. Posener and E. Negelein, *Biochem. Z.*, 1924, **152**, 319–344.

51 X. Chen, Y. Qian and S. Wu, *Free Radic. Biol. Med.*, 2015, **79**, 253–263.

52 T. Epstein, R. A. Gatenby and J. S. Brown, *PLoS One*, 2017, **12**, 1–14.

53 M. V. Liberti and J. W. Locasale, *Trends Biochem. Sci.*, 2016, **41**, 211–218.

54 D. Anastasiou, G. Poulogiannis, J. M. Asara, M. B. Boxer, J. Jiang, M. Shen, G. Bellinger, A. T. Sasaki, J. W. Locasale, D. S. Auld, C. J. Thomas, M. G. Vander Heiden and L. C. Cantley, *Science (80-.).*, 2011, **334**, 1278–1283.

55 D. Sud, W. Zhong, D. G. Beer and M. Mycek, *Opt. Express*, 2006, **14**, 4412–4426.

56 M. C. Skala, K. M. Riching, A. Gendron-Fitzpatrick, J. Eickhoff, K. W. Eliceiri, J. G. White and N. Ramanujam, *Proc. Natl. Acad. Sci. U. S. A.*, 2007,

104, 19494–19499.

57 C. P. Toseland, *J. Chem. Biol.*, 2013, **6**, 85–95.

58 I. Bora, S. A. Bogh, M. Santella, M. Rosenberg, T. J. Sørensen and B. W. Laursen, *European J. Org. Chem.*, 2015, **28**, 6351–6358.

59 I. Bora, S. A. Bogh, M. Rosenberg, M. Santella, T. J. Sørensen and B. W. Laursen, *Org. Biomol. Chem.*, 2016, **14**, 1091–1101.

60 T. J. Sørensen, B. W. Laursen, R. Luchowski, T. Shtoyko, I. Akopova, Z. Gryczynski and I. Gryczynski, *Chem. Phys. Lett.*, 2009, **476**, 46–50.

61 H. L. Stewart, P. Yip, M. Rosenberg, T. J. Sørensen, B. W. Laursen, A. E. Knight and D. J. S. Birch, *Meas. Sci. Technol.*, 2016, **27**, 045007.

62 T. J. Sørensen, E. Thyrhaug, M. Szabelski, R. Luchowski, I. Gryczynski, Z. Gryczynski and B. W. Laursen, *Methods Appl. Fluoresc.*, 2013, **1**, 025001.

63 R. M. Rich, M. Mummert, Z. Gryczynski, J. Borejdo, T. J. Sørensen, B. W. Laursen, Z. Foldes-Papp, I. Gryczynski and R. Fudala, *Anal. Bioanal. Chem.*, 2013, **405**, 4887–4894.

64 J. T. Alander, I. Kaartinen, A. Laakso, T. Pätilä, T. Spillmann, V. V. Tuchin, M. Venermo and P. Välisuo, *Int. J. Biomed. Imaging*, 2012, **2012**, 1–26.

65 L. A. Yannuzzi, *Am. J. Ophthalmol.*, 2011, **151**, 745–751.

66 A. De Gasperi, E. Mazza and M. Prosperi, *World J. Hepatol.*, 2016, **8**, 355–367.

67 M. Kaiser, A. Yafi, M. Cinat, B. Choi and A. J. Durkin, *Burns*, 2011, **37**, 377–386.

68 Q. Xiao, T. Chen and S. Chen, *Exp. Ther. Med.*, 2018, **16**, 1577–1585.

69 J. R. Van Der Vorst, B. E. Schaafsma, M. Hutteman, F. P. R. Verbeek, G. J. Liefers, H. H. Hartgrink, V. T. H. B. M. Smit, C. W. G. M. Löwik, C. J. H. Van De Velde, J. V. Frangioni and A. L. Vahrmeijer, *Cancer*, 2013, **119**, 3411–3418.

70 C. Shirata, J. Kaneko, Y. Inagaki, T. Kokudo, M. Sato, S. Kiritani, N. Akamatsu, J. Arita, Y. Sakamoto, K. Hasegawa and N. Kokudo, *Sci. Rep.*, 2017, **7**, 1–8.

71 I. Veys, C. F. Pop, R. Barbieux, M. Moreau, D. Noterman, F. De Neubourg, J. M. Nogaret, G. Liberale, D. Larsimont and P. Bourgeois, *PLoS One*, 2018, **13**, 1–13.

72 L. Boni, G. David, A. Mangano, G. Dionigi, S. Rausei, S. Spampatti, E. Cassinotti and A. Fingerhut, *Surg. Endosc.*, 2015, **29**, 2046–2055.

73 T. Desmettre, J. M. Devoisselle and S. Mordon, *Surv. Ophthalmol.*, 2000, **45**, 15–27.

74 S. Mindt, I. Karampinis, M. John, M. Neumaier and K. Nowak, *Photochem. Photobiol. Sci.*, 2018, **17**, 1189–1196.

75 J. R. Lakowicz, *Principles of Fluorescence Spectroscopy*, Springer, New York, Third Edit., 2010.

76 G. G. Stokes, *Philos. Trans. R. Soc. London*, 1852, **142**, 463–562.

77 B. Valeur and M. N. Berberan-Santos, *J. Chem. Educ.*, 2011, **88**, 731–738.

78 B. Wardle, *Principles and Applications of Photochemistry*, John Wiley & Sons, Chichester, First Edit., 2009.

79 C. Usai and A. Diaspro, in *Encyclopedia of Biophysics*, ed. G. C. K. Roberts, Berlin, Springer., 2013, pp. 826–831.

80 H. Szmacinski and J. R. Lakowicz, in *Topics in Fluorescence Spectroscopy Volume 4: Probe Design and Chemical Sensing*, ed. J. R. Lakowicz, Kluwer Academic, New York, 2006, pp. 1–520.

81 E. Sobakinskaya, M. Schmidt am Busch and T. Renger, *J. Phys. Chem. B*, 2018, **122**, 54–67.

82 P. V Butte, A. N. Mamelak, M. Nuno, S. I. Bannykh, K. L. Black and L. Marcu, *Neuro Image*, 2011, **54**, 1–24.

83 B. Valeur, *Molecular Fluorescence - Principles and Applications*, Wiley-VCH, Weinheim, 2001.

84 L. Bene and L. Damjanovich, *Cytom. Part A*, 2015, **87**, 101–103.

85 HORIBA, *Time-resolved fluorescence lifetime measurements*, Tech. Note TRFT-1.

86 HORIBA, *DataStation v2.4: Software for single photon counting data acquisition*, Operating Guide.

87 HORIBA, *Time-resolved fluorescence anisotropy*, Tech. Note TRFT-2.

88 P. Yip, *Nanometrology using Time-Resolved Fluorescence Techniques*, University of Strathclyde, 2016.

89 D. J. S. Birch, Y. Chen and O. J. Rolinski, in *Photonics: Scientific Foundations, Technology and Applications*, ed. D. L. Andrews, John Wiley & Sons, Hoboken, 2015, pp. 1–49.

90 HORIBA, *DAS6: Fluorescence decay analysis software*, User Guide.

91 HORIBA, *Time-resolved emission spectra/decay associated spectra*, Tech. Note TRFT-3.

92 N. Jain and S. Mukhopadhyay in *Applied Spectroscopy and the Science of Nanomaterials Vol. 2*, ed. P. Misra, Springer, Singapore, 2015, pp. 41–58.

93 G. Weber, *Biochem. J.*, 1952, **51**, 145–155.

94 A. P. Demchenko, *Introduction to Fluorescence Sensing Introduction to Fluorescence Sensing*, Springer, Heidelberg, Second Edit., 2015.

95 K. König, in *Multiphoton Microscopy and Fluorescence Lifetime Imaging: Applications in Biology and Medicine*, ed. K. König, DeGruyter, Berlin, 2018.

96 L. C. Chen, W. R. Lloyd, C. W. Chang, D. Sud and M. A. Mycek, in *Methods in Cell Biology*, 2013.

97 J. R. Lakowicz and K. W. Berndt, *Rev. Sci. Instrum.*, 1991, **62**, 1727–1734.

98 W. Becker, *J. Microsc.*, 2012, **247**, 119–136.

99 I. Bugiel, K. Konig and H. Wabnitz, *Lasers Life Sci.*, 1989, **3**, 47–53.

100 S. F. Silva, J. P. Domingues and A. M. Morgado, *J. Healthc. Eng.*, 2018, **2018**, 1371386.

101 M. O. Lenz, A. C. N. Brown, E. Auksorius, D. M. Davis, C. Dunsby, M. A. A. Neil and P. M. W. French, *Multiphot. Microsc. Biomed. Sci. XI*, 2011, **7903**, 79032D.

102 F. Zappa, S. Tisa, A. Tosi and S. Cova, *Sensors Actuators, A Phys.*, 2007, **140**, 103–112.

103 HORIBA, *EzTime Image: For the QuantiCam Lifetime Imaging Camera* Operating Guide.

104 R. K. Henderson, N. Johnston, F. Mattioli Della Rocca, H. Chen, D. Day-Uei Li, G. Hungerford, R. Hirsch, D. McLoskey, P. Yip and D. J. S. Birch, *IEEE*

J. Solid-State Circuits, 2019, **54**, 1907–1916.

105 QuantIC, *Making the 'invisible' visible.*, June 2019.

106 A. Méndez, in *Optics in Our Time*, eds. M. D. Al-Amri, M. El-Gomati and M. S. Zubairy, Springer, Cham, 2016, pp. 300–333.

107 A. Al-Azzawi, *Fibre Optics: Principles and Practices*, CPC Press, Boca Raton, 2007.

108 K. Amano, Y. Aihara, S. Tsuzuki, Y. Okada and T. Kawamata, *Acta Neurochir.*, 2019, **161**, 695–706.

109 S. Sensarn, C. L. Zavaleta, E. Segal, S. Rogalla, W. Lee, S. S. Gambhir, M. Bogyo and C. H. Contag, *Mol. Imaging Biol.*, 2016, **18**, 820–829.

110 J. Crisp and B. Elliot, *Introduction to Fiber Optics*, Elsevier, Oxford, Third Edit., 2005.

111 Lumatec, *Liquid Light Guides*, 2019.

112 D. Volpi, I. D. C. Tullis, A. Laios, P. N. J. Pathiraja, K. Haldar, A. A. Ahmed and B. Vojnovic, *Proc. SPIE.*, 2014, **8935**, 89350.

113 M. D. Keller, S. K. Majumder, M. C. Kelley, I. M. Meszoely, F. I. Boulos, G. M. Olivares and A. Mahadevan-jansen, *Lasers Surg. Med.*, 2010, **42**, 15–23.

114 D. J. S. Birch, A. Sanderson, A. S. Holmes, D. McLoskey and R. E. Imhof, *Meas. Sci. Technol.*, 1993, **4**, 797–799.

115 A. Sanderson, S. Smith, D. McLoskey, D. J. S. Birch and R. E. Imhof, *Proc. SPIE*, 1993, **1885**, 466–477.

116 A. L. Vahrmeijer, M. Hutteman, J. R. van der Vorst, C. J. H. van de Velde and J. V Frangioni, *Nat. Rev. Clin. Oncol.*, 2013, **10**, 507–518.

117 Q. T. Nguyen and R. Y. Tsien, *Nat. Rev. Cancer*, 2013, **13**, 653–662.

118 J. McGinty, N. P. Galletly, C. Dunsby, I. Munro, D. S. Elson, J. Requejo-Isidro, P. Cohen, R. Ahmad, A. Forsyth, A. V. Thillainayagam, M. A. A. Neil, P. M. W. French and G. W. Stamp, *Biomed. Opt. Express*, 2010, **1**, 627.

119 J. Keating, J. Tchou, O. Okusanya, C. Fisher, R. Batiste, J. Jiang, G. Kennedy, S. Nie and S. Singhal, *J. Surg. Oncol.*, 2016, **113**, 508–514.

120 K. A. Selanger, J. Falnes and T. Sikkeland, *J. Phys. Chem.*, 1977, **81**, 1960–1963.

121 C. D. Geddes, K. Apperson and D. J. S. Birch, *Dye. Pigment.*, 2000, **44**, 69–74.

122 C. D. Geddes and D. J. S. Birch, *J. Non. Cryst. Solids*, 2000, **270**, 191–204.

123 D. J. S. Birch and P. Yip, in *Fluorescence Spectroscopy and Microscopy: Methods and Protocols*, eds. Y. Engelborghs and A. J. W. G. Visser, Humana Press, 2014, pp. 279–302.

124 Sigma Aldrich, *Tris(hydroxymethyl)aminomethane*, Product Note, 2016.

125 D. J. S. Birch, G. Hungerford, B. Nadolski, R. E. Imhof and A. D. Dutch, *J. Phys. E.*, 1988, **21**, 857–862.

126 D. J. S. Birch, R. E. Imhof and A. Dutch, *Rev. Sci. Instrum.*, 1984, **55**, 1255–1264.

127 T. S. Blacker, Z. F. Mann, J. E. Gale, M. Ziegler, A. J. Bain, G. Szabadkai and M. R. Duchen, *Nat. Commun.*, 2014, **5**, 1–9.

128 J. De Ruyck, M. Famere, J. Wouters, E. A. Perpe, J. Preat and D. Jacquemin, *Chem. Phys. Lett.*, 2007, **450**, 119–122.

129 J. Eng, R. M. Lynch and R. S. Balaban, *Biophys. J.*, 1989, **55**, 621–630.

130 T. G. Scott, R. D. Spencer, N. J. Leonard and G. Weber, *J. Am. Chem. Soc.*, 1970, **92**, 687–695.

131 R. Schuyler, I. Isenberg and R. D. Dyson, *Photochem. Photobiol.*, 1972, **15**, 395–398.

132 A. J. W. G. Visser and A. van Hoek, *Photochem. Photobiol.*, 1981, **33**, 35–40.

133 M. E. Couprie, F. Mérola, P. Tauc, D. Garzella, A. Delboulbé, T. Hara and M. Billardon, *Rev. Sci. Instrum.*, 1994, **65**, 1485–1495.

134 T. S. Blacker, N. Nicolaou, M. R. Duchen and A. J. Bain, *J. Phys. Chem. B*, 2019, **123**, 4705–4717.

135 P. V Butte, Q. Fang, J. A. Jo, W. H. Yong, B. K. Pikul, K. L. Black and L. Marcu, *J. Biomed. Opt.*, 2010, **15**, 027008.

136 T. S. Blacker, T. Berecz, M. R. Duchen and G. Szabadkai, *Bio-protocol*, 2017, **7**, 1–20.

137 M. C. Skala, K. M. Riching, D. K. Bird, A. Gendron-Fitzpatrick, J. Eickhoff, K. W. Eliceiri, P. J. Keely and N. Ramanujam, *J. Biomed. Opt.*, 2007, **12**, 1–19.

138 J. N. Miller, in *UV Spectroscopy: Techniques, instrumentation and data handling*, eds. B. J. Clark, T. Frost and M. A. Russell, Chapman & Hall, London, First Edit., 1993, pp. 17–34.

139 A. Vyšniauskas, M. Qurashi, N. Gallop, M. Balaz, H. L. Anderson and M. K. Kuimova, *Chem. Sci.*, 2015, **6**, 5773–5778.

140 M. V. Shirmanova, I. N. Druzhkova, M. M. Lukina, M. E. Matlashov, V. V. Belousov, L. B. Snopova, N. N. Prodanetz, V. V. Dudenkova, S. A. Lukyanov

and E. V. Zagaynova, *Biochim. Biophys. Acta - Gen. Subj.*, 2015, **1850**, 1905–1911.

141 Sigma Aldrich, *NADH*, Product Information, 2018.

142 B. Muz, P. de la Puente, F. Azab and A. K. Azab, *Hypoxia*, 2015, **3**, 83–92.

143 J. D. Arrigo, in *Stable Nanoemulsions: Self-Assembly in Nature and Nanomedicine*, Amsterdam, 2011, pp. 135.

144 B. W. Pogue and M. S. Patterson, *J. Biomed. Opt.*, 2006, **11**, 041102.

145 S. L. Jacques, *Phys. Med. Biol.*, 2013, **58**, 37–61.

146 A. J. Welch, M. J. C. van Gemert and W. M. Star, in *Optical-Thermal Response of Laser-Irradiated Tissue*, eds. A. J. Welch and M. J. C. van Gemert, Springer, Dordrecht, 2nd edn., 2011, pp. 27–64.

147 J. L. Sandell and T. C. Zhu, *J. Biophotonics*, 2011, **4**, 773–787.

148 J. R. Mourant, M. Canpolat, C. Brocker, O. Esponda-Ramos, T. M. Johnson, A. Matanock, K. Stetter and J. P. Freyer, *J. Biomed. Opt.*, 2000, **5**, 131–137.

149 J. Beuthan, O. Minet, J. Helfmann, M. Herrig and G. Muller, *Phys. Med. Biol.*, 1996, **41**, 369–382.

150 J. T. Walsh, in *Optical-Thermal Response of Laser-Irradiated Tissue*, eds. A. J. Welch and M. J. C. van Gemert, Springer, Dordrecht, Second Edit., 2011, pp. 13–26.

151 A. Kim and B. C. Wilson, in *Optical-Thermal Response of Laser-Irradiated Tissue*, eds. A. J. Welch and M. J. C. van Gemert, Springer, Dordrecht, 2nd edn., 2011, pp. 267–320.

152 A. N. Bashkatov, E. A. Genina and V. V. Tuchin, *J. Innov. Opt. Health Sci.*,

2011, **4**, 9–38.

153 ScienceDirect search of ‘Tissue Phantom’, https://www.sciencedirect.com/search/advanced?qs=tissue phantom&show=25&sortBy=relevance, (accessed 12 September 2019).

154 S. Taghizadeh, C. Labuda and J. Mobley, *Ultrasound Med. Biol.*, 2018, **44**, 2813–2820.

155 K. I. Papadimitriou, L. A. Dempsey, J. C. Hebden, S. R. Arridge and S. Powell, *Biomed. Opt. Express*, 2018, **9**, 2648.

156 L. A. Dempsey, R. J. Cooper, S. Powell, A. Edwards, C. W. Lee, S. Brigadoi, N. Everdell, S. Arridge, A. P. Gibson, T. Austin and J. C. Hebden, *Proc. SPIE*, 2014, **9538**, 953818.

157 G. McIlvain, E. Ganji, C. Cooper, M. L. Killian, B. A. Ogunnaike and C. L. Johnson, *J. Mech. Behav. Biomed. Mater.*, 2019, **97**, 65–73.

158 N. H. M. Jamal, I. S. Sayed and W. S. Syed, *Radiat. Phys. Chem.*, 2019, 108472.

159 J. C. Santos, C. D. Almeida, A. Iwahara and J. E. Peixoto, *Radiat. Phys. Chem.*, 2019, **164**, 108361.

160 M. Navarro-lozoya, M. S. Kennedy, D. Dean and J. I. Rodriguez-devora, *Materialia*, 2019, **8**, 100438.

161 G. J. Owens, R. K. Singh, F. Foroutan, M. Alqaysi, C.-M. Han, C. Mahapatra, H.-W. Kim and J. C. Knowles, *Prog. Mater. Sci.*, 2016, **77**, 1–79.

162 M. C. Gonçalves, *Molecules*, 2018, **23**, 1–26.

163 A. E. Forte, S. Galvan, F. Manieri, F. Rodriguez y Baena and D. Dini, *Mater. Des.*, 2016, **112**, 227–238.

164 E. In and H. Naguib, *AIP Conf. Proc.*, 2015, **1664**, 130002.

165 D. J. S. Birch and C. D. Geddes, *Phys. Rev. E*, 2000, **62**, 2977–2980.

166 P. Yip, J. Karolin and D. J. S. Birch, *Meas. Sci. Technol.*, 2012, **23**, 084003.

167 K. Apperson, J. Karolin, R. W. Martin and D. J. S. Birch, *Meas. Sci. Technol.*, 2009, **20**, 025310.

168 T. Uchino and T. Yamada, *Appl. Phys. Lett.*, 2004, **85**, 1164–1166.

169 P. Yip, J. Karolin and D. J. S. Birch, *Meas. Sci. Technol.*, 2012, **23**, 084003.

170 J. Karolin and C. D. Geddes, *Dye. Pigment.*, 2015, **112**, 50–53.

171 J. Karolin, C. D. Geddes, K. Wynne and D. J. S. Birch, *Meas. Sci. Technol.*, 2002, **13**, 21–27.

172 A. M. Buckley and M. Greenblatt, 1994, **71**, 599–602.

173 Based on preliminary results in: H. L. Stewart, *Masters Thesis: Nanoparticle Metrology*, University of Strathclyde, 2015.

174 G. Hungerford, A. Rei, M. I. C. Ferreira, K. Suhling and C. Tregidgo, *J. Photochem. Photobiol. B Biol.*, 2007, **111**, 3558–3562.

175 M. Endo and P. P. Lin, *Chinese Clin. Oncol.*, 2018, **7**, 1–14.

176 M. Pilewskie and M. Morrow, *Cancer*, 2018, **124**, 1335–1341.

177 M. Y. Berezin, H. Lee, W. Akers and S. Achilefu, *Biophys. J.*, 2007, **93**, 2892–2899.

178 R. C. Benson and H. A. Kues, *Phys. Med. Biol.*, 1978, **23**, 159–163.

179 F. Rotermund, R. Weigand and A. Penzkofer, *Chem. Phys.*, 1997, **220**, 385–

392.

180 J. C. Kraft and R. J. Y. Ho, *Biochemistry*, 2014, **53**, 1275–1283.

181 A. Gerega, N. Zolek, T. Soltysinski and D. Milej, *J. Biomed. Opt.*, 2011, **16**, 067010.

182 W. J. Akers, M. Y. Berezin, H. Lee and S. Achilefu, *J. Biomed. Opt.*, 2008, **13**, 054042.

183 G. A. Wagnieres, W. M. Star and B. C. Wilson, *Photochem. Photobiol.*, 1998, **68**, 603–632.

184 A. Chorvatova and D. Chorvat, in *Fluorescence Lifetime Spectroscopy and Imaging: Principles and Applications in Biomedical Diagnostics*, eds. L. Marcu, P. M. W. French and D. S. Elson, CRC Press, Boca Raton, 2014, pp. 47–76.

185 K. Drozdowicz-Tomsia, M. A. Cahill, K. N. Madlum, M. S. Baker and E. M. Goldys, *J. Biomed. Opt.*, 2014, **19**, 086016.

186 N. D. Evans, L. Gnudi, O. J. Rolinski, D. J. S. Birch and J. C. Pickup, *J. Photochem. Photobiol. B Biol.*, 2005, **80**, 122–129.

187 A. V Meleshina, V. D. Varvara, M. V Shirmanova, V. I. Shcheslavskiy, W. Becker, A. S. Bystrova, E. I. Cherkasova and E. V Zagaynova, *Sci. Rep.*, 2016, **6**, 1–11.

188 M. Wakita, G. Nishimura and M. Tamura, *J. Biochem.*, 1995, **118**, 1151–1160.

189 K. Blinova, S. Carroll, S. Bose, A. V Smirnov, J. J. Harvey, J. R. Knutson and R. S. Balaban, *Biochemistry*, 2005, **44**, 2585–2594.

190 D. M. Jameson, V. Thomas and D. Zhou, *Biochim. Biophys. Acta - Protein*

Struct. Mol. Enzymol., 1989, **994**, 187–190.

191 W. Becker, A. Bergmann, R. Suarez Ibarrola, P.-F. Müller and L. Z. Braun, 2019, 10.

192 H. Schneckenburger, M. Wagner, P. Weber, W. S. L. Strauss and R. Sailer, *J. Fluoresc.*, 2004, **14**, 649–654.